UNIVERSITY OF BLIDA 1

FACULTY OF TECHNOLOGY

Department of Renewable Energy

Doctorate thesis

Specialty: Renewable Energy

TRANSIENT STUDY OF A HEAT PIPE INTEGRATED TO A PARABOLIC TROUGH SOLAR COLLECTOR

By

Mohammed BOUKHALFA

Graduated 26 /01 / 2023 in front of the jury composed of:

Y. Benkhedda	Professor, U. Blida 1	President
B. Rekik	Professor, U. Blida 1	Examiner
M .Abbas	Research Director, UDES	Examiner
M. Roudane	Professor, U. Blida 1	Examiner
M. Merzouk	Professor, U. Blida 1	Supervisor
N. Kasbadji	Research Director, UDES	Co- Supervisor

Blida, January 2023

ملخص

لقد تمحورت دراستنا هذه حول إنجاز نموذج محاكاتي مكثف أسطواني ذي شكل قطع مكافئ، يحتوي على أنبوب حراري مفرغ.

تم تطوير النموذج البصري من خلال تحليل المسار البصري لأشعة الشمس الساقطة. يأخذ النموذج بعين الاعتبار الانعكاسات المتعددة للأشعة الشمسية بين الغطاء الزجاجي والممتص الأسطواني قبل الامتصاص من خلالهما بواسطة الماص، حيث أثبت النموذج قدرته على الدراسة الدقيقة لتأثير عوامل هندسية وبصرية معينة على الأداء البصري للنظام. أما النموذج الحراري النظري، فقد تم تطويره من أجل تحديد المقومات النظرية للأنبوب الحراري في النظامين الدائم والعابر حيث تم إجراء تحليل مفصل لانتقال الحرارة من أنبوب حراري مدمج في هذا المجمع من خلال تطبيق مبدأ انحفاظ الطاقة على كل مكون من مكونات النظام، قمنا بإنشاء نظام المعادلات التفاضلية الجزئية ثم حلها باستخدام طريقة Runge-Kutta من خلال برمجية MATLAB والتي وصفت سلوك النظام في الحالة العابرة.

أخيرًا، تم التحقق من صحة نموذج الحالة المستقرة (الدائمة) من خلال مقارنة النتائج العددية المتحصل عليها مع البيانات التجريبية التي تم الحصول عليها في المراجع المتعلقة بالموضوع، حيث أظهرت النتائج توافقا جيدا مع البيانات التجريبية.

RESUME

Ce travail est consacré à l'étude d'un échangeur caloduc intégré à un concentrateur cylindro-parabolique. Le modèle optique a été développé en analysant le chemin optique des rayons incidents. Le modèle prend en compte les réflexions multiples des rayons solaires entre le couvert en verre et l'absorbeur cylindrique avant leur absorption par le tube collecteur. Le modèle permet d'étudier avec précision l'effet de certains paramètres géométriques et optiques sur le rendement optique du système.

Par ailleurs, un modèle théorique a été développé pour déterminer, en régime permanent puis en régime transitoire, les performances théoriques du système. L'analyse détaillée du transfert de chaleur entre les composants du système et son environnement, en régime permanent et en régime transitoire, a été réalisée, en procédant par la méthode des bilans énergétiques, autour des volumes de contrôle respectifs, des composants. Le système d'équations, aux dérivées partielles, couplées décrivant le comportement du système en régime transitoire a été établi et résolu en utilisant la méthode de Runge-Kutta sur MATLAB.

Enfin, le modèle en régime permanent a été validé en comparant les résultats numériques avec les données expérimentales obtenues dans la littérature. Les résultats ont montré un bon accord avec les données expérimentales.

ABSTRACT

This research focuses on the study of a heat pipe tube integrated into a PTC system. The optical model was developed tracing the path of the solar ray. The model takes into consideration multiple reflections of solar rays between the glass cover and the absorber cylinder before their absorption, the model proved its ability to accurately study the effect of some geometrical and optical parameters on the optical efficiency of the system. A theoretical model was developed to determine in both steady and transient state the theoretical performances of a heat pipe integrated to a parabolic trough solar collector. A detailed numerical heat transfer analysis of a heat pipe absorber integrated into a parabolic trough collector was performed, energy balances were applied in each component of the system. The system of partial differential equations describing the unsteady-state behavior of the system was established and solved using the 2^{nd} order Runge-Kutta method on MATLAB. Finally, the steady state model was validated by comparing the numerical results with experimental data obtained from the literature. The results showed a good agreement correlation with experimental data.

ACKNOWLEDGEMENT

First, I would like to thank Allah for giving me the strength and ability to undertake and complete this research work.

My gratitude goes to my supervisors Pr. Mustapha Merzouk and Dr. Nachida Kasbadji Merzouk for their patience, support, and encouragement, their expertise was invaluable in the formulating of the research topic and methodology in particular.

I would like to express my great appreciation to Pr. Michel Feidt and Dr. Nicolas Blet from « Laboratory of Energetics, Theoretical and Applied Mechanics (LEMTA), ENSEM, University of Lorraine, Nancy, France» for their patient guidance, enthusiastic encouragement and useful critiques of this research work.

My warm thanks are addressed to Pr. BENKHEDA Younes, Professor at the department of mechanics (University of Blida1) for the honor he gave me by accepting to chair my thesis jury. I would like to assure him my deep gratitude for the interest he has shown in this work.

My sincere thanks also Pr. Roudane Mohamed, Professor at the department of mechanics and vice rector of the university of Blida 1, for accepting to evaluate my thesis.

My honest appreciations goes Dr. Abbas Mohammed, Director of Solar Equipment Development Unit for his interest in this work by agreeing to examine and enrich it.

I would like to express my gratitude to Pr. Rekik Brahim from the physics department, University of Blida 1, for his observations and useful criticisms.

I would like to thank Mr. SAID Noureddine, former Researcher at the Renewable Energies Development Center (CDER) for giving me the benefit of his knowledge and experience in the field.

My sincere appreciations go to my parents for their support and encouragement throughout my study.

I am grateful to all my brothers, sisters, family members, and friends for their love and support.

DEDICATION

I dedicate this humbled work to my loving parents

To the soul of my teacher Haddadi Nabila

To my friends and family members

TABLE OF CONTENTS

List of figures

List of tables

NOMENCLATURE

A	: Surface (m^2)
D	: Diameter (m)
E	: End loss ratio (%)
F	: View factor between the glass cover and the reflector
F’	: Collector flow factor
I_0	: Extraterritorial irradiance (W/m^2)
I	: Solar radiation (W/m^2)
K	: Permeability of the porous medium (m^2)
K(θ)	: Incidence angle modifier [-]
L	: Receiver length (m)
L_{st}	: Standard meridian for the local time zone
L_{loc}	: Longitude of the location.
P	: Pressure
Re	: Reynolds number
R	: Thermal resistance (K/W)
R_v	: Gas constant (J/mol. K)
T	: Temperature (°C)
T_g	: Temperature of the upper part of the glass
T_{sv}	: Solar time (Hours).
T_L	: Local time (Hours).
T_{LK}	: Atmospheric total Linke turbidity factor
a	: Aperture width of the parabolic trough collector (m)
e	: Thickness (m)
f	: Focal length (m)
h	: Sun’s elevation angle (Degree)

h_{fg} : Latent heat of vaporization. (J /kg K]

k : Thermal conductivity, (W/m K)

l : Optical distance (m)

m_A : Air Mass [-]

m_v : Mass flow rate of the fluid in heat pipe [$kg \cdot s^{-1}$]

n : The day of the year

$\vec{n}$: Normal vector

n_1, n_2 : Refractive indexes

r : Radius [m]

r : Reflectivity

$\vec{r}$: Vector carrying the direction of the reflected ray

$\vec{s}$: Vector carrying the direction of the solar rays

GREEK SYMBOLS

a : Solar azimuth (°)

α : Thermal diffusivity of the fluid [m^2/s]

α_p : Absorptance of the absorber

β : Receiver tilt angle (°)

β' : Absorber tilt angle (°)

ε : Porosity of the capillary medium

ε_g : Emissivity of the glass cover

ε_p : Emissivity of the heat pipe wall

f : Friction factor

τ : Directional total transmittance

ş : Tracking angle (°)

γ : Intercept factor

ρ_s : Reflectivity of the mirror

γ_s : Azimuth deviation (°)

δ_R : Rayleigh optical thickness.

$\bar{\tau}$: Average transmittance of the upper part of the receiver

ρ_d : Reflectance of the glass cover for diffuse radiation

η_0 : Optical efficiency (%)

ξ : Transversal incidence angle (°)

η : Longitudinal Incidence angle (°)

Φ : Integration angle (°)

φ_m : Rim angle (°)

τ_a : Absorption of radiation in a partially transparent medium

θ : Incidence angle (°)

θ_w : Liquid wetting angle (°)

θ_2, θ_3 and θ_4 : Angles of refraction (°)

ν : Kinematic viscosity of the fluid [m^2/s]

μ : Dynamic Viscosity [Pa/s]

μ_f : Dynamic viscosity at the fluid bulk mean temperature

γ : Intercept factor

τ : Transmittance

$(\tau\alpha_p)_{eff}$: Effective absorptance- transmittance product

σ : Surface tension [N /m]

ρ : Vapor density

u_∞ : Free-stream velocity flows across the cylinder (Condenser)

u_m : Mean velocity

w : Width of a groove (m)

w_f : Metal thickness (m)

δ : Depth of a groove (m)

SUBSCRIPTS

L, U	: Upper and lower
a	: Ambient
air	: Air
b, d and g	: For beam, diffused and global solar radiation,respectively
e, c	: Evaporator, condenser
eff-p	: Effective pore
evc	: Condenser wall
evw	: Evaporator wall
eff	: Effective
ext	: Exterior
conv	: Convection
con	: Conduction
f	: Fluid
f-e	: Working fluid (Th VP-1) – environment
g	: Glass envelope
h_0	: Sun's elevation
Δh_0^{ref}	: Correction of sun's elevation
hp	: Heat pipe
hpw	: Heat pipe wall
$h_{w\text{-}e}$	: Heat pipe wall- environment
i=2	: (For sintered metal powder)
in	: Inlet
int	: Interior
ins	: Thermal insulation
r	: Reflector, receiver
s	: Sky

v	: Vapor
ws	: Wick structure
wm	: Wick materiel
w-f	: Heat pipe wall-working fluid
Z	: Altitude of the location (km
//and ⊥	: For parallel and perpendicular component, respectively

GENERAL INTRODUCTION

Energy consumption worldwide is increasing rapidly due to the increase in the global population and industrialization processes in many countries [1].

The production and use of conventional fossil fuel energy resources account for a high percentage of air pollution, leading to a harmful impact on our environment[2]. Climate change leads to water shortage, damage caused by floods, storms, the spread of disease, and extinction of some species.

Renewable energies represent one of the most promising sources for meeting the world's energy needs. It is also a potential solution to fossil fuel shortage and the high cost of electricity; it also reduces the negative environmental impacts such as CO_2 emissions, global warming and air pollution[3]. Solar energy is a very important renewable energy source that worth great attention since it is abundant, freely available, and technically mature in commercial applications, clean and endless energy sources[4].

At present, solar concentration, technologies have great potential for commercial exploitation of solar energy for electricity production, due to their cost-effectiveness in terms of performance, and high efficiency can be achieved [4].

Parabolic trough technology is the most mature concentrated solar power design[5].

The concentrated solar radiation allows high energy density and consequently higher temperatures can be achieved at the receiver, the heat produced can generate steam for electricity production, or other purposes such as heating homes, water distillation, and refrigeration [6].

The use of heat pipes as solar receivers for parabolic trough collectors can improve the collector's overall efficiency, reduce the circumferential temperature differences around the outer surface of the absorber pipe, and enhance the stability of the receiver and has the ability to operate as a thermal diode [7][8].

This thesis is presented in four chapters, starting with a general introduction and ending with a general conclusion, the contents of this thesis are summarized as follows:

Chapter one presents basic aspects of the sun's position determination, techniques used for the solar radiation measurement focusing mathematical models for the estimation of solar radiation. It also present a literature review on the parabolic trough technologies, different components of the parabolic trough collector and the techniques use to improve the performance of the PTC. It and by presenting a detailed overview of heat pipe including a

brief historical perspective, the principle of operations, types of the heat pipes, and heat pipe's applications for solar energy.

Chapter two will be devoted to the optical modeling of parabolic trough receiver; the optical analysis was carried out by tracing the optical path of the solar ray, the model developed allows study the effects of different parameters on the performance of the parabolic trough collector.

Chapter three will be dedicated to the development of the theoretical model of the heat pipe integrated to a parabolic trough collector, this model allows to determine in steady and transient state the theoretical performance of the system.

Chapter four presents the model validation and the results obtained from the optical and the thermal modeling, taking into consideration the important parameters influencing the performance of the system.

In the end, a general conclusion contains a summary highlighting the main contributions of this study with some perspectives for future research on the topic.

1. CHAPTER 01: BIBLIOGRAPHIC STUDY

1.1 Introduction

This chapter presents basic aspects of the sun's position determination, the measurement of the available solar radiation, and concentrated solar power (CSP) including the Fresnel system, parabolic dish, power tower, and parabolic through system. It also presents a detailed literature review on parabolic trough collectors including the history of the technology, design approach, and performance enhancement techniques. This chapter also presents a literature review on the heat pipe and its applications for solar energy.

1.2 Geometric aspect of solar radiation

The determination of the apparent sun's position depends mainly on the general sun-earth geometry, refraction processes in the atmosphere, and time.

1.2.1 Coordinate systems

They are presented by two systems, the horizontal system and the equatorial system:

1.2.1.1 The horizontal system

a- Elevation Angle (h)

b- Azimuth Angle (α)

1.2.1.2 The equatorial system

a- Declination Angle (δ)

b- Hour angle ($\boldsymbol{\omega_s}$)

As it passes through the atmospheric layer, solar radiation undergoes through:

- An attenuation estimated through the clearness index, Link's turbidity factor.

- A series of absorption and multi-reflection decomposing the solar radiation:

a- Direct radiation

b- Diffuse radiation

1.2.2 Clearness index

The clearness index is a measure of atmosphere clearness. It is calculated as the fraction of the actual total solar radiation on the surface of the earth during a certain period over the theoretical maximum radiation during the same period [9].

The monthly average clearness index K_T is the ratio of the monthly average daily radiation ($\bar{H}$) on a horizontal surface to the monthly average daily extra-terrestrial radiation $\bar{H}_0$. It is presented in the following equation [10]:

$$\overline{K_T} = \frac{\overline{H}}{\overline{H_0}}$$

We can also define a daily clearness index K_T as the ratio of a particular day's radiation (H) to the extra-terrestrial radiation for that day (H_0). It is given by the following equation[10]:

$$K_T = \frac{H}{H_0} \quad (1.1)$$

1.2.3 The Linke turbidity factor

The total Linke turbidity factor is a function of the scattering by aerosols and the absorption by gas, mainly water vapour. When combined with the atmosphere molecules scattering, it summarises the turbidity of the atmosphere, hence the attenuation of the direct beam and the importance of the diffuse fraction [11] [12]. The absorption and scattering caused by atmospheric constituents can be expressed by this factor [11] [12]:

$$T_L^* = T_0 + T_1 + T_2 \quad (1.2)$$

T_0: is the atmospheric turbidity factor caused by gas absorption as by fixed components of the atmosphere to ozone and especially by steam. A model of this factor based on only geo-astronomical parameters allowed us to propose following expressions[11] [12] :

$$T_0 = 2.4 - 0.9 \sin(\varphi) + 0.1 (2 + \sin(\varphi)) A - 0.2z - (1.22 + 0.14A)(1 - \sin(h)) \quad (1.3)$$

Where:

$$A = \sin\left(\left(\frac{360}{365}\right)(j - 121)\right) \quad (1.4)$$

With:

Z: The altitude (km)

J: The day number

A : is a coefficient dependent only on the corrected T_L error factor.

φ: The latitude angle (°)

h: The Sun's elevation angle (°)

T_1: The atmospheric turbidity corresponding to the absorption by atmospheric gases (O_2, CO_2, and O_3) and molecular Rayleigh scattering given by the approach [11] [12]:

$$T_1=0.89^z$$

T_2: The atmospheric turbidity relative to the aerosol scattering coupled with a slight absorption (depend on both the nature and the amount of aerosols), factor which is a function of the Ångström atmospheric turbidity coefficient β [11] [12]:

$$T_2= (0.9+0.4A_{he}) (0.63)^z$$

The Total Linke turbidity factor T_L can be estimated by the monthly average values T_{Lm}. The long-term measurements are used to calculate this mean value with numerous methods [13]. There are two sites in the Sahara Desert of Algeria where T_{Lm} is known, Tamanrasset and Ghardaia. In summer the values of Ghardaia differ from those of Tamanrasset that have higher elevation, this can be explained by hot weather and Sirocco winds that characterize the region of Ghardaia. These kinds of winds transport sand with them [14].

Table 1-1.Monthly mean Linke turbidity factor for Ghardaia an Tamanrasset[15].

Region	Ghardaia	Tamanrasset
Latitude	32.37°	22.78°
Longitude	3.77°	5.52°
Altitude	450 m	1377m
Measurement period	2004-2008	1995-1999
January	2.1	2.7
February	2.7	2.6
March	3.1	3.2
April	3.9	3.3
May	4.2	3.2
June	4.5	3.9
July	4.9	4
August	4.8	4.4
September	4.4	4.5
October	3.7	4.7
November	2.8	3.5
December	2.4	3.7

1.2.4 Solar constant

The solar constant G_{sc} is the energy received from the sun per unit time on a unit area of surface perpendicular to the direction of radiation propagation outside the atmosphere at the mean Earth-Sun distance [16].

The solar constant depends mainly on two factors:

a- The emittance of the sun

b- The view factor

Several experiments were made to measure the solar constant. High altitude aircrafts, balloons, and satellites permitted direct measurements of solar radiation outside most or the earth's entire atmosphere. In 1982, as a result of the different measurements, the World Meteorological (WMO) organization fixed the average value of 1367 $\frac{W}{m^2}$ as the solar constant[17].

1.2.5 History and correction of solar constant

Prior to the invention of rockets and spacecraft, estimations of the solar constant had to be based on ground-based observations of solar radiation after it had passed through the atmosphere and been absorbed and scattered in part by atmospheric components. Estimates of air transmission in various regions of the sun spectrum were used to extrapolate from terrestrial observations taken from high mountains.

Pioneering studies were done by C.G. Abbot and his colleagues at the Smithsonian Institution[18]. These studies and later measurements from rockets were summarized by Johnson (1954) [19]; Abbot's value of the solar constant of 1322 W/m^2 was revised upward by Johnson to 1395 W/m^2.

Direct measurements of solar radiation outside most or the earth's entire atmosphere are now possible thanks to the availability of very high altitude airplanes, balloons, and spacecraft. In nine different experimental programs, these measurements were taken with a variety of devices. They resulted in a value of the solar constant G_{sc} of 1353 W/m^2 with a 1.5 percent estimated error [20]. This standard value was accepted by NASA (1971) and by the American Society of Testing and Materials (2006). Frohlich (1977) [21] reexamined the data that led to the 1353 W/m^2 estimate and lowered it to a new pyrheliometric scale based on instrument comparisons with absolute radiometers. The investigation also incorporated data from the Nimbus and Mariner satellites, and as of 1978, Frohlich suggests a new estimate for the solar constant G_{sc} of 1373 W/m^2, with a probable error of 1 to 2 percent. This was 1.5 percent higher than the previous value and 1.2 percent higher than the highest available spectral measurement-based determination of the solar constant. Hickey et al. (1982) [22] conducted further satellite measurements reporting 1373 W/m^2 and Willson et

al. (1981) [23] reporting 1368 W/m^2. Measurements from three rocket flights reported by Duncan et al. (1982)[24] were 1367, 1372, and 1374 W/m^2. The World Radiation Centre (WRC) has adopted a value of 1367 W/m^2, with an uncertainty of the order of 1%.

1.2.6 Nebulosity

Nebulosity (Ng) expresses the sky area coverage by clouds. The fraction of the sky obscured by clouds, measured in eighths: one Octa equals one eighth of the sky, two Octas equals one quarter, and so on. The goal is to depict the sky using a circle divided into eight equal segments. It is an estimate based on visual judgment. [9]. There are in literature [25] several methods for evaluation of the impact of the nebulosity on beam, diffused and hemi-spherical radiation discussed. However, coefficients used in these calculations depend on local conditions. Influence of nebulosity on the received daily energy sum can be expressed separately for the beam radiation and diffuse.

1.2.7 Measurement of solar radiation

1.2.7.1 Ground measurement

There are different methods to get solar radiation data, in the case of ground measurement, the ground meteorological stations use different instruments to measure solar radiation. There are various instruments for measuring radiation and methods for ground measuring, the use of which depends on the purpose of measurement. There are different devices for measuring global, direct, and diffuse radiation, and there are different devices for measuring radiation in different wavelength ranges.

1.2.7.2 Solar radiation modeling

Various models have been proposed to estimate the solar radiation, these models are in the form of empirical formulas that link the components of solar radiation to key meteorological parameters, such as the clarity index, insolation fraction or duration of insolation, cloudiness, and astronomical parameters such as maximum duration of the day, the declination of the sun, the earth-sun distance variation and solar radiation out of the atmosphere. There are several models in the literature allowing the estimation of solar radiation; we will propose only the models that give results close to the measured solar radiation in Algeria.

a. Perrin Brichambaut's model[26]

Perrin de Brichambaut proposed the formulas of the beam solar radiation, as following:

$$I_b = A \sin(h) e^{[C \sin(h + \frac{4\pi}{180})]^{-1}} \quad (1.5)$$

The diffused solar radiation is estimated by :

$$I_d = \mathrm{B} \sin(h)^{0.4} \quad (1.6)$$

The global solar radiation is estimated by :

$$I_g = \mathrm{D} \sin(h)^{E} \quad (1.7)$$

Table 1-2: The coefficients depend on the quality of the sky

Sky	A W/m^2	B W/m^2	C	D W/m^2	E
Clear sky	1300	87	6	1150	1.15
Average sky	1230	125	4	1080	1.22
Variable sky	1200	187	2.5	990	1.25

b. Simplified Capderou Model

According to Capderou, the relationship giving the best results for Algeria is given by[27]:

$$I_g = 1080 \left[1 + 0.033 \cos\left(\frac{360\,J}{365}\right) \right] \sin(h) \left[\frac{\sin(h)}{0.89^{z}}\right]^{0.22} \quad (1.8)$$

c. R. Sun Model

For the R. Sun model [28], the global radiation incident on a horizontal plane I_{gh} (W/m^2) in the case of a clear sky is into two parts. The beam radiation I_{bh} and the diffuse radiation I_{dh}, are estimated separately.

The beam solar radiation is given by:

$$I_b(h, T_{LK}) = G_0 \sin(h) \exp(-0.866 T_{LK} . m_A \delta_R) \quad (1.9)$$

Where:

T_{LK}: Is the total Linke turbidity factor

Extraterrestrial solar radiation is a function of the solar constant and the distance correction (ε) between the earth and the sun, and it's given by the following equation:

$$I_0 = I_{cs} \times \varepsilon \tag{1.10}$$

Where ε is given by:

$$\varepsilon = 1+0.03344 \cos (J-0.048869) \tag{1.11}$$

Normal direct solar radiation (I_{bn}) is given by:

$$I_{bn} = \frac{I_{bh}(h, T_{LK})}{\sin(h)} \tag{1. 12}$$

The R. Sun model uses this formula for the estimation of optical air mass, with a slight correction of the Sun's elevation

$$m_A = \frac{\frac{p}{p_0}}{\sin h_0^{ref} + 0.50572 * (h_0^{ref} + 6.07995)^{-1.6364}} \tag{1.13}$$

Where $\frac{p}{p_0}$ ration is correction for a given elevation Z, in meter[28]:

$$\frac{p}{p_0} = \exp\left(-\frac{Z}{8434.5}\right) \tag{1.14}$$

Where h^{ref} is the corrected solar altitude angle *h* (in degrees) by the atmospheric refraction component Δh^{ref} [28] given by.

$$\Delta h_0^{ref} = 0.061359(0.1594 + 1.23h0) + 0.065656h_0^2(1 + 28.9344h0 + 277.3971h_0^2) \tag{1.15}$$

$$h^{ref} = h + \Delta h^{ref} \tag{1.16}$$

For: $m_A \leq 20$

$$\delta_R = \frac{1}{(6.6296 + 1.7513m_A - 0.1202m_A^2 + 0.0065m_A^3 - 0.00013m_A^3} \tag{1.17}$$

And for: $m_A \geq 20$

$$\delta_R = \frac{1}{10.4 + 0.718\, m_A} \tag{1.18}$$

Diffuse radiation expression is given by:

$$\mathrm{I_{dh}} = \mathrm{G_0 T_n(T_{LC})\ F_d}\ (h) \tag{1.19}$$

Where:

I_0 is the normal extraterrestrial irradiance [W.m^{-2}]

T_n (T_{LC}) is the diffuse transmittance function, which is rewritten as follows:

$$T_n(T_{LC}) = -1.5843.10^{-2} + (3.0543.10^{-2}.T_{LC}) + (3.797.10 - 4.\mathrm{T}_{LC}^2) \tag{1.20}$$

F_d is the diffuse angular function, it depends on the sun's elevation.

The diffuse angular function (F_d) is given by the following expression.

$$\mathrm{F_d}(h) = \mathrm{A_0} + \mathrm{A_1}\sin(h) + \mathrm{A_2}[\sin(h)]^2 \tag{1.21}$$

Due to the lack of experimental data for Algeria, the Linke turbidity factor (T_{LK}) can be estimated using the formula proposed by Capderou (1987) [27].

$$T_{LK} = 2.4 - 0.9 \sin(\varphi) + 0.1(2 + \sin(\varphi))\,\mathrm{A} - 0.2\,\mathrm{Z} - (1.22 + 0.14\mathrm{A})\,(1 - \sin(h)) + 0.89\mathrm{Z} + (0.9 + 0.4\,\mathrm{A})\,(0.63\mathrm{Z}) \tag{1.22}$$

$$\mathrm{A} = \sin\left[\left(\frac{360}{365}\right)(J - 121)\right] \tag{1.23}$$

1.2.8 **Concentration collectors**

The electromagnetic radiation can be converted into electricity, either:

- Directly through the photovoltaic effect.

- Indirectly through the following steps:

a- Conversion of radiation into heat

b- Conversion of heat into mechanical work

c- Conversion of mechanical work into electricity

The fact that the efficiency of the conversion cycle of heat into work increase with the temperature of the hot source (Carnot efficiency) imposes the use of solar concentration systems. There are four main types of concentrating collectors:

a. Fresnel system

b. Parabolic dish

a. Power tower

b. Parabolic trough system

1.2.8.1 **Fresnel systems**

A linear Fresnel reflectors power plant use series of nearly flat reflecting segments, with each segment matching the curvature of a corresponding focusing mirror in either three or two dimensions, the mirrors focus light onto one or more linear absorbers positioned above the mirrors.

This system aims to offer lower overall costs by sharing a heat-absorbing element between several mirrors (as compared with trough and dish concepts). While still using the line-focus geometry that allows reduced complexity in the tracking mechanism (as compared with central tower).

Figure 1.1 represents the Fresnel reflector installed at the Plataforma Solar de Almería.

Figure 1.1: Fresnel reflector at the Plataforma Solar de Almería[29]

1.2.8.2 **Parabolic dish systems**

A parabolic dish system uses a computer to track the sun and concentrate the sun's rays into a receiver located at the focal point. Parabolic dish systems can reach 1000 °C at the receiver and achieve the highest efficiencies for converting solar heat to electricity.

Figure 1.2 represents two 10-kW SBP Euro dish prototypes installed at Plataforma Solar de Almeria, Spain.

Figure 1.2. Two 10-kW SBP Euro dish prototypes at Plataforma Solar de Almeria, Spain[30].

1.2.8.3 **Power tower system**

In solar power plants, a large number of computer-assisted mirrors called heliostats track the sun individually over two axes and concentrate the solar irradiation onto a single receiver on top of a high tower, where temperatures well above 1000°C can be reached. High-pressure steam is generated to produce electricity.

Figure 1.3. represents PS10 and PS20 installed in Seville, Spain.

Figure 1.3. PS10 and PS20 (Seville, Spain)[31]

1.2.8.4 **Parabolic trough collector**

Parabolic trough collectors concentrate the direct solar radiation onto a tubular receiver situated in the focal line, the absorber is filled with heat transfer fluid such as synthetic oil and then the oil transfers its heat to the storage tank. The collected heat is first converted to mechanical energy, using Rankine cycle, then to electricity [32]. There are other heat applications such as industrial process heat, domestic hot water, space heating, air-conditioning, refrigeration, pumping irrigation water, and water desalination[33].

Figure 1.4. The Euro Trough collector prototype under test at PSA[34].

1.2.9 **Geometry and performance of parabolic trough collector (PTC)**

1.2.9.1 **Parabolic trough Collector geometry**

The equation of the parabola is given as:

$$y = \frac{x^2}{4f} \tag{1.24}$$

Where:

f: is the focal distance (m)

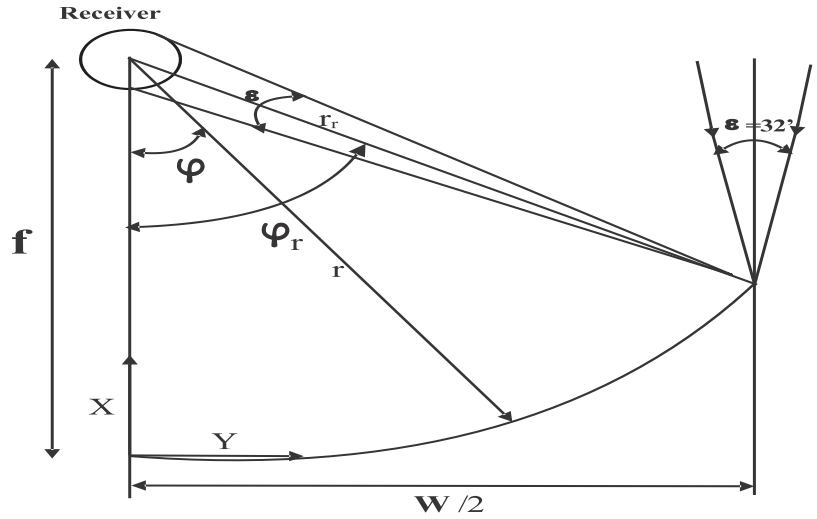

Figure 1.5. Cross-section of the parabolic trough collector

The radius of the parabolic reflector, r is given by:

$$r = \frac{2f}{1 + \cos(\varphi_r)} \tag{1.25}$$

The rim angle (φ_r)is related to the distance between the different parts of the mirrors and the focal line.

$$\tan(\varphi_r) = \frac{\frac{a}{f}}{2 - \frac{1}{8}\left(\frac{a}{f}\right)^2} \tag{1.26}$$

1.2.9.2 **Aperture area of the parabolic trough collector**

The aperture area is calculated as the product of the aperture width a and l the collector length:

$$A_{ap} = a.l \tag{1.27}$$

1.2.9.3 **Concentration ratio**

The concentration ratio is defined as the ratio of the radiant power density at the collector ($I_{b,ap}$) divided by the incident radiant power density of the sun (I_{in}):

$$C = \frac{G_{b,ap}}{G_{in}} \tag{1.28}$$

1.2.9.4 **Geometrical concentration ratio**

The geometrical concentration ratio is defined as the ratio of the effective aperture area (A_a) to the receiver aperture area(A_r).

$$C_G = \frac{A_a}{A_r} \tag{1.29}$$

1.2.10 Performance of parabolic trough collector (PTC)

The overall performance of the parabolic trough collector depends on the optical and thermal efficiencies. The optical efficiency of a PTC depends largely on the material properties of the reflector and glass cover.

1.2.10.1 Optical efficiency

In 1985 Rabl, proposed a simple equation for optical efficiency which is available for all concentration solar powers (CSP) systems [35].

$$\eta_0 = \rho\tau\alpha\gamma \tag{1.30}$$

With:

γ is the intercept factor which is the fraction of the solar radiation incident on the absorber surface, it depends on the construction accuracy and the geometric size, and its value varies between 0.9 and 1[36].

ρ,τ and α are respectively the reflectance of the mirror, the transmittance of the glass cover, and the absorptivity of the receiver.

1.2.11 The absorbed solar radiation

The absorbed solar radiation (I_{ab}) per unit area is given by:

$$I_{ab} = I_b\rho\tau\alpha\gamma \tag{1.31}$$

Incidence angle modifier $K_{\tau\alpha\gamma}$ can be introduced to take account of deviations from the normal angle of incidence of the solar radiation on the aperture area. Biaxial incidence modifiers are needed in the case of cylindrical systems, separate treatment for the longitudinal and transverse planes is required. However, the transverse incidence angle modifier is treated only in case of tracking errors and may not be needed in practice [10].

In this case I_{ab} is given by:

$$I_{ab} = I_b\rho_s(\tau\alpha\gamma)_n K_{\tau\alpha\gamma} \tag{1.32}$$

1.2.12 Glass mirrors

Mirrors have a multilayer structure; the first layer below the glass is the reflective layer, namely the silver layer. A protective layer of copper is applied under the silver layer, on which three epoxy coatings are added: a primer, intermediate and protective topcoat. In most solar mirrors that have been used so far, the first and second layers contain a certain percentage of lead, but protective layers without copper and lead are under development.

Figure 1. 6 show the variation of reflectivity of silver with solar spectrum.

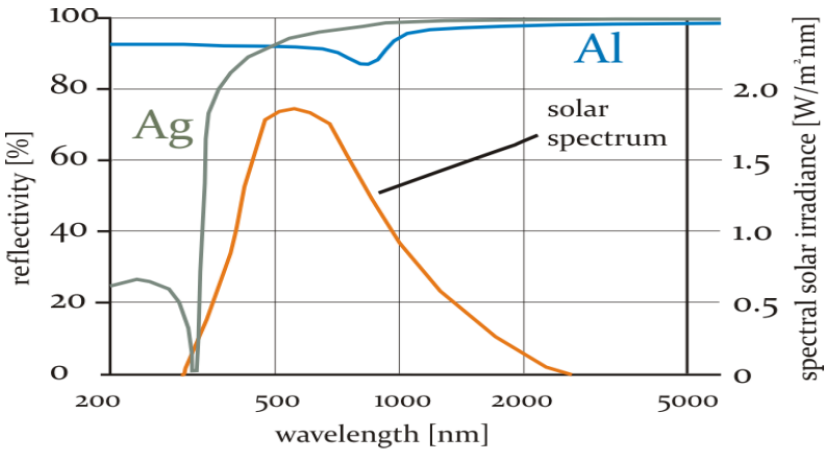

Figure 1.6. Reflectivity of aluminium compared to silver and related to the solar spectrum (source: Schott)[37].

1.2.13 **Heat collection element (HCE)**

The HCE consists of a steel absorber tube coated with a selective coating; the selective surface can either be black chrome or a selective ceramic/metal (cermet). The absorber is placed inside a concentric glass cover, the air vacuum between the absorber and the glass cover reduces convective and conductive heat losses and prevents the degradation of the selective coating at high temperatures [38].

1.2.14 **Glass tube**

The glass tubes used are borosilicate 3mm thick. The borosilicate transmittance which is 92% can be increased to 96% after anti-reflection treatment. The diameter of the tubes varies from 100 to 120 mm.

Figure 1.7 shows the Borosilicate Transmittance and Spectral Emissions of the Sun and a Black Surface at 380 °C.

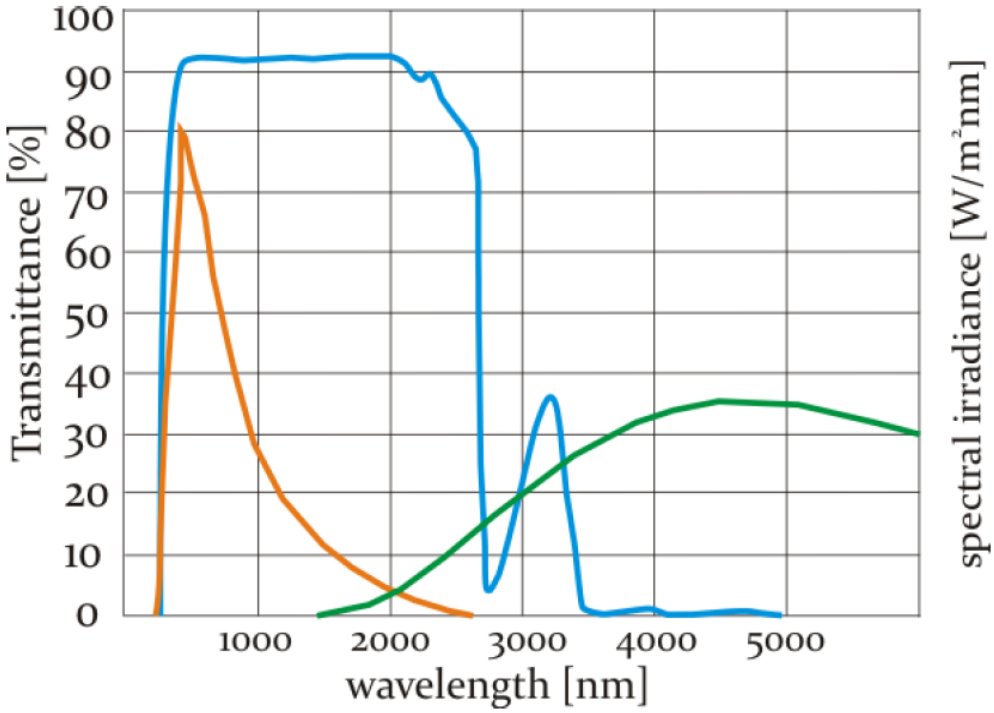

Figure 1.7. Transmittance of borosilicate glass without antireflective coating (blue line), solar spectrum (orange line) and thermal radiation at about 380 °C (green line), spectral irradiance without scale (source for transmittance of borosilicate glass: Schott)

1.2.15 **Heat transfer fluid (HTF)**

The fluids used such as mineral or synthetic oils must meet the following conditions [39].

- Stability at high temperatures (number of cycles)
- Not corrosive
- Not flammable, non-volatile and non-explosive
- Low viscosity
- High mass heat

Figure 1. 8. Shows the classification of transfer fluids HTF for PTC application [39].

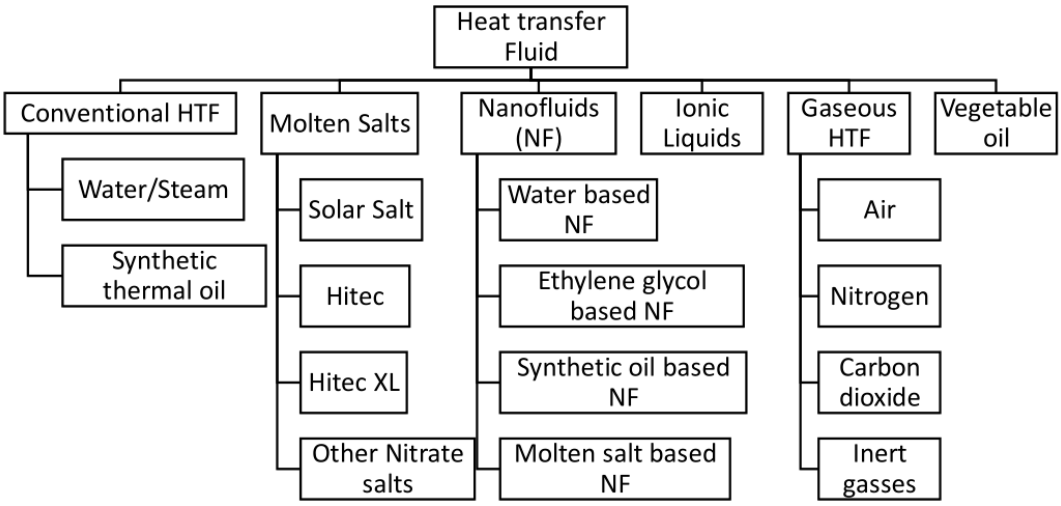

Figure 1.8. Classification of HTF for PTC system[39].

1.2.16 **Parabolic trough orientation**

The collectors can be mounted with the axis of the cylinder oriented in the direction:

- North-South alignment, (N-S)

-East-West alignment, (E-W)

If the PTC is aligned to the N-S direction, the tracking mechanism tracks the daily path of the sun, while in E-W alignment the tracking system follows the displacements in the sun's elevation which depends on the latitude and day of the year [40]. The PTC needs minimal adjusting during the daytime for East-West alignment and the aperture area is always facing the sun at noon but the collector's performance at the beginning and the end of the day is considerably reduced due to the large incident angles (cosine effect). PTC's with North-South orientation have the highest cosine loss at noon and the lowest in the morning and evening.

1.2.17 **Literature review on parabolic technology**

This literature review on PTC technology is divided into three main sections:

1. History of parabolic trough technology.
2. Performance enhancement techniques and applications.
3. Optical study of the PTC.

1.2.17.1 **History of parabolic trough technology**

This section presents a literature review of the development of PTCs throughout the history of technology. The first real practical experience of PTCs was conducted in 1870 by a Swedish engineer immigrant to the USA named John Ericsson, he succeeded to design and build a PTC collector with 3.25m^2 aperture width which was able to drive a small 373 W engine. The system was used to produce steam. The same engineer built seven other hot-air

engines from 1872 to 1875, whereas using air as a working fluid, Ericsson refused to reveal any technical details about his boilers for protective reasons [41]. In 1883, Ericsson [42] built a large ‘‘Sun motor’’ which was exhibited in New York, it consisted of a 3.33 m long, 4.9 m wide PTC. The whole system was moved manually to track the Sun. He claimed that during Summer trials, the engine’s steam pressure was 0.24 Mpa with an average speed of 120 rpm[41][42]. In 1907 German engineers Wilhelm Maier and Adolf Remshardt [43], invented a PTC with what is called today (Direct Steam Generation or DSG). From 1906 to 1911, an American engineer, Frank Shuman, developed and tested several solar engines. In 1907 he used his 3.5 h.p steam engine for pumping irrigation water in Tacony, Pennsylvania (United States), ether was used as the working fluid [41]. In 1913, with the help of Charles Vernon Boys, a British consultant, they succeeded to build and install a parabolic trough power plant in Media, Egypt[41]. The trough collectors were used to produce steam and vapor engines drove the pumps. The produced power was used for irrigation water. Each parabolic concentrator (five in total) was 62.5 m long and 4m aperture width, the total collecting surface was 1280.8m^2. The concentration ratio of 4.6 resulted in an overall peak absorber efficiency of 40.7 %[41]. The system was able to pump 27,000 liters of water per minute[37]. The power plant originally rated at 75 kW mechanical energy, whereas reports on the actual output vary from just over 14 kW to a maximum of 54 kW [41]. Despite all the difficulties, the system was patented in 1917[44].

Figure 1.9. represents the parabolic trough power plant in Egypt built in 1913.

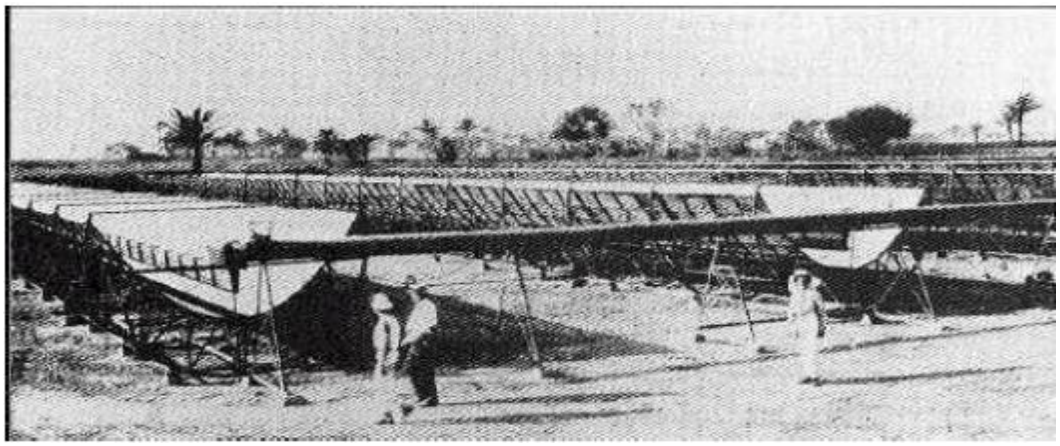

Figure 1.9. Parabolic trough power plant in Egypt built-in 1913 (source: Ragheb 2011)

In 1936, C.G. Abbot used parabolic trough collectors to convert solar energy into mechanical power using a 0.37 kW (0.5 h.p) steam engine. The PTC axis was mounted parallel to the earth's axis of rotation to produce the familiar equatorial mounting used by astronomers. The author claimed an overall system efficiency of 15.5%. A single tube flash-boiler wrapped in a long, double-walled evacuated glass sleeve was placed along the focal axis of the PTC. The vacuum was created to reduce heat losses, and water was fed to the boiler automatically. The system was designed to raise full steam pressure within five minutes of exposure to the Sun's rays, producing saturated steam at 374°C [33][41]. In 1938, he used a similar boiler in Florida to power a 0.15 kW steam engine. As cited by Spencer, Abbot suggested that a system using this boiler to produce steam at 225 °C should obtain a theoretical overall efficiency of 15.5% and a real efficiency of 11.7% [45].

Higher fossil fuel prices encouraged to restore the interest in the parabolic trough technology in 1977. The US Department of Energy as well as the German Federal Ministry of Research and Technology were forced to take new measures. They began to finance the development of several process heat machines and water pump systems with parabolic trough collectors.

In 1981, the parabolic trough technology managed to enter the market. American companies such as Acurex Solar Corp manufactured and marketed several PTCs (models Acurex 3001 and Acurex 3011), Acurex 3001 collector with a rated power of 500 kW was installed at the Platforms Solar de Almeria (PSA) (Spain) [46].

In 1981, the first privately funded process heat machine with 5580 m² parabolic trough collectors was successfully put into operation for thermal heating in Arizona. These trough

systems developed for industrial process heat applications were capable of generating temperatures higher than 260°C [37][46].

The company Luz International Ltd founded in 1979, designed three generations of PTCs, called LS-1, LS-2, and LS-3. After signing an agreement with Southern California Edison (SCE), the first two commercial solar thermal power plants, called Solar Electric Generating System (SEGS) II, and I were constructed in the Mojave Desert in California and started operation in the years 1985 and 1986.

Figure 1.10. Represents LS-3 PTC designed by the company Luz International Ltd.

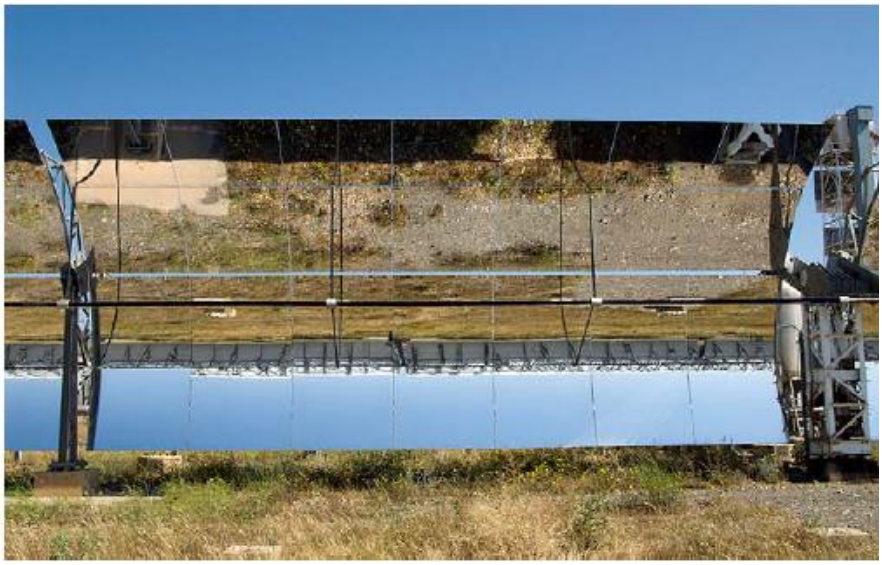

Figure 1.10. LS-3 collector

Many other contracts with SCE were signed and led to the construction of the SEGS III to SEGS IX plants. In total, nine Solar Electric Generating Systems (SEGS), ranging from 13.8 to 80 MW. The nine SEGS plants provide a total capacity of 354 MW and still in operation now. Each plant was developed as an Independent Power Producer facility.

Figure 1.11. SEGS III–SEGS VII solar plants in California[47]

In 2007, the first commercial parabolic trough power plant in Europe called Andasol I was constructed in the Spanish province of Granada, it started generating electricity in December 2008. Another power plant with the same capacity called Andasol II was built in the middle of 2009, the power plants are located near each other and both are connected to the grid. Each of the three plants has a capacity of 50 MWe.

The Andasol power plants were the first CSP power plants with large thermal storage systems. Heat can be stored for 7.5 full load hours. In Summer, the power plants can operate approximately 24 hours a day [47].

Figure 1.12. SEGS III–SEGS VII solar plants in California[47]

Most parabolic power plants are constructed in the USA and Europe; few power plants are constructed in Africa.

Despite the solar potential of Algeria, only one integrated solar combined cycle power plant was constructed. Hassi R'Mel power plant began operation in 2011. The plant combines a 25MW parabolic trough array, covering an area of over 180,000m^2, in conjunction with a 130MW combined cycle gas turbine plant. The gas turbine and steam cycle are fired by natural gas, with the steam turbine receiving additional solar-generated steam during the day.

1.2.17.2 **Performance enhancement techniques**

The improvement of solar energy conversion relies profoundly on the efficiency of the parabolic trough solar collector which can be enhanced by optimizing the reflector geometry, selecting the appropriate materials for the absorber, and choosing the best heat transfer fluid…. Etc.[48].

a- Heat transfer enhancement (HTE)

The major reasons for heat losses in the parabolic trough receiver are due to the improper maintenance of the vacuum between the glass envelope and the receiver tube, end loss in the receiver tube, degradation of coating at high temperature, hydrogen accumulation and permeation in the receiver tube and breakage of seals at the ends of the receiver tube respectively.

The HTF inside the receiver tube has to take up the maximum heat available from the collector. Therefore, there should be a way for the HTF to absorb all the heat provided from the source to the system. All the literature available is categorized under different techniques or ways for heat transfer enhancement onto the receiver tube of the solar PTC namely minimizing heat loss, placing turbulators inside the receiver, use of nanofluids in the heat transfer fluid, and using selective coatings on the receiver tube[49].

b- Heat transfer enhancement by placing turbulators inside the receiver tube

The heat transfer enhancement inside the receiver tube can be made by inducing a higher degree of turbulence through the reduction in the development of the boundary layer, increasing the effective heat transfer area, and the forming of secondary or swirl flow [50]. The heat transfer is augmented by placing various turbulators, namely twisted tapes, coil inserts, dimples, baffles, metal foams, porous discs.. etc. These turbulators cause turbulence in the fluid flow and enhance the rate of heat transfer thereby achieving maximum heat transfer in a system.

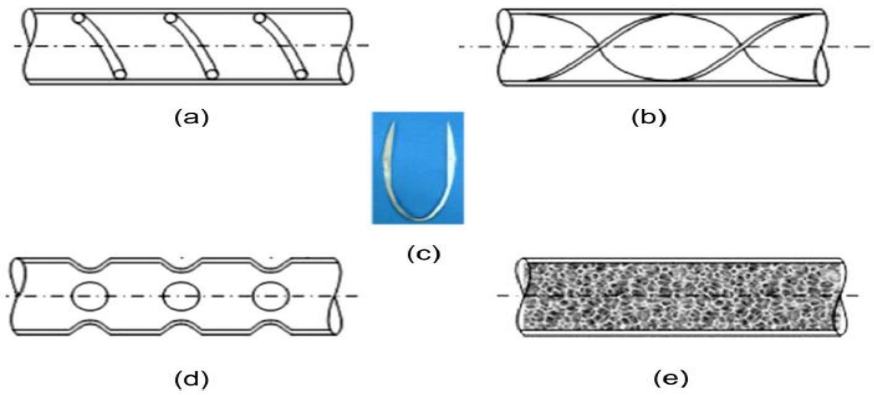

Figure 1.13. Turbulators (a) Twisted tape tube, (b) Coil inserted tube, (c) Baffle, (d) Dimpled tube, (e) Metal foam in tube[50]

Reddy et al. [51] experimentally investigated heat transfer enhancement in the receiver of a solar PTC with porous discs. Six types of receiver configurations were tested in the solar PTC, namely shielded tubular receiver (STR), unshielded tubular receiver (USTR), bottom porous disc receiver (BPDR), U-shaped bottom porous disc receiver (UBPDR), inclined bottom porous disc receiver (IBPDR) and alternate porous disc receiver (APDR) as shown

in Fig. 1.14. The maximum thermal efficiency of the solar PTC with STR, USTR, BPDR, UBPDR, IBPDR and APDR were found out to be 66.96%, 64.78%, 67.59%, 67.78%, 67.43% and 69.03% respectively.

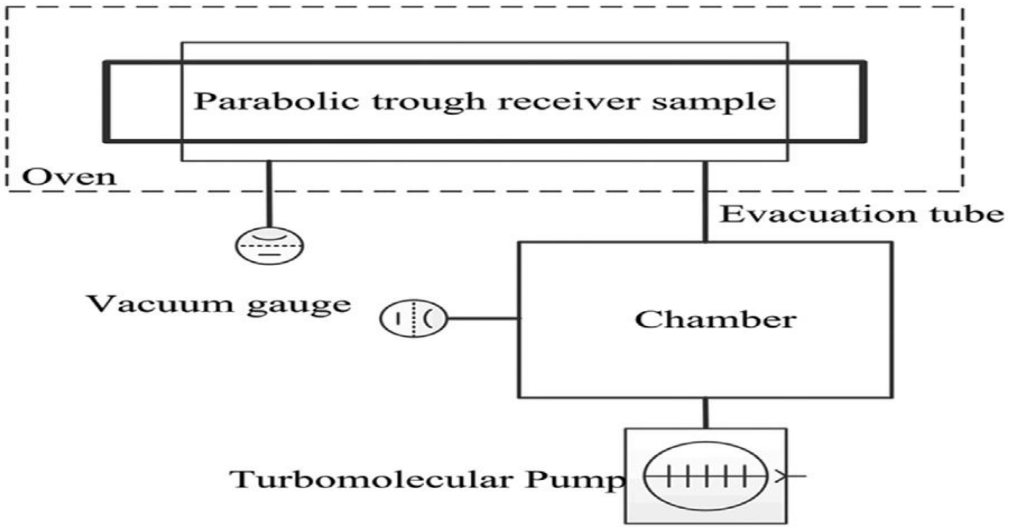

Figure 1.14. Degassing process in a parabolic trough receiver [52].

Song et al.[53] numerically investigated a parabolic trough receiver with helical screw tape inserts. They concluded that the transverse angle (β) greatly affects the incident flux distribution, heat loss, maximum temperature and temperature difference in the receiver. They also found that the increase in Reynolds number gradually reduces the effect of β on the above parameters.

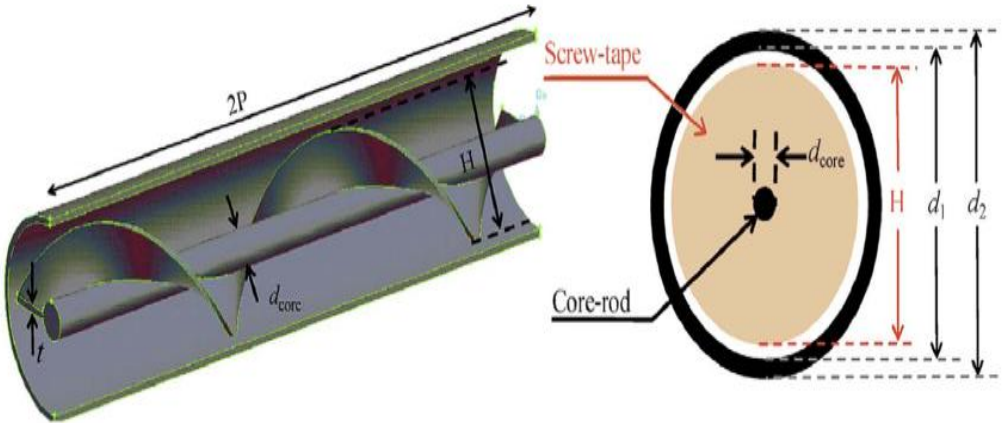

Figure 1.15. Schematics of parabolic trough receiver with helical screw tape inserts [53].

Huang et al. [54] numerically studied the heat transfer enhancement of a parabolic trough receiver with dimples, protrusions and helical fins. They concluded that the dimpled tube with deeper depth and narrow pitch provided better heat transfer enhancement in the receiver

tube than protrusions and helical fins. The performance enhancement factor for dimple tube is in the range of 1.23–1.37.

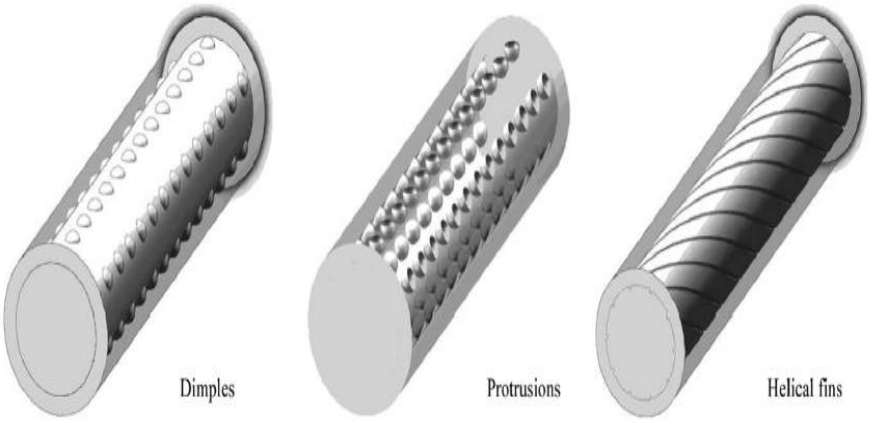

Figure 1.16. Schematic diagram of parabolic trough receiver with dimples, protrusions and helical fins [54].

c- Heat transfer enhancement by application of nanofluids

The use of nanofluids as HTF in solar PTC offers the advantage of basic improvement in the absorption of solar intensity and simultaneously increases the heat transfer in the receiver tube. CuO/water and Cu/Therminol VP-1 nanofluids have better heat transfer enhancement than other nanofluids. Recently the addition of nanoparticles in Thermions HTF for solar linear concentrating collectors was studied and their thermal efficiency of 62.7% was quoted [55].

Nanofluids exhibit novel and improved thermophysical heat transfer properties due to the influence of nanoscale size additives. The application of nanofluids as HTF increases the heat transfer coefficient of the fluid. Therefore, the heat transfer fluid absorbs the maximum solar radiation, which is concentrated onto the receiver. This results in an improved overall efficiency of the system. Many experimental studies have been conducted for the enhancement of heat transfer by using nanofluids.

Recently, Bellos et al. [56] numerically analyzed the thermal efficiency enhancement of solar PTCs by dimpled tube with sine geometry and addition of Al_2O_3 nanoparticles. The authors revealed that there was an increase in the thermal efficiency of 4.55% and 4.25% with geometrical modification and addition of nanofluids, respectively.

Kasaeian et al. [57] developed a pilot-scale of a solar PTC and carried out an experimental investigation using multi-walled carbon nanotube/oil-based nanofluids. The authors found that the overall efficiency of the trough collector was enhanced by about 4–5% and 5–7%, when 0.2% and 0.3% of nanofluids was used, instead of pure oil.

Bajestan et al.[58] experimentally investigated the application of nanofluids as HTF in solar heat exchangers. TiO_2/water was used as HTF in a straight tube to study the enhancement of heat transfer considering its usage in solar PTC and flat plate collector. The results indicated that the convective film heat transfer coefficient increased with an increase in nanoparticle concentration and flow Reynolds number. However, the increase in nanoparticle size had an inverse effect.

Kasaeian et al. [59] numerically analyzed the heat transfer enhancement in a solar PTC using Al_2O_3/synthetic oil nanofluids. They concluded that the heat transfer coefficient increases proportionally with an increase in the concentration of nanofluids but decreases with an increase in the operating temperature.

d- Selective coating

To enhance the performance of a PTC, the operating temperature has to be increased. To reduce heat loss, the outer surface of the metal absorber is covered with a selective coating to achieve a high solar absorbance and low thermal emittance [49][60]. An ideal selective coating for a PTC receiver should be inexpensive, easy to manufacture, chemically and thermally stable in air, have solar absorptivity ≥ 0.98 and thermal emittance ≤ 0.05 at 500 °C operating temperature [61]. Cheng et al [62] prepared dense Mo-Al_2O_3 thin films as a solar coating for absorber tubes. The researchers concluded that up to 400 °C, the coating was thermally stable for solar PTCs. Céspedes et al [63] developed a novel Molybdenum and Silica nitride (Mo–Si_3N_4) selective coating for high-temperature solar power applications. The authors optimized the thermal stability of the selective coating and reported that high solar thermal energy conversion efficiency was achieved with the selective coating. Barriga et al [64] developed a selective coating for high-temperature parabolic trough receivers. They prepared Molybdenum and Silica nitride (Mo–Si_3N_4) as selective coatings for a solar PTC receiver operating at a temperature of 600 °C. It was found that the selective absorber coating deposited on 4 m long tubes reached an absorbance of 95.2%. Kasaeian et al [65] examined the optical absorbance and thermal conductivity of three different coatings namely matt black painting, black chrome and black nickel-chrome coating for the absorber tube of a solar PTC. The results showed that the black chrome coating had a high absorbance of 98% and nickel chrome coating had better corrosion resistance.

e- Thermal storage

Selecting the appropriate storage medium is one of the main key technological issues for the future success of PTC technology, thermal storage improves efficiency and extended

life expectancy of components due to a reduction in thermal transients. Storage systems also facilitate the integration of solar thermal power plants into electrical grids by smoothing out fluctuations caused by variances in insolation, thus avoiding grid instability problems and reducing the requirements for fossil peak load backup capacity. Early systems utilized the heat transfer media itself as the thermal energy storage media, but due to the costs of oil, this is not economical [66]. A promising approach is the application of phase change materials, but additional experiments are required to obtain sufficient data for the layout of larger storage systems[67].

The application of solid media sensible heat storage is an attractive option regarding investment and maintenance costs. Cost-effective systems demand the utilization of inexpensive storage materials, which usually exhibit a low thermal conductivity. Essential for the successful development of a storage system is the sufficient heat transfer between the synthetic oil and the storage material[68].

Solid media sensible heat storage units were developed in the project ‘‘Midterm Storage Concepts”. Further Development of Solid Media Storage Systems’’ (PARASOL/WESPE) [69] funded by the German government.

f- Vacuum between the absorber and the glass cover

The air vacuum between the absorber and the glass cover greatly decreases convective and conductive heat losses and prevents the degradation of the selective coating at high temperatures [38].

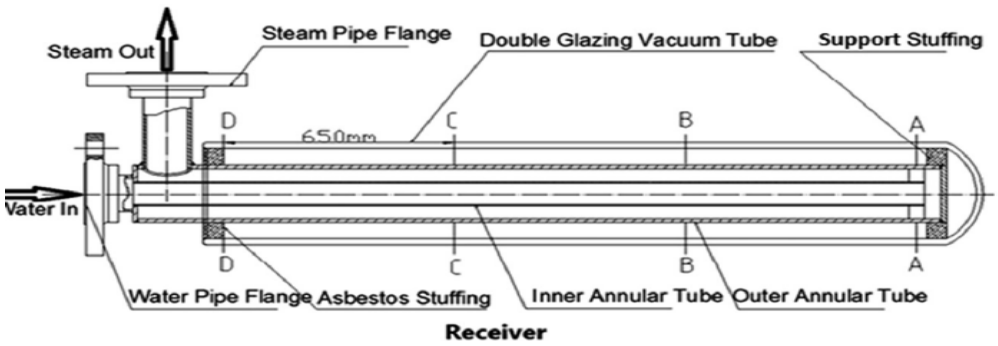

Figure 1.17. Double glazing’s U-type solar receiver [70].

Chen et al. [71] designed and theoretically analyzed the linear cavity receiver for a parabolic trough solar concentrator. The theoretical values were comparatively higher than the experimental values and the maximum theoretical and experimental efficiencies were found to be 56.20% and 51.20% respectively at 345 K inlet HTF temperature. The authors concluded that the use of glass cover minimizes the temperature difference in the receiver

and hence better thermal performance can be achieved in the linear parabolic trough system at medium temperature.

1.2.17.3 **Optical analysis of the PTC**

The optical efficiency of PTCs is affected by the absorption of the cylindrical absorber, the transmittance of the glass envelope, and the reflectivity of the mirror [72]. However, the mentioned optical properties depend on the incidence angle [73]. To calculate the optical efficiency of the PTCs, or calculate the solar flux distribution on the receiver, several models were published. These models are normally based on integration methods or simple geometric analytical methods [74]. Monte Carlo Ray-Tracing technique is demonstrated to be an effective numerical technique for the optical simulation of the concentrating characteristics of solar collectors [75][76][77]. But this method usually requires a high computing price, the runtime is long and causes floatation in the obtained results in case of multiple runs [78]. The technique is based on tracing a large number of solar rays. The pathway of every single ray depends on the emission, reflection, and absorption in the surface [76]. The reflection of the direction of the solar ray obeys the Fresnel law of optics [76]. He et al [77] established an integrated technique of MCRT and FVM to numerical study the photo-thermal process of a PTC. The MCRT was employed to determine the heat flux distribution, and FVM was employed to solve the fluid and heat transfer equations. The first integral of the focused solar flux density for a PTC was developed by Jeter [79] for the flat and cylindrical absorber, in his second paper Jeter [72] improved the model by considering the non-uniform source and additional practical transmission, reflection and absorption process. R. Grena [73] established an optical model, using a three-dimensional ray-tracing method, the model permits to carry out precise simulations and calculation of the efficiency and the distribution of solar radiation on the receiver. Tsai and Lin [80] [80] employed a ray-tracing method on MATLAB to optimize the solar thermal concentrator geometry of a PTC. Balghouthi et al [81] performed the photogrammetric techniques on MATLAB code for the optical evaluation of a PTC employed for a cooling system. The study of Liang et al [82] focused on developing and comparing three optical models basing on the ray- tracing technique to study the optics of a PTC. In each model, the way of initializing photons and the calculations of reflection, transmission, and absorption processes were different. Their run time, computational efforts and characteristics where compared. The objective of their comparison was to select the best

model for investigating and enhancing the optical performance of the parabolic trough collector. Huang *et al* [74] simulated the optical efficiency of the parabolic trough collector with and evacuated cylindrical receiver using the optical model that he developed. Boukhalfa et al [83] conducted a detailed optical investigation of PTC with an absorber plate, the ray-tracing technique was used.

1.3 Heat Pipes

Although discovered in the 1930s, the concept of heat pipe has only really been adopted in the last few decades, in particular in the aerospace, railway or power electronics sectors.

Patented in 1942, the heat pipe was forgotten until the early 1960s when it was rediscovered for the needs of space technology. Also sometimes called "Heat-Pipe", its ancestor is the Perkins tube, a kind of closed-circuit boiler invented in the 19th century by A.M. and J. Perkins. Two families of heat pipes are now mature: capillary heat pipes and two-phase thermosiphons.

For heat conduction, different systems are possible such as metals like copper and aluminum. However, the heat pipes operating system is based on the thermal heat transfer mainly by the phase transition of a fluid (latent heat), makes it possible to have a particularly interesting efficiency in the transport of heat flows. The main types of heat pipes generally used are capillary heat pipes and heat pumps and two-phase thermosiphons. Heat pipes are thermal systems that can transport a quantity of heat equal to several times the amount of heat that would otherwise be lost in the process. Hundreds of thousands of times that transported by a solid and homogeneous metallic conductor of the same volume under the same temperature difference.

The function of the heat pipe is to transport heat from a hot spot to a cold spot. The hot spot is in contact with the evaporator of the heat pipe and the cold source in contact with the condenser. The liquid evaporates at the evaporator and the steam is condensed in the condenser. While the steam moves under the pressure difference at the evaporator. And to the condenser, the condensate returns to the evaporator under the effect of forces imposed by the system. These are most often-capillary forces developed in a porous medium that lining the inside wall of the heat pipe (capillary heat pipe) or gravity forces (two-phase thermosiphon).

1.3.1 Two-phase thermosiphons

Two-phase thermosiphon are heat pipes in which the motor ensuring the return of the liquid is not the capillary effect, but gravity. This is only possible when the condenser is above the evaporator.

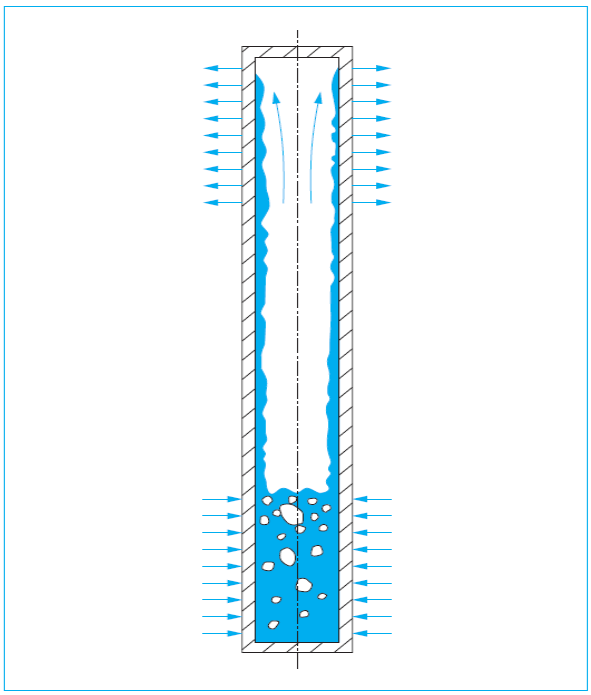

Figure 1.18. Principle of a two-phase thermosiphon[84]

1.3.1.1 Principle of operation

The pressure evolution is very different in a thermosiphon. Indeed, due to the absence of capillary pressure, the static pressures of the vapor phase and the liquid phase are identical in each section. Besides, the pressure in the liquid phase is equal to the sum of the force-related pressure gravity and losses of expenses related to the flow. The driving force of the flow represented by gravity being the thickness of the liquid films is generally very important; the thickness of the liquid films adapts itself to induce pressure drops to compensate for this driving force.

For a two-phase thermosiphon, the limitations of transfer capacity are not related to the driving forces of the flow as long as the flow has a sufficient inclination concerning gravity (greater than 10^{o}).

1.3.2 Capillary heat pipe

Capillary heat pipe is a thermosiphon with capillary structure, such as grooving, the role of the grooving is only to improve the local performance (exchange coefficient, homogenization of the condensate film, stabilization of the liquid-vapor interface, etc.).

Thermosiphons are also widely used in the industrial field with smooth internal walls when you are looking for a minimum cost price.

However, the use of a capillary network improves the functioning and increases the performance of the heat pipe. The only capillary network used industrially in this type of heat pipe is the internal grooving of the tubes. The advantages of internal grooving, compared to smooth pipe, are first and foremost to significantly increase the exchange coefficients of evaporation and condensation, and then to have an internal more stable operation.

1.3.2.1 **Principle of operation**

The length of a heat pipe is divided into three parts: the evaporator section, adiabatic (transport) section and condenser section, the existence of the adiabatic section depends on specific applications and design of the heat pipe [85]. The heat pipe has the function of transporting heat from a hot source (evaporator) to a cold source (condenser). The liquid evaporates on the evaporator and the vapor condenses on the condenser. The resulting vapor pressure drives the vapor through the adiabatic section to the condenser, where the vapor condenses, releasing its latent heat of vaporization to the provided heat sink, the condensed liquid returns to the evaporator through the wick driven by capillary force [86][87] developed in a porous medium lining the inner wall of the heat pipe. This capillary pressure gradient circulates the fluid against the liquid and vapors pressure losses, and adverse body forces such as gravity or acceleration, the friction cause changes in the vapor pressure along the heat pipe [87]. Thermosiphon heat pipes depend on the gravitational forces to return the condensate to the evaporator to continue the cycle. Different types of working fluids such as water, acetone, methanol, ammonia or sodium can be used in heat pipes based on the required operating temperature [85].

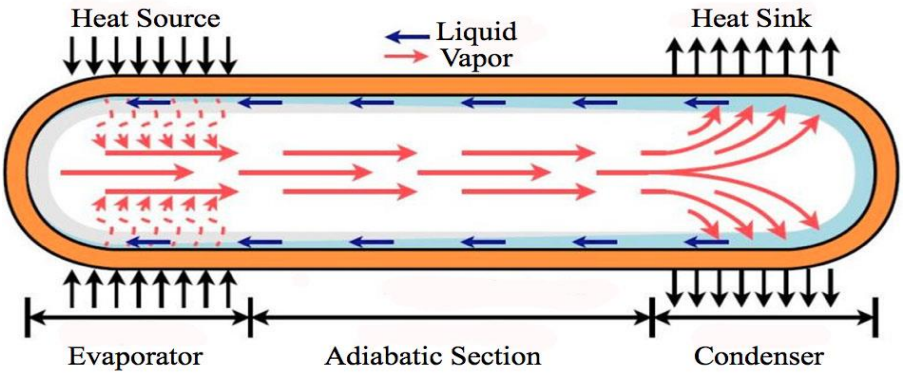

Figure 1.19. Schematic view of a heat pipe[88].

1.3.3 Literature review on heat pipe for solar applications

Vasiliev, Grakovich et al [89] have developed a mathematical model for a solar collector with a heat pipe. They demonstrated that the choice of the heat pipe or thermosiphon depends mainly on the heat transfer coefficient in the condenser. It has also been shown that the use of heat pipes rather than thermosiphons results in a 10-17% increase in efficiency at defined flow rates that are appreciable to heat fluxes.

Ismail and Abogderah [90] studied the performance of a heat pipe solar collector. The instantaneous efficiencies are higher than the conventional collector when the heat pipes reach their operating temperatures.

Rittidech et al [91] investigated the plate collector adopting a curved heat pipe and analyzed the influence of solar radiation and ambient temperature on the collector's performance. This analysis incorporates the natural forces of gravity and capillary action. It has additional benefits such as corrosion-free operation.

Muneer et al [92] has analyzed the potential of solar thermal energy for Turkish textile industries considering life cycle assessment and relevant economics of solar water heater.

Shafahi et al [93] used analytical models developed by Vafai et al [87,86] to investigate the thermal performance of rectangular and disk-shaped heat pipes using nanofluids as the working fluids. Al_2O_3, CuO, and TiO_2 were considered in their work. They noticed a significant enhancement in thermal performance of a flat-shaped heat pipe using nanofluids. The study showed the small size nanoparticles present in the working fluid are the most effective in the enhancement of the flat-shaped heat pipe. Their results also showed that the presence of an optimum wick thickness and nanoparticles concentration levels maximizes the heat removal capability of a flat-shaped heat pipe.

Huminic et al [95] conducted an experimental investigation of the thermal performance of thermosiphon heat pipe using iron oxide nanoparticles added to water as a working fluid. Their results showed that the presence of iron oxide nanoparticles in water improves the thermal performance of the heat pipe.

Mobin Arab an Ali Abbas [96] developed a semi-dynamic underwater sensor model for water heating. The effects of using water, ammonia, acetone, methanol and pentane as working fluids of the heat pipe were discussed. Water was identified as the best working fluid among the others. The variation of the thermal resistance and the critical heat flux of the heat pipes due to the variation of the meteorological conditions were presented and discussed. In addition, it has been demonstrated that considerably higher performance of the

solar water heater (up to 84%) is achievable by only improving the properties of the working fluid. Also, the modification of the working fluid can lead to an improvement of about 50% in the saving of the solar water heater.

Yulan et al[97] analyzed the heat transfer of the compound parabolic concentrator CPC heat pipe vacuum solar collector and calculated and compared the efficiencies of several collectors.

Xuesong et al [98]has computed the thermal loss coefficient and efficiency of the CPC heat pipe collector.

Yunfeng et al[99] combined a composite parabolic concentrator with a heat pipe plate collector, adopted an iodine-tungsten lamp to simulate the solar irradiance and performed experimental investigation and comparison with the CPC heat pipe plate solar collector and ordinary plate solar collector by focusing on the collector efficiency.

Wang, Zhu et al[100] created and investigated a tracking system for a compound parabolic concentrator (CPC) with a concentration ratio of 2.3, the CPC was combined with a heat pipe evacuated tube-shaped receiver and crank rod transmission mechanism. They also conducted a theoretical investigation to simulate the solar incident angles and the optical performance of the tracking CPC collector. Additionally, the thermal performance was experimentally investigated at different operation modes.

1.3.4 The literature on heat pipe integrated to parabolic trough collector

Replacing the absorber tube by a heat pipe in a PTC is an excellent idea to improve the collector's overall efficiency thanks to the high thermal performance of the heat pipe. The use of a heat pipe as a receiver for parabolic trough collector was proposed for the first time in 2008 by Zhan et al [101]. They developed and investigated a medium temperature (250~500 °C) heat pipe receiver for a PTC and carried out the feasibility study on the receiver. The results showed that the heat pipe receiver was flexible, easily maintained, with low manufacture cost and could be reliable in the temperature and heat flux conditions of PTC with a high heat collect efficiency. Zhang Weiwei et al [102] performed Analysis of the heat transfer properties for the Heat-Pipe evacuated tube solar collector system in the parabolic trough. In this study, a heat transfer fluid's temperature is raised to approximately 200 °C using a parabolic trough solar collector system with a heat pipe evacuated tube. The system performance is also influences by the type of gases in the annulus space. The kind of gases in the annulus space also affect how well the device works. The temperature of the heat transfer fluid and the gases (air, hydrogen, and argon) in the annulus space affect how

much heat is lost by the collector. Additionally, inert gases with high thermal condition coefficients, like hydrogen, cause the collector to lose more energy. El Fada et al [103] established a theoretical model to examine the performance of a refrigeration system power-driven with a parabolic trough collector combined with a heat pipe. The system was demonstrated to have high efficiency and heat flow. Zhang et al [104] conducted an experimental investigation of a U-type natural circulation heat pipe system integrated to a parabolic trough collector for steam generation. The obtained results proved that the system can generate mid-temperature steam up to a pressure of 0.75 MPa. Zhang et al [70] experimentally investigated the heat losses of a U-type solar heat pipe receiver of a parabolic trough collector for steam generation. Their results demonstrated that for this kind of U-type receiver, the characteristics of the structure are essential to determine the thermal efficiency. A new desalination system using a parabolic trough collector coupled with an evacuated heat pipe was industrialized by Mosleh et al [105]. Their results revealed that filling the gap between the heat pipe and twin-glass evacuated tube with oil rather than aluminum foil pieces can maximize the amount of production. Ismail et al [106] replaced a PTC heat absorber with an evacuated porous heat pipe tube. The system was studied in details; they explained the differences between the theoretical and experimental results by the fact that a manual adjustment was used and better conformity will be achieved using an automatic tracking system. The United States department of energy launched a project of high temperature heat pipe receiver for parabolic trough collectors, from 1 October 2015 to 30 Sept 2018. The work was presented in the 2016 CSP program summit by Stephen Obery [88]. The objective of the project was to enable parabolic trough collector to operate at 750°C, to reduce system complexity, to mitigate unknowns associated with heat transfer fluid, and enable the use of high efficiency power cycles.

Performance evaluation of novel heat pipe-Assisted thermal storage system with parabolic trough solar collector using nanofluid was carried out by vednath P et al[107]. The final remark of this study has been done with the comparison of the present system with the existing and similar kinds of thermal energy storage systems. For the same charging cycle time and same climatic conditions, the compared value of specific heat storage capacity is 67% higher as compared to the average value of other considered systems. The comparison of their system with the existing and related types of thermal energy storage systems has been done as the study's concluding observation.

Hassan Fathabadi[108] investigated the performance of a novel low cost evacuated tube and flat-plate solar collector with Two-phase closed thermosiphon (TPCT) heat pipe and solar tracker.

Peak thermal efficiencies of 73.3% are offered by the built trough solar collector,

which ishigher than those of the evacuated tube collector ETC20 (71.6%). The thermal eff iciency curve of the constructed parabolic trough collector is substantially flatter than that of the other two commercial solar collectors (ET C-20 and F PC-A 26). The suggested solar collector has a much higher power production density (808.3 W/m2) than the evacuated tube sun collector ETC-20 (710.05 W/m2) and the flat plate solar collector FPC A26 (754.86 W/m^2). The suggested parabolic trough solar collector's price to peak output power ratio is 0.4467 €/W, which is considerably cheaper than 0.8346 €/W of the evacuated tube solar collector ETC-20's.

Weiwei Zhang et al [109] examined the effects of installation and tracking errors on the optical performance of a heat pipe evacuated for parabolic trough collector. The heat flux distribution at the focal plane was determined, and a test bench for the parabolic trough concentrator's azimuth-elevation axis manual tracking mechanism was designed and constructed. The largest relative error was 2.69% when the optical simulation findings were compared to the test results to ensure their accuracy. The largest inaccuracy was 16.23% when the simulation results were compared to those estimated in the literature. Even after longitudinal incidence angles and vertical installation defects were discovered, simulation results demonstrate that the circumferential heat flow of the receiver is still symmetrically distributed.

1.4 Conclusion

The review started by presenting the different techniques used for the solar radiation measurement, the techniques mentioned are ground measurement and some mathematical models for the estimation of beam radiation. The literature review provided also an update on the main research works on the parabolic trough collector, different components of the parabolic trough collector and the techniques used to improve the performance of the PTC. The chapter also gave a detailed overview of heat pipe including a brief history of the technology, principle of operations, types of the heat pipe and heat pipe's applications for solar energy.

2. CHAPTER 02: OPTICAL MODELING

2.1 Introduction

The total energy absorbed by the receiver depends on the solar radiation reflected by the parabolic mirrors and transmitted by the glass cover. In this study, the optical efficiency of the parabolic trough receiver was calculated. The transmittance of the upper and the lower semi-cylindrical parts of the glass envelope was calculated by analyzing the optical path of the incident solar rays. The effective transmittance-absorptance product $(\tau\alpha)_{eff}$ was determined taking into account multiple reflections-absorptions of solar rays, into the glass cover and between the glass cover and the absorber cylinder before their absorption. To estimate the direct solar radiation on a horizontal or inclined plane, simple empirical models can be used. The model used in this paper is well adapted to our region.

2.2 Average transmittance of the upper part of the receiver $\bar{\tau}_U(\theta)$

2.2.1 Optical properties of a cylindrical cover glass

Figure 2.1 represents the optical path of the solar ray until it reaches the absorber cylinder. Traversing the glass cover, the solar ray undergoes a series of reflections - absorptions - transmissions before it reaches absorber and some rays will miss it:

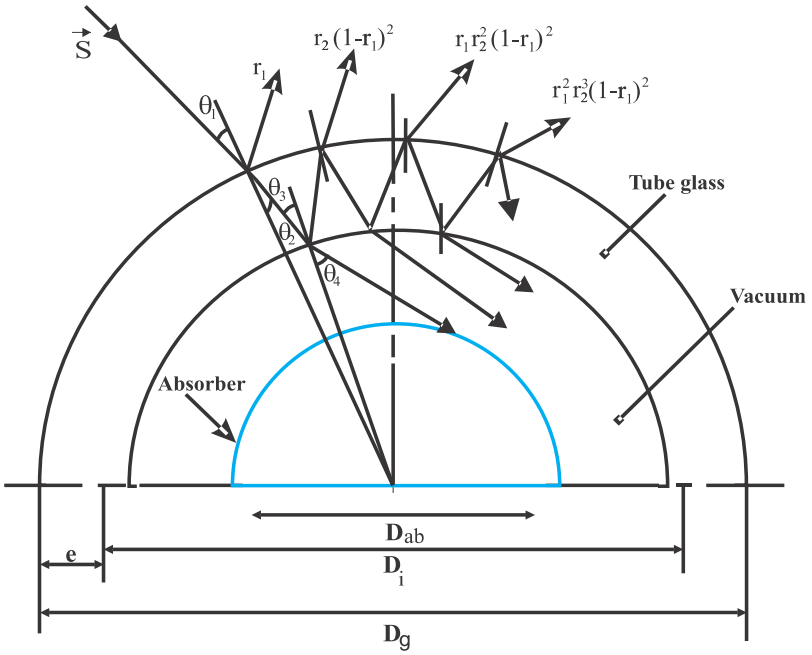

Figure 2.1. Receiver cross section and ray tracing application

According to the results of Fresnel's work, the optical proprieties of a glass cover, for a non-polarized light ray, are given by the average of its parallel and perpendicular components.

therefore, at the first interface of the glass cover, the fraction of radiation reflected will be given by,[10]:

$$r_1 = \frac{(r_{1\parallel} + r_{1\perp})}{2} \tag{2.1}$$

Where:

$$r_{1\parallel} = \frac{\tan^2(\theta - \theta_2)}{\tan^2(\theta + \theta_2)} \tag{2.2}$$

$$r_{1\perp} = \frac{\sin^2(\theta - \theta_2)}{\sin^2(\theta + \theta_2)} \tag{2.3}$$

And from Snell's law we have:

$$n_1 \sin(\theta) = n_2 \sin(\theta_2) \tag{2.4}$$

Therefore, we obtain:

$$\theta_2 = \arcsin\left[\frac{n_1}{n_2} \sin(\theta)\right] \tag{2.5}$$

For the second interface of the glass cover, we have:

$$r_2 = \frac{(r_{2\parallel} + r_{2\perp})}{2} \tag{2.6}$$

Where:

$$r_{2\parallel} = \frac{\tan^2(\theta_3 - \theta_4)}{\tan^2(\theta_3 + \theta_4)} \tag{2.7}$$

$$r_{2\perp} = \frac{\sin^2(\theta_3 - \theta_4)}{\sin^2(\theta_3 + \theta_4)} \tag{2.8}$$

The parallel and perpendicular components of the transmittance are deduced by analyzing the optical path of the solar ray, so we obtain [10],[110]:

$$\tau_\parallel = \tau_a \frac{(1 - r_{1\parallel})(1 - r_{2\parallel})}{1 - \tau_a^2 r_{1\parallel} r_{2\parallel}} \tag{2.9}$$

$$\tau_\perp = \tau_a \frac{(1 - r_{1\perp})(1 - r_{2\perp})}{1 - \tau_a^2 r_{1\perp} r_{2\perp}} \tag{2.10}$$

And

$$\tau(\theta) = \frac{(\tau_\parallel + \tau_\perp)}{2} \tag{2.11}$$

The absorption of radiation in a partially transparent medium is described by Bouguer's law, [10]:

$$\tau_a = e^{-k\,l} \tag{2.12}$$

Figure 2.2 represents the optical distance for a tubular cover glass. The optical path is given by the following formulas[111][112]:

$$l = \frac{d}{\cos(\alpha_1)} \tag{2.13}$$

And

$$d = \frac{D}{2}\left[\cos(\theta_2) - \left(1 - \frac{2e}{D_g}\right)\cos(\theta_3)\right] \tag{2.14}$$

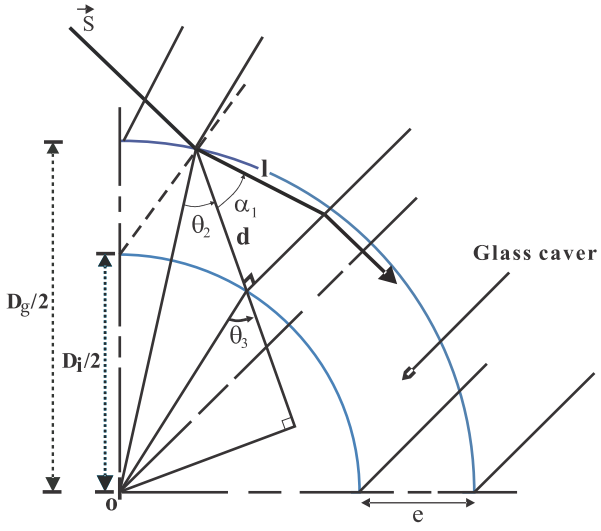

Figure 2.2. Schematic representation of optical distance for a cylindrical cover glass

The average transmittance is described as a fraction between the transmitted and incident solar flux. The average transmittance of the cover is given by [112]:

$$\bar{\tau}_U(\theta) = \frac{1}{G_i}\int_{\Phi_1}^{\Phi_2} dG_a = \frac{1}{D_i\,L\,I_b\cos(\theta_a)}\int_{\Phi_1}^{\Phi_2} D\,L\,I_b\,\tau(\theta)\cos(\theta)\,d\Phi \tag{2.15}$$

After traversing the glass cover some rays will miss the absorber. The energy collected by the absorber will be calculated by integration over the useful surface.

Figure 2.3 presents the integration limits of the radiation received by the cylindrical absorber, depending on the relative position of the Sun.

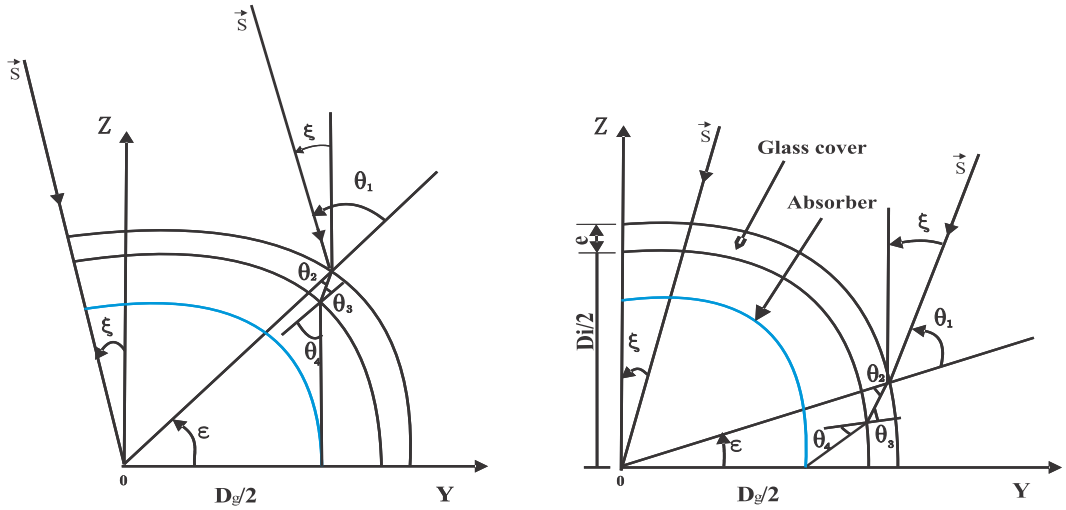

Figure 2.3. The integration limits of the radiation transmitted by the tube and received by the absorber

The integration limits are given by [112] :

$$\begin{cases} \Phi_1 = \xi \\ \Phi_2 = \xi - \theta \end{cases} \tag{2.16}$$

The incidence angle $\theta 1$ is the solution of the following system of equations[112]:

$$\begin{cases} \dfrac{\sin(\theta)}{\sin(\theta_{2)}} = 1 - \dfrac{2e}{D} \\ \dfrac{\sin(\theta_4)}{D} = \dfrac{\cos\left[\theta - \xi - \theta_4 + \left(\arcsin\left(\frac{n1}{n2}\sin\theta_4\right)\right) - \arccos\left(\frac{n1}{n2}\sin\theta\right)\right]}{D - 2e} \end{cases} \tag{2.17}$$

The projections of the incidence angle are given by [112]:

$$\tan(\xi) = \frac{\cos(h)\sin(a+h)}{\sin(h)} \tag{2.18}$$

$$\tan(\eta) = \frac{-\cos(h)\cos(a+\gamma)}{\sin(h)} \tag{2.19}$$

2.2.2 Incidence angle

The PTC receiver is exposed to solar radiation horizontally (tilt angle β equal to zero), and an azimuth angle γ_s, from the south direction. If the PTC is oriented to the North-South direction the azimuth angle is null, in the case of East-West alignment γ_s is equal to 90°. Figure 2.4 and 2.5 represent the positioning of the receiver for both East-West and North-South alignments, where $\vec{s}$ is the unit vector of the solar ray and $\vec{n}$ the unit vector normal to the glass cover.

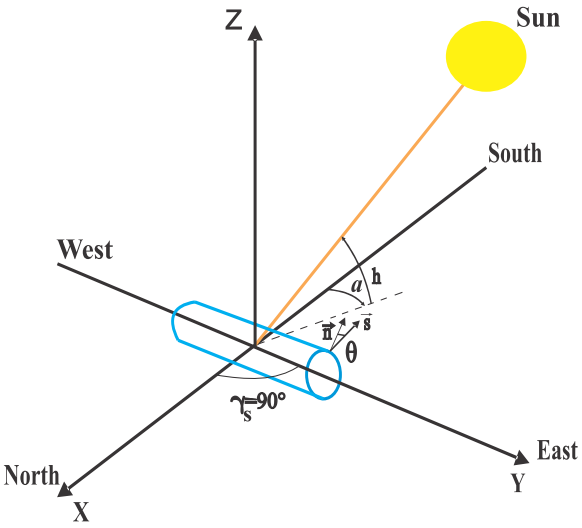

Figure 2.4. Schematic representation of a tube receiver in case of E-W alignment

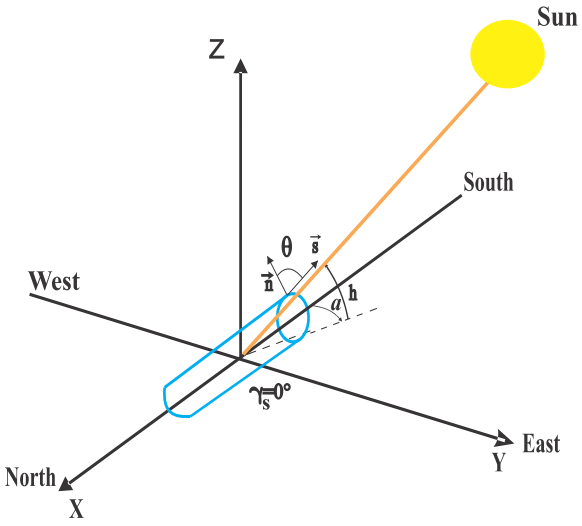

Figure 2.5. Schematic representation of a tube receiver in case of N-S alignment

The cosine of the angle of incidence θ is given by [10]:

$$\cos(\theta) = \cos(h)\sin(a+\gamma_s)\sin(\Phi) + [\sin(\beta)\cos(h)\cos(a+\gamma_s) + \cos(\beta)\sin(h)]\cos(\Phi) \quad (2.20)$$

The cosine of the angle of incidence θ_a in absence of the glass cover is given by[111]:

$$\cos(\theta_a) = -\cos(h)\sin(a+\gamma_s)\sin(\beta') + [\sin(\beta)\cos(h)\cos(a+h) + \cos(\beta)\sin(h)]\cos(\beta') \quad (2.21)$$

2.2.3 The transmittance of the lower part of the receiver

The longitudinal and transversal incidence angles were obtained by projecting the reflected solar ray on the longitudinal and transversal plane of the parabolic trough, respectively.

2.2.3.1 Transversal plane

Figure 2.6 represents the longitudinal plane of the parabolic trough collector with the sun rays considered to be parallel. The solar tracking system is assumed to be perfect (tracking errors are neglected), this hypothesis allows us to consider that transversal incidence angle to be equal to zero (ξ=0).

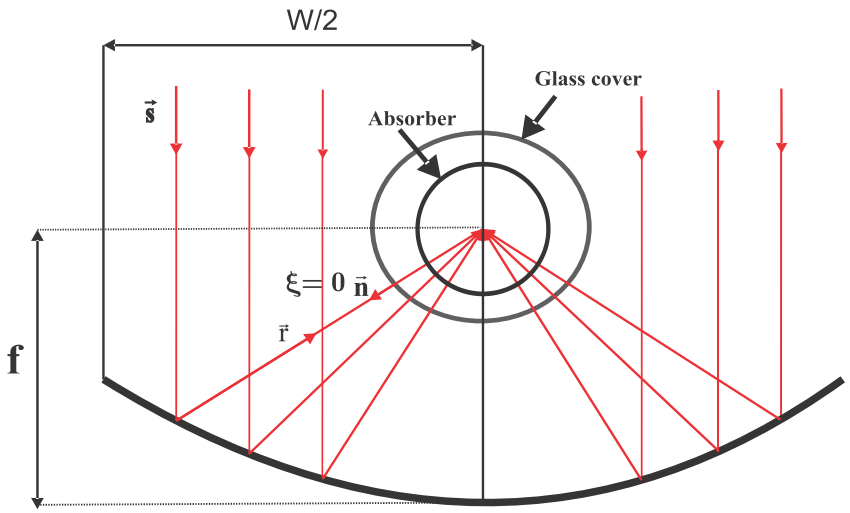

Figure 2.6. Transversal plane of parabolic trough collector

2.2.3.2 **Longitudinal plane**

Figure 2.7 represents the path for the reflected solar ray until it reaches the absorber. The reflected solar rays from the parabolic mirror will go through multiple reflections and refractions inside the glass cover medium. Some energy will be reflected out of the glass cover, and the rest will be transmitted and absorbed by the absorber.

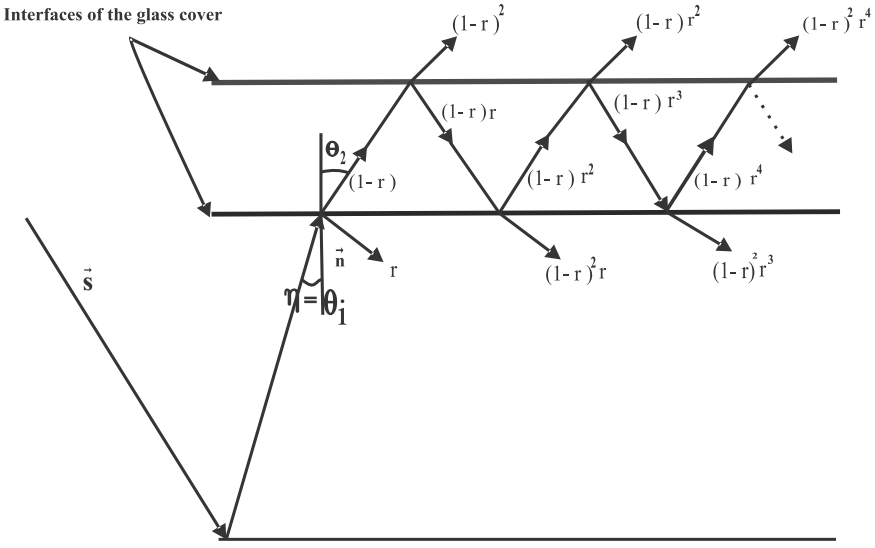

Figure 2.7. The path of the reflected ray in the longitudinal plane of parabolic trough collector

2.2.4 **Angle of incidence**

By analysing the reflected solar ray using vectorial analysis, which is based on vectors, we can deduce the angle of incidence for both East-West and North-South alignment.

2.2.4.1 **In the case of North-South alignment**

Figure 2.8 And 2.9 represents the tracking angle in case of North-South alignment and the receiver in the case of inclined setting respectively.

The unit vector perpendicular to the optical axis and the unit vector of the optical axis are represented in the figure 2.8.

The unit vector of the sun ray is given by:

$$\vec{s}\begin{cases} cos(h)\,cos(a) \\ cos(h)\,sin(a) \\ sin(h) \end{cases} \qquad (2.22)$$

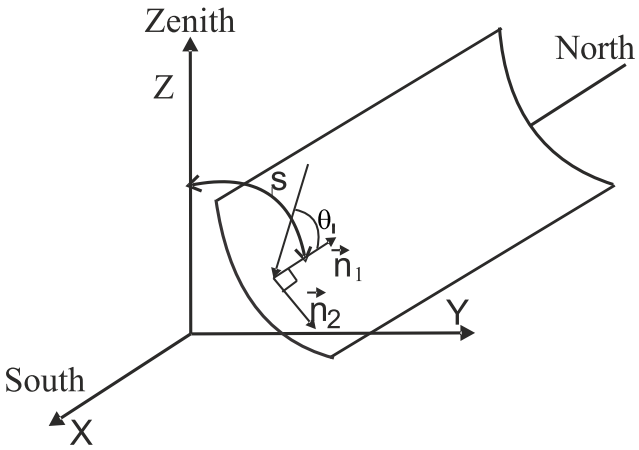

Figure 2.8. Schematic representation of tracking angle in case of North-South alignment

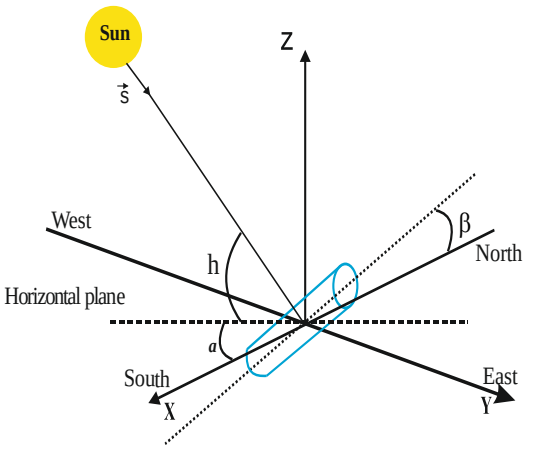

Figure 2.9. Schematic representation of the receiver

The unit vector perpendicular to the optical axis is given by (see figure 2.8):

In the morning:

$$\overrightarrow{n_2}\begin{cases} 0 \\ cos\,ş \\ -\,sin\,ş \end{cases} \qquad (2.23)$$

In the afternoon:

$$\overrightarrow{n_2}\begin{cases} 0 \\ cos\,ş \\ sin\,ş \end{cases} \qquad (2.24)$$

The tracking can be considered as perfect if the vector $\overrightarrow{n_2}$ and the unit vector of the solar ray are perpendicular which means that $\vec{s}\,.\overrightarrow{n_2} = 0$.

In the morning, we have:

$$\vec{s}\,.\overrightarrow{n_2} = cos(h)\,sin(a)\,cos(ş) - sin(h)\,sin(ş) = 0 \qquad (2.25)$$

In the afternoon, we have:

$$\vec{s}\,.\overrightarrow{n_2} = cos(h)\,sin(\,a)\,cos(ş) + sin(h)\,sin(ş) = 0 \tag{2.26}$$

The tracking angle (ş) which equal to the zenith angle is given by:

$$ş = arctan\left((-1)^n \frac{sin\,a}{tan\,h}\right) \tag{2.27}$$

With n= 1 before mid-day and n=2 after mid-day.

The unit vector of the optical axis $\vec{n}_1$ is given by:

In the morning:

$$\overrightarrow{n_1}\begin{cases} \sin(\beta\,) \\ +\,sin(ş)\cos(\beta\,) \\ cos(ş)\,\cos(\beta\,) \end{cases} \tag{2.28}$$

In after noon:

$$\overrightarrow{n_1}\begin{cases} \sin(\beta\,) \\ -\,sin(ş)\cos(\beta\,) \\ cos(ş)\,\cos(\beta\,) \end{cases} \tag{2.29}$$

The angle between the sunray and the optical axis is given by:

In the morning:

$$\cos(\theta_i) = \overrightarrow{n_1}.\vec{s} = cos(h)\,cos(a)\sin(\beta\,) + \cos(h)\sin(a)\,\sin(ş)\,\cos(\beta\,) + \\ +\sin(h)\,\cos(ş)\,\cos(\beta\,) \tag{2.30}$$

In the afternoon:

$$\cos(\theta_i) = \overrightarrow{n_1}.\vec{s} = cos(h)\,cos(a)\sin(\beta\,) - \cos(h)\sin(a)\,\sin(ş)\,\cos(\beta\,) + \\ +\sin(h)\,\cos(ş)\,\cos(\beta\,) \tag{2.31}$$

In case of the PTC receiver exposed to solar radiation horizontally (tilt angle β equal to zero).

2.2.4.2 **For the East-West axis orientation**

Figure 2.10 and 2.11 represent the schematic representation of tracking angle in case of East-West alignment and the schematic representation of the receiver positioning, respectively.

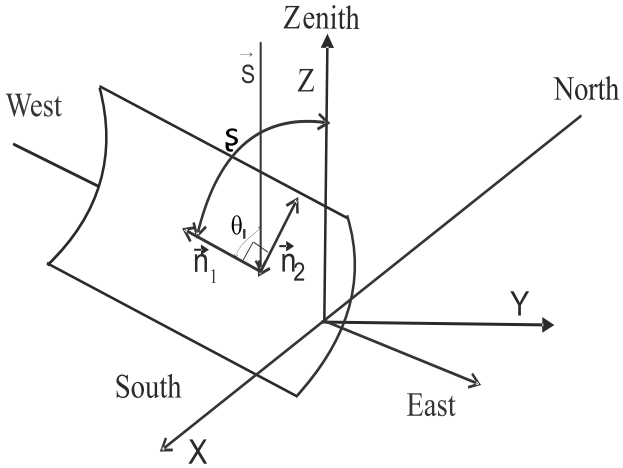

Figure 2.10. Schematic representation of tracking angle in case of East-West alignment

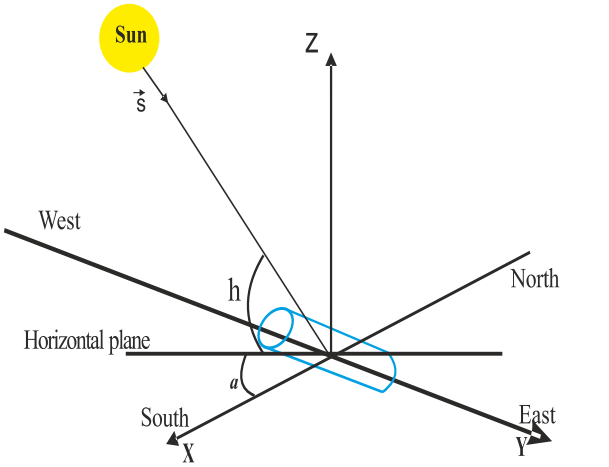

Figure 2.11. Schematic representation of the receiver

The unit vector of the solar ray is given by equation (2.22).

The unite vector perpendicular to the optical axis is given by:

$$\overrightarrow{n_2}\begin{cases}-\cos ş \\ 0 \\ \sin ş\end{cases} \tag{2.32}$$

In case $\overrightarrow{n_2}$ and the unit vector of the solar ray are perpendicular, the tracking can be considered as perfect.

$$\vec{s}.\overrightarrow{n_2} = -\cos(ş)\cos(\mathrm{h})\cos(a) + \sin(ş)\sin(\mathrm{h}) = 0 \tag{2.33}$$

Which means that the tracking angle is given by:

$$ş = \arctan\left(\frac{\cos a}{\tan \mathrm{h}}\right) \tag{2.34}$$

The unit vector of the optical axis is given by:

$$\overrightarrow{\overrightarrow{n_1}}\begin{cases}\sin ş \\ 0 \\ \cos ş\end{cases} \tag{2.35}$$

The angle between the sunray and the optical axis given by:

$$\cos(\theta_i) = \overrightarrow{n_1}.\vec{s} = \cos(\mathrm{h})\cos(a)\sin(ş) + \sin(\mathrm{h})\cos(ş) \tag{2.36}$$

2.2.4.3 **End loss**

End losses occur at the ends of the receiver, where, for a nonzero incidence angle, some length of the absorber tube is not illuminated by solar radiation reflected from the mirrors.

Figure 2.12 depicts the occurrence of end losses for an receiver with a nonzero angle of incidence [113].

The end loss ratio (M) which is the ratio between the non-illuminated lengths ($E = f.\tan(\theta_i)$) and the total length of the absorber is given by:

$$M = \frac{f.\tan(\theta_i)}{L} \tag{2.37}$$

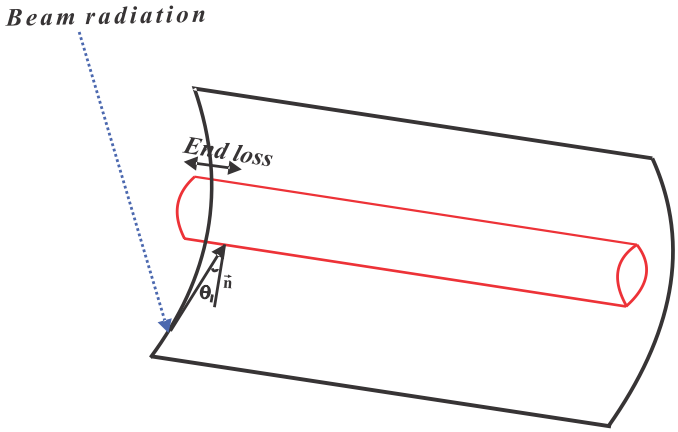

Figure 2.12. End loss from the receiver

The transmittance of the lower part of the receiver is given by:

$$\tau_L(\theta_i) = \frac{(L - E).\tau(\theta_i)}{L} \tag{2.38}$$

For this lower part of the receiver, the expression of the transmittance of the glass cover $\tau(\theta)$ is the same as for the upper part, but the optical path of the solar ray is different because the transversal incidence angle is neglected. Therefore, the optical path is given by[112]:

$$l = \frac{e}{\cos(\theta_2)} \tag{2.39}$$

2.2.5 Average transmittance of the whole receiver

The average transmittance of the receiver takes into account both the transmittance of the lower part and the upper part of the glass cover, and it's calculated by weighted average:

$$\bar{\tau}(\theta) = \frac{I_b D\, L\, \bar{\tau}_U(\theta) + I_b(a - D)L\, \tau_L(\theta_i)}{I_b\, a\, L} \tag{2.40}$$

2.2.6 Effective transmittance-absorptance product

Figure 2.13 shows the multiple reflections-absorptions of solar rays between the glass cover and the absorber cylinder. Some solar rays will be reflected the glass cover and the rest will be transmitted by the absorbed to heat the fluid.

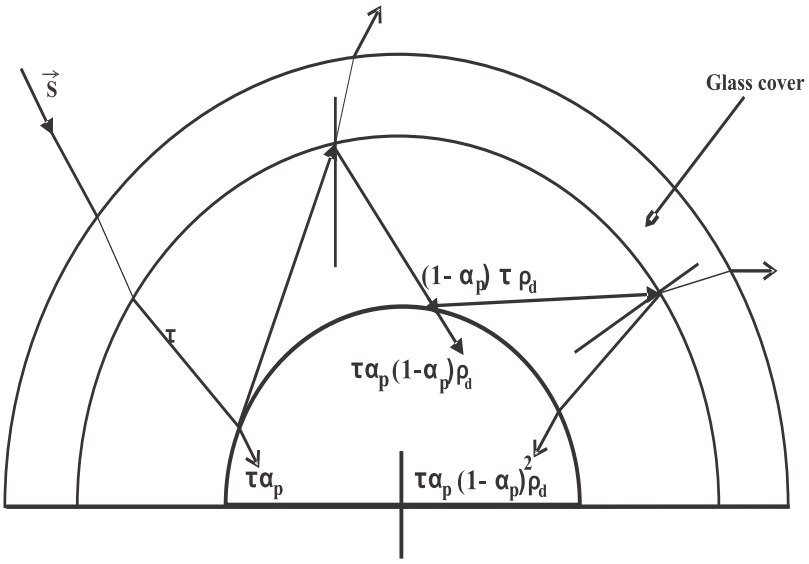

Figure 2.13. Multiple absorptions – reflections between the absorber and the glass cover.

2.2.7 The optical efficiency of the parabolic trough collector

The optical efficiency is given by:

$$\eta_0 = \frac{(\tau\alpha)_U\ D\ L + (\tau\alpha)_L\ \gamma\ \rho\ (a - D)\ L}{I_b\ a\ L} \tag{2.41}$$

The effective transmittance-absorptance product of the upper and the lower part of the receiver are given by, successively:

$$(\tau\alpha)_U = \frac{(\tau\alpha)_U\ \alpha_p}{1-(1-\alpha_p)\rho_d(\theta)} \tag{2.42}$$

$$(\tau\alpha)_L = \frac{(\tau\alpha)_L\ \alpha_p}{1-(1-\alpha_p)\rho_d(\theta)} \tag{2.43}$$

The analysis of the optical path of an incident ray shows that the summation of the quantities absorbed successively, the effective transmittance-absorptance product is given by,[10].

$$(\tau\alpha)_{eff} = \frac{\bar{\tau}(\theta)\alpha_p}{1-(1-\alpha_p)\rho_d(\theta)} \tag{2.44}$$

The total absorptivity in the function of the incidence and is deduced from the normal total absorptivity α_{p0} and it's given by[114]:

$$\alpha_p = \alpha_{p0}\cos(\theta_i)^{0.25} \tag{2.45}$$

ρ_d can be approximated by the beam transmittance at an incidence angle of 58 °, [10].

The beam solar radiation on the horizontal plan is estimated using the model of Brichambraut-Capderou,[26] (see equation 1.5).

2.3 Conclusion

In this chapter, the optical analysis of the parabolic trough collector was conducted, the adopted method is based on analyzing the optical path of the solar ray until it reaches the cylindrical absorber. The average solar transmittance of the upper part of the receiver (the part facing the sky) was calculated for different incident angles using a numerical integration technique. The transmittance of the lower part of the receiver was also calculated for different longitudinal angles taking into account the end losses. The proposed model is very efficient as it allows to calculate the optical efficiency with lower computing cost, and shorter runtime. The model takes into consideration multiple reflections of solar rays between the glass cover and the absorber cylinder before their absorption by the absorber. The model takes also into account the incident angle variation, end effects, and both trough alignments. Even though the lower part of the receiver has a higher transmittance because it receives concentrated solar rays with small incidence angle, the transmittance of upper semi-cylindrical part of the receiver was calculated because it receives solar rays coming directly from the Sun. By calculating the effective absorptance-transmittance product ($\tau\alpha$) for different incident angles, better accuracy in the optical efficiency will be achieved.

3. CHAPTER 03: THERMAL MODELING

3.1 Introduction

The improvement of the performance of the PTC leads to the increase of energy conversion and therefore high temperatures can be reached. The coupling of a parabolic trough collector with a heat pipe allows achieving higher temperatures than those achieved with an ordinary receiver tube by increasing the efficiency of the system. The configuration offers also the possibility to the parabolic trough collectors to be mounted in parallel and arranged horizontally or inclined. Inclined arrangement setting makes use of gravity assistance to bring the condensed fluid back to the evaporator. In this chapter, performance analysis of a heat pipe absorber integrated into a parabolic trough collector was performed; energy balances were applied in each component of the system. The system of partial differential equations describing the transient behavior of the system was established.

3.2 Description of the system

As shown in Figure 3.1 the heat pipe is placed all along the focal length of the parabolic trough collector.

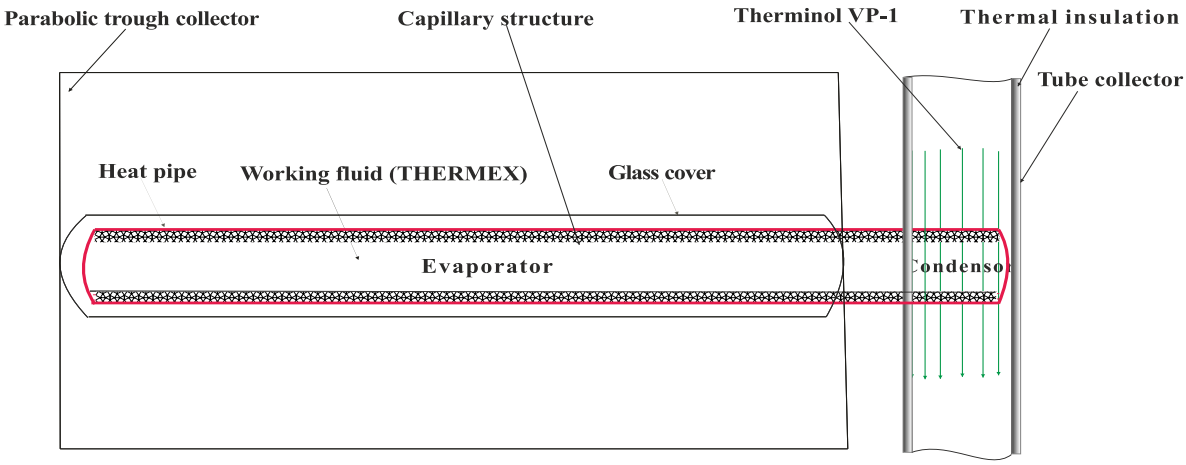

Figure 3.1. Schematic representation of heat pipe receiver for parabolic trough collector

The heat pipe is placed all along the focal length of the parabolic trough collector .The heat pipe's operating principle is based on a heat exchange using the liquid vapor phase change as the heat transfer mechanism. The heat pipe consists of a copper absorber tube covered with a selective coating, which is made of black chrome. The heat pipe is composed of two

sections: the evaporator and the condenser (the adiabatic section is neglected). The reflective mirror of the PTC concentrates the beam radiation into the receiver tube. The concentrated flux received at the evaporation zone evaporates the working fluid (Thermex) in the heat pipe. The natural pressure difference drives the vapor to the condenser, where it is cooled and condensed, due to the external flow of the synthetic oil (Therminol VP-1) in the steel tube. The capillary structure on the inner wall ensures the return of the liquid from the condenser to the evaporator. The steel tube is wrapped in a thermal insulation material. The wick structure is made of sintered metal powder (Copper).

Thermex was chosen as the heat pipe's working fluid for its stability at our operating temperature range [115]. The Therminol VP-1 synthetic oil is chosen as the heat transfer fluid in the tube collector for its stability at high temperatures [116].

A properly designed wick structure will ensure the continuous availability of sufficient liquid in the evaporator of the heat pipe to maximize the heat transfer.

A properly designed wick structure will ensure the continuous availability of sufficient liquid in the evaporator of the heat pipe to maximize the heat transfer.

3.2.1 Steady – state modelling

3.2.1.1 Hypothesis

The following assumptions were made to write the formulation of the mathematical models:

- The temperature of the reflector equals ambient temperature
- The heat flux is uniform along the evaporator zone of the heat pipe.
- The temperature is uniform along the evaporator zone.
- The temperature is uniform along the condenser zone.
- The optical errors, such as shading, cleanliness of the mirror are not considered in our model.
- The system is operating in steady state conditions.
- The optical properties are taken at a normal incident angle**.**

3.2.2 The modelling of the system

The model of the studied system is based on a representation of heat transfer by global thermal resistances as illustrated in Figure 3.2.

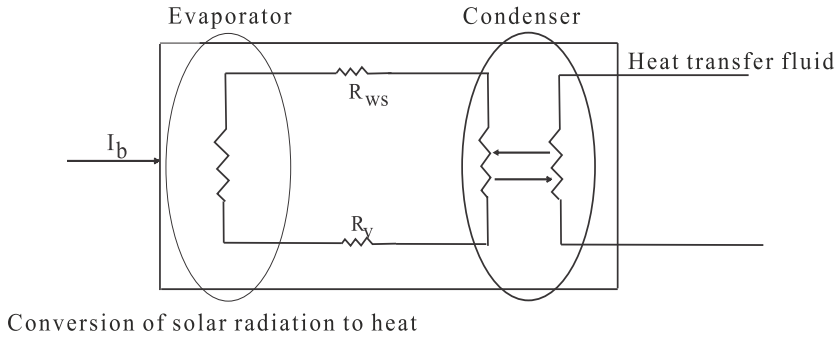

Figure 3.2. Electrical diagram of the whole system

A more detailed electrical analogy of the system is given in figure 3.2.

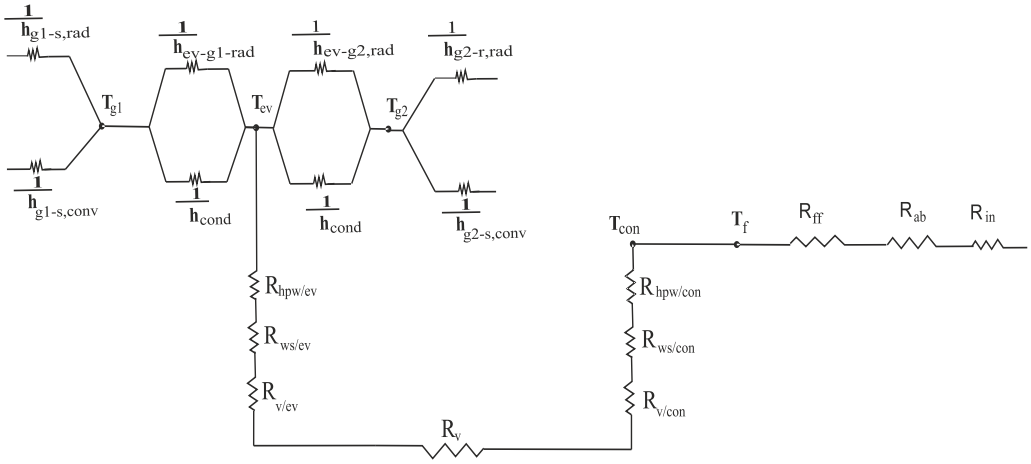

Figure 3.3. Schematic representation of different thermal resistances of the system

3.2.2.1 **Heat transfer between the receiver and the environment**

The heat exchange between the glass cover and the surroundings occurs through convection and radiation (Figure 3.4).

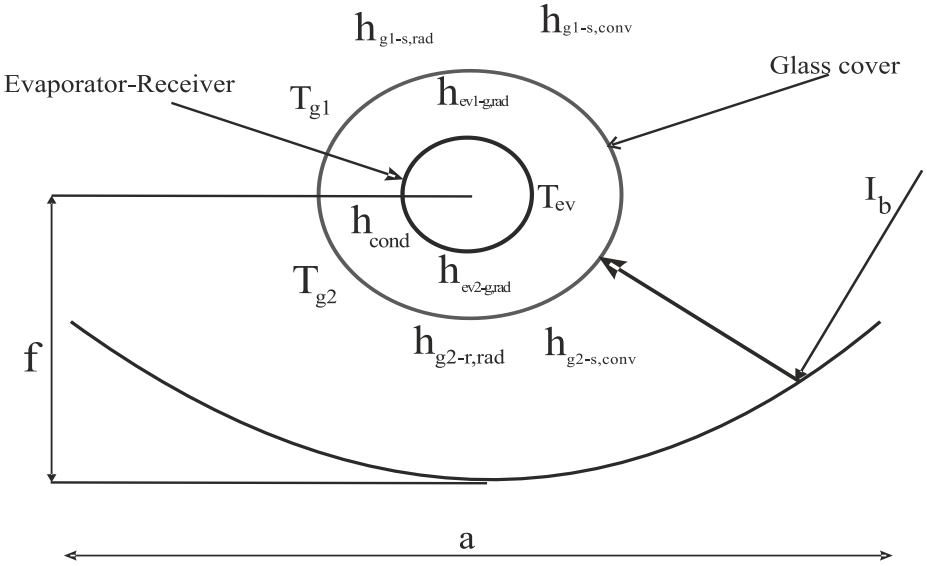

Figure 3.4. Heat transfer for the heat pipe coupled with a PTC.

The convective heat transfer coefficient $h_{g1\text{-}s,conv}$ around the upper part of the glass envelope can be estimated by [117] :

$$h_w = 1.32\left[\frac{T_v - T_a}{D}\right]^{1/4} \qquad \text{For } Re < 400 \tag{3.1}$$

$$h_w = \left(0.0161\ \mathbf{Re}^{0.492} + 0.007\right)\left(1/D\right) \qquad \text{For } Re > 400 \tag{3.2}$$

Where:

$$\mathbf{Re} = 72770\ D\ V \tag{3.3}$$

V is the wind speed (m/s)

Assuming that the sky is a black body, the radiative heat transfer coefficient between the upper part of the glass envelope and the sky can be written as[10]:

$$h_{g1-s,rad} = \varepsilon_g\ \sigma\left(\frac{T^4_{g1} - T^4_s}{T_{g1} - T_a}\right) \tag{3.4}$$

Where T_{g1} is the temperature of the upper part of the glass cover

The heat loss coefficient between the upper part of the glass envelop to the environment is finally given by:

$$U_{11} = (h_{g1-s,rad} + h_{g1-s,conv}) \tag{3.5}$$

Due to the high conductivity of the evaporator wall (Copper) and the high temperature of the vapor inside the evaporator we can assume that the temperature of the upper part and the lower part of the evaporator are equal.

The conduction heat transfer between the evaporator wall and the glass cover is given by Raithby and Holland's correlation [118], that is:

$$h_{cond} = \frac{2k_{air}}{D_{hp(ext)}} \ln\left(\frac{D_{g(int)}}{D_{hp(ext)}}\right) \tag{3.6}$$

The radiative heat transfer coefficient between the evaporator wall and the upper part of the glass tube [119] is written as:

$$h_{ev-g1,rad} = \frac{\sigma(T^2_{ev} + T^2_{g1})(T_{ev} + T_{g1})}{\frac{1}{\varepsilon_{hp}} + \frac{D_{hp}}{D_{gi}}\left(\frac{1}{\varepsilon_g} - 1\right)} \tag{3.7}$$

The heat loss coefficient between the evaporator and the upper part of the glass envelop is as follows:

$$U_{12}= (h_{ev-g1,rad}+h_{ev-g,cond}) \quad (3.8)$$

The heat loss coefficient between the evaporator and the environment facing the upper part of the glass cover is given by:

$$U_{up}=\left[\frac{1}{U_{11}}+\frac{1}{U_{12}}\right]^{-1} \quad (3.9)$$

The heat transfer coefficient between the lower part of the glass cover and the reflector is given by:

$$h_{g2-rad}=\frac{\left(T_{g2}^4-T_r^4\right)\left(T_{g2}-T_a\right)^{-1}}{\frac{1-\varepsilon_g}{A_g\,\varepsilon_g}+\frac{1}{A_gF_r}+\frac{1-\varepsilon_r}{A_c\varepsilon_r}} \quad (3.10)$$

The heat loss coefficient between the lower part of the glass envelop to the environment is finally given by:

$$U_{21}=\left(h_{g2-r,rad}+h_{g2-s,conv}\right) \quad (3.11)$$

The radiative heat transfer coefficient between the evaporator wall and the glass tube [119] is written as:

$$h_{ev-g2,rad}=\frac{\sigma(T_{ev}^2+T_{g2}^2)\left(T_{ev}+T_{g2}\right)}{\frac{1}{\varepsilon_{hp}}+\frac{D_{hp}}{D_{gi}}\left(\frac{1}{\varepsilon_g}-1\right)} \quad (3.12)$$

The heat loss coefficient between the lower part of the evaporator and the glass envelop is as follows:

$$U_{22}= (h_{ev-g,rad}+h_{cond}) \quad (3.13)$$

The heat loss coefficient between the upper part of the evaporator and the environment is given by:

$$U_L=\left[\frac{1}{U_{21}}+\frac{1}{U_{22}}\right]^{-1} \quad (3.14)$$

The global heat transfer losses from the evaporator wall to the environment and given by:

$$U_G=\frac{(U_U+U_L)}{2} \quad (3.15)$$

The effective sky temperature is estimated by [120]:

$$T_s = 0.0552\ T_a^{1.5} \tag{3.16}$$

The ambient temperature was estimated by using the following model [121]:

$$Ta(t)=\frac{Ta_{max}+Ta_{min}}{2}+\frac{Ta_{max}-Ta_{min}}{2}\cos\left(\frac{\pi\,(14-ST)}{12}\right) \tag{3.17}$$

3.2.3 **The heat pipe model**

The thermal resistances of the heat pipe can be summarized as follows [115] , and their expressions were given in Table 1:

Table 3-1. Thermal resistances of the heat pipe.

Thermal resistances					
$R_{hpw/ev}$	$R_{ws/ev}$	$R_{v/ev}$	$R_{ws\text{-}con}$	$R_{hpw/con}$	$R_{v/con}$
$\frac{\log(\frac{r_w}{r_v})}{2\,\pi L_e k_p}$	$\frac{\log(\frac{r_w}{r_v})}{2\,\pi L_e k_w}$	$\frac{1}{A_{ev}\,h_{v/ev}}$	$\frac{\log(\frac{r_w}{r_v})}{2\,\pi L_c k_{eff}}$	$\frac{log(\frac{r_w}{r_v})}{2\,\pi L_c k_p}$	$\frac{1}{A_{ev}h_{v/ev}}$

With:

$R_{hpw/ev}$, $R_{hpw/con}$ Thermal resistances of the evaporator's and condenser's walls.

$R_{ws/ev}$, $R_{ws/con}$ The thermal resistance of the evaporator's and condenser's wick structures.

$R_{v/ev}$, $R_{v/con}$ Thermal resistances of Thermex vapor in the evaporator and condenser section.

Notice that the resistance of vapor (R_v) in both the evaporator and the condenser is neglected due to the low conductivity of the working fluid in the vapor state. The effective thermal conductivity for liquid-saturated wick structures is evaluated by[122]:

$$k_{eff} = \varepsilon\, k_l + (1-\varepsilon) k_{ws} \tag{3.18}$$

3.2.3.1 **Heat transfer between heat pipe and synthetic oil**

Figure 3.1. represents the heat pipe-tube collector connection

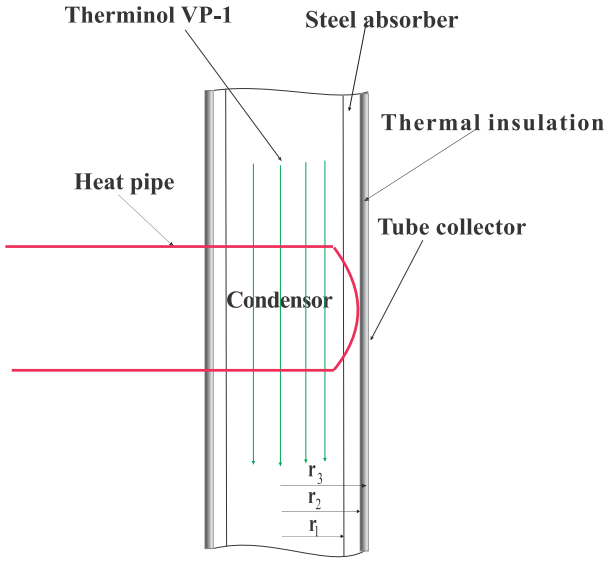

Figure 3.5. Schematic representation of heat pipe-conduit connection

The thermal resistances presented in table 3.2 are illustrated in figure 3.3.

Table 3-2. The thermal resistance of the condenser inserted to the tube collector.

$R_{ff} = \frac{1}{A_1 h_{loss}}$	The thermal resistance of fluid
$R_{ab} = \frac{r_2 \log(\frac{D_2}{D_1})}{A_2 k_{ab}}$	The thermal resistance of the absorber (Steel)
$R_{in} = \frac{r_2 \log(\frac{D_3}{D_2})}{A_3 k_{is}}$	The thermal resistance of the thermal insulation

The Nusselt number used to calculate the heat transfer coefficient h_f for the heat transfer fluid flow across the condenser is calculated using the following correlation, [123] as:

$$Nu_m = (0.4\ Re^{0.5} + 0.06\ Re^{2/3})\ Pr^{0.4} \left(\frac{\mu_\infty}{\mu_w}\right)^{0.25} \quad (3.19)$$

The Nusselt Number used to calculate the convective heat loss coefficient inside a tube collector is given by the correlation of Colburn, as [124]:

$$Nu = 0.023\ Re^{0.8} Pr^{1/3} \tag{3.20}$$

3.2.4 Efficiency estimation

3.2.4.1 Useful energy

The energy absorbed (Q_{ab}), on the evaporator wall is given by:

$$Q_{ab} = A_c \eta_0 K(\theta) I_b \cos(\theta) \tag{3.21}$$

The direct solar radiation (I_b) was estimated using R-Sun model [28].

The heat flux received by the Therminol VP-1 is given by:

$$Q_i = A_c \left(\frac{R_{evw-e}}{R_{f-e}}\right) (Q_{ab} - U_{loss} (T_f - T_a)) \tag{3.22}$$

Where:

R_{evw-e}: Thermal resistance between the heat pipe wall and the environment.

R_{f-e}: Thermal resistance between the heat transfer fluid and the environment

The solar incident angle (θ) for the East-West horizontal alignment is given by [32]:

$$\cos(\theta_i) = \sqrt{1 - cos^2\delta\ sin^2\omega} \tag{3.23}$$

The solar incident angle (θ) for the inclined North-South alignment is given by equation (3.24 and 3.25) and the details are given in the appendices.

In the morning:

$$\cos(\theta_i) = cos(h)\ cos(a)\sin(\beta) + \cos(h)\sin(a)\ \sin(ş)\cos(\beta) + \\ + \sin(h)\cos(ş)\cos(\beta) \tag{3.24}$$

In the afternoon:

$$\cos(\theta_i) = cos(h)\ cos(a)\sin(\beta) - \cos(h)\sin(a)\ \sin(ş)\cos(\beta) + \\ + \sin(h)\cos(ş)\cos(\beta) \tag{3.25}$$

Figure 3.6 represent the positioning of the receiver and the aperture of the PTC in case of inclined setting:

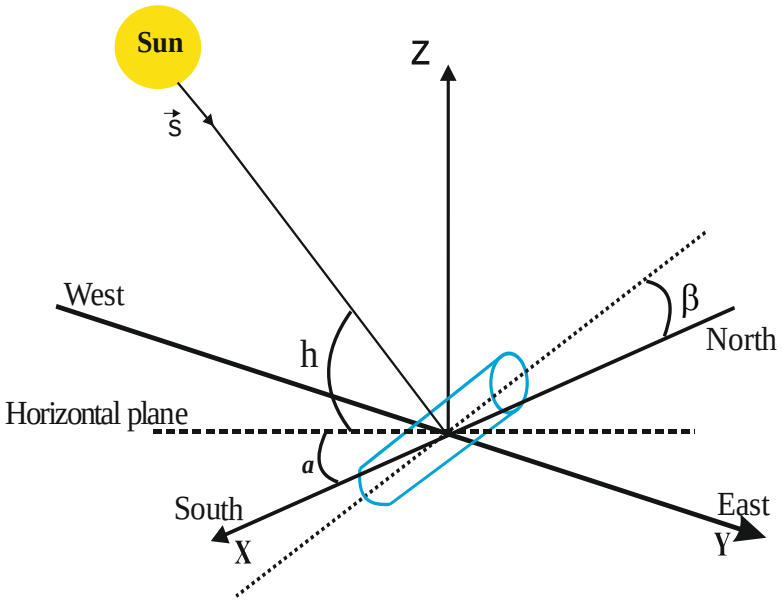

Figure 3.6. Schematic representation of the receiver in case of inclined PTC.

3.2.4.2 **Thermal efficiency**

The useful heat gain (Q_u) by the condenser is given by:

$$Q_u = \dot{m} C_{pf} \Delta T_f = Q_i - U_{con} A_{con} (T_f - T_a) \quad (3.26)$$

From which :

$$\frac{Q_i}{\dot{m} C_{pf}} = \Delta T_f + \frac{A_{con} U_{con}}{\dot{m} C_{pf}} (T_f - T_a) \quad (3.27)$$

Assuming that:

$$T_f = T_i + \frac{\Delta T_f}{2} \quad (3.28)$$

And using equation (3.28), the previous equation can be written:

$$\frac{\Delta T_f}{2} = \frac{Q_{ab}}{U_{loss}} - (T_i - T_a) - \frac{Q_i}{A_c F' U_{loss}} \quad (3.29)$$

Combining equation 3.26 and 3.29 we obtain:

$$\frac{Q_i}{\dot{m} C_{pf}} \frac{1}{2 + \frac{A_{con} U_{con}}{\dot{m} C_{pf}}} = \frac{A_{con} U_{con}}{\dot{m} C_{pf}} \frac{1}{2 + \frac{A_{con} U_{con}}{\dot{m} C_{pf}}} (Ti - Ta) + \frac{\Delta T_f}{2} \quad (3.30)$$

Replacing $\frac{\Delta T_f}{2}$ with its formula from equation (3.27), we obtain:

$$Q_i\left[\frac{1}{(A_c F' U_{loss})+1/(2\,\dot{m}C_{pf}+A_2 U_{con})}\right]=\frac{1}{(A_c F' U_{ev})}+\frac{1}{2\,\dot{m}C_{pf}+A_2 U_{con}} \quad 3.31)$$

Or:

$$Q_i=\frac{\frac{G}{U_{loss}}-\left[1-\frac{A_{con}U_{con}}{A_{con}U_{con}+2\,\dot{m}C_{pf}}\right](Ti-Ta)}{\frac{1}{A_c F' U_{loss}}+\frac{1}{2\,\dot{m}C_{pf}+A_{con}U_{con}}} \quad (3.32)$$

The overall thermal efficiency of the system is given by:

$$\eta_{th}=\frac{Q_u}{Q_s} \quad (3.33)$$

Where solar power irradiance in the aperture area of the collector Q_s can be calculated as:

$$Q_s = A_c I_b \quad (3.34)$$

3.3 Transient state modelling of the system

3.3.1 Hypothesis

To solve of the mathematical models, the following assumptions were made:

A- The thermo-physical properties of the glass envelope and the heat pipe wall are constant.

B- The thermal inertia of the heat pipe's working fluid is negligible.

C- The temperature is uniform along the solid components of the system (Low Biot number).

The transient behavior of the system is based on the following formulas:

$$Q_u = Q_i - Q_{loss} + \sum\left(mc_p\frac{dT}{dt}\right)_i \quad (3.35)$$

Where:

Q_i Is the incident power on the system.

Q_u Is the useful heat gain.

$\sum\left(mc_p\frac{dT}{dt}\right)_i$ The inertia of the whole system.

The thermal inertia of the system is the sum of the thermal inertia of all the components of the system:

$$\sum \left(mc_p \frac{dT}{dt}\right)_i = \left(mc_p \frac{dT}{dt}\right)_{Glass\ cover} + \left(mc_p \frac{dT}{dt}\right)_{Evaporator\ wall} + \left(mc_p \frac{dT}{dt}\right)_{Condenser\ wall} + \left(mc_p \frac{dT}{dt}\right)_{Th\ VP1} \quad (3.36)$$

Where:

$\left(mc_p \frac{dT}{dt}\right)_{Glass\ cover}$: Is the thermal inertia of the class cover

$\left(mc_p \frac{dT}{dt}\right)_{Evaporator\ wall}$: Is the thermal inertia of the evaporator wall

$\left(mc_p \frac{dT}{dt}\right)_{Condenser\ wall}$: Is the thermal inertia of the condenser wall

$\left(mc_p \frac{dT}{dt}\right)_{Th\ VP1}$: Is the thermal inertia of the HTF (Therminol VP-1)

3.3.1.1 **Energy balance on the glass cover**

The energy balance equation for the glass cover is described as follows:

$$\left(\rho V C_p\right)_g \frac{dT_g}{dt} = Q_{abs,g} + \left(Q_{hpw-g,rad} + Q_{hpw-g,cond}\right) - \left(Q_{loss,rad} + Q_{loss,conv}\right) \quad (3.37)$$

Where:

$\rho V C_p$: Density, volume and heat capacity respectively.

$Q_{hpw-g,rad}$: Radiation heat transfer between the evaporator wall glass cover.

$Q_{hpw-g,cond}$: Conduction heat transfer between the evaporator wall and the glass cover.

$Q_{loss,rad}$: Radiation heat transfer between the glass cover and the sky.

$Q_{loss,conv}$: Convection heat transfer due to wind between the glass and the sky.

The energy absorbed on the glass envelope is given by:

$$Q_{abs,g} = I_b\ A_c\ \alpha_g\ \rho_0\ \gamma \quad (3.38)$$

Where:

I_b: Beam radiation in W/m^2

Ac: The surface of the trough collector.

α_g: Absorptance of the glass cover.

ρ_0 : Reflectivity of the mirror.

γ : Intercept factor.

3.3.1.2 Energy balance on the evaporator wall

The energy balance equation for the evaporator is described as follows:

$$(\rho V C_p)_{evw} \frac{dT_{evw}}{dt} = Q_{ab} - (Q_{evw-g,cond} + Q_{evw-g,rad}) - \frac{1}{R_{ev-con}}(T_{ev} - T_{cw}) \quad (3.39)$$

Where:

Q_{ab}: The energy absorbed by the evaporator

T_{ev}: Temperature of the evaporator wall

T_{cw}: Temperature of the condenser wall

$R_{ev,con}$: Represents all the thermal resistances between the evaporator and the working fluid.

$$R_{ev-con} = R_{evw} + R_{v\text{-}ev} + R_{v\text{-}c} + R_{wc\text{-}ev} + R_{ws\text{-}c} + R_{cnw} \quad (3.40)$$

Where:

R_{evw}: Thermal resistance of the evaporator wall.

$R_{v\text{-}ev}$: Thermal resistance of vapor in the evaporation zone.

$R_{v\text{-}c}$: Thermal resistance of vapor in the condensation zone.

$R_{wc\text{-}ev}$: Thermal resistance of the wick structure in evaporation zone.

$R_{ws\text{-}c}$: Thermal resistance of the wick structure in condensation zone.

R_{cnw}: Thermal resistance of the condenser wall.

Figure 3.7. represents the thermal resistances between the evaporator and the heat transfer fluid.

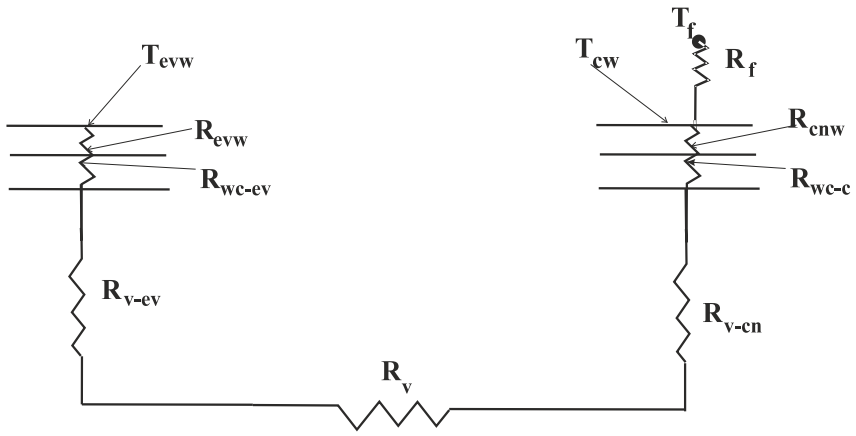

Figure 3.7. Thermal resistances between the evaporator and the heat transfer fluid.

Where:

R_v: The thermal resistance of vapor.

The energy absorbed on the heat pipe wall is given by:

$$Q_{ab} = \eta_0 \, I_b \; A_c \tag{3.41}$$

3.3.1.3 Energy balance on the condenser wall

The energy balance equation on the condenser wall is described as follows:

$$(\rho V C_p)_{cw,} \frac{dT_{cw}}{dt} = \frac{1}{R_{ev-con}} (T_{evw} - T_{cw}) - A_{tc} \, h_f \left(T_{cw} - T_f\right) \tag{3.42}$$

Where:

T_f: Temperature of the heat transfer fluid (HTF)

A_{tc}: Surface of the tube collector

h_f: Heat transfer coefficient of the HTF

3.3.1.4 **Energy balance on the heat transfer (Therminol VP-1)**

The collectors are mounted in parallel, one element of the fluid is taken.

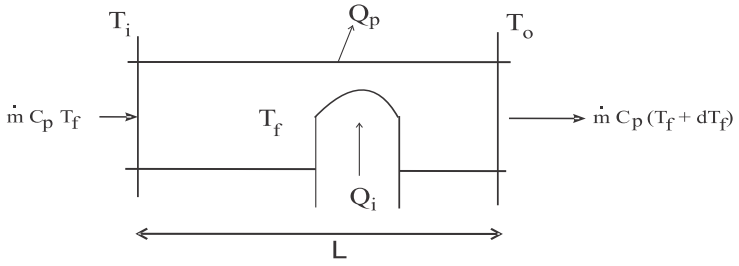

Figure 3.8. Energy balance on the working fluid

Where:

T_i: The inlet temperature of the HTF.

T_O: The inlet temperature of the HTF.

Balance on the considered fluid volume:

$$M_f\, C_p\, \frac{dTf}{dt} = Q_i + \dot{m}\, C_{pf}\, T_i - (\dot{m}.\, C_p(T_i + \Delta T) + Q_p) \tag{3.43}$$

Where:

M_f: The mass of the heat transfer fluid (HTF)

C_{pf}: Heat capacity of heat transfer fluid

$\dot{m}$: The mass flow rate of the HTF

The heat loss is given by:

$$Q_p = A_{tc}\, U_p.\, (T_f - Ta) \tag{3.44}$$

Where:

Ta : Ambient temperature

U_p: Heat loss coefficient

Heat flux received by the Therminol VP-1 is given by:

$$Q_i = A_{con}\, .\, h_f.\, (T_{con} - T_f) \tag{3.45}$$

The energy balance equation on the heat transfer fluid is described as follows:

$$\frac{dTf}{dt} = \frac{Q_i - Q_p - \dot{m}\, \Delta T\, C_p}{M_f C_{pf}} \tag{3.46}$$

3.3.1.5 **The system of equation to solve**

The system of coupled differential equations was solved using the second order Rung Kutta method, and it's given by:

$$\frac{dT_g}{dt} \frac{\alpha_g \gamma \rho_s \mathrm{K}(\theta)\, \mathrm{I_b} + \left(h_{evw-g,conv} + h_{\mathrm{evw-g,rad}}\right)\left(T_{evw} - T_g\right)A_{ev} - \left(h_{g-s,conv} + h_{\mathrm{g-s,rad}}\right)\left(T_g - T_{sky}\right)A_g}{\left(\rho V \mathrm{C_p}\right)_{\mathrm{g}}} \tag{3.47}$$

$$\frac{dT_{evw}}{dt} = \frac{\eta_0 \mathrm{K}(\theta)\, \mathrm{Ib} - \left(h_{evw-g,conv} + h_{\mathrm{evw-g,rad}}\right)\left(T_{hpw} - T_g\right)A_{ev} + \frac{1}{R_{tot,hp}}\left(T_{cw} - T_{evw}\right)}{\left(\rho V C_p\right)_{hpw}} \tag{3.48}$$

$$\frac{dT_{con}}{dt} = \frac{\frac{1}{R_{ev-con}}\left(T_{evw} - T_{cw}\right) - A_{con} h_f \left(T_{cw} - T_f\right)}{\left(\rho V C p\right)_{cw}} \tag{3.49}$$

$$\frac{\partial T_f}{\partial t} = \frac{\mathrm{A}_{con}\,.\mathrm{h_f}.(\mathrm{Tcon} - \mathrm{Tf}) - \mathrm{A_{tc}\ Up}.\left(\mathrm{T}_f - \mathrm{Ta}\right) - \dot{m}\ \Delta T\ \mathrm{C_{pf}}}{M_f\ \mathrm{C_{pf}}} \tag{3.50}$$

3.4 Conclusion

In this study, a theoretical model was developed to study in both steady and transient state performances of a Heat-Pipe receiver integrated into a parabolic trough collector. A network of thermal resistances was created to facilitate the study of the thermal performance of the system. The present model allows conducting a detailed heat transfer analysis of the system. The equations describing the steady and transient state behavior of the system were established. The developed model allows the variation of the thermo-physical properties of Thermex and the Therminol VP-1 with temperature. The steady state model is validated with experimental data and good agreement was found.

4. CHAPTER 04: RESULTS AND DISCUSSION

4.1 Introduction

The annual and daily optical efficiency were calculated for both East-West and North-South alignment. The effect of the absorptance of the cylindrical absorber on the daily optical efficiency was investigated. The end loss ratio was calculated for both trough alignments for three different representative days. In addition, the effect of end loss on optical efficiency was investigated.

The steady state and transient state behavior of a heat pipe coupled with a parabolic trough collector was studied, a detailed heat transfer analysis of the system was presented. The thermophysical properties of the heat transfer fluid (Therminol VP-1) in the tube collector and the working fluid (Thermex) in its both liquid and vapor states in the heat pipe vary with temperature, the derived polynomial and exponential expressions for these properties with variable temperatures were presented, some were developed and other from the literature. The theoretical results were compared with experimental results provided by the literature[106].

4.2 The results obtained from the optical analysis

The values of the parameters used to perform the calculation are shown in Table

Table 4-1: Parameter used to perform the calculation.

Parameters	Values
The refractive index	n=1.526
Extinction coefficient of the glass cover	k=16 m^{-1}
External diameter of the glass cover	D=125mm
External diameter of absorber	D_{ab}=70mm
Glass cover thickness	e=3mm
Absorptivity of the selective coating at a normal incidence angle	$\alpha_{p0} = 0.95$
Aperture width of collector	a= 5.77m
The length of the receiver	L=12 m
The focal length	f= 1.75 m
The reflectivity of mirror	ρ_n= 0.94
The intercept factor	γ=0.96

4.2.1 The optical efficiency of the parabolic trough for both East-West and North-South alignment

In order to get a more accurate optical efficiency we took into consideration the fact that the receiver tube is not only irradiated by the reflected radiation from the mirror but also by the radiation reaching the receiver directly, so that the whole receiver surface is irradiated.

The optical efficiency depends on the average transmittance. However, when the average transmittance is low, the energy absorbed decreases and therefore the optical efficiency also decreases. On the other hand, the optical efficiency depends also on the angle of incidence which is the angle that the ray makes with a line perpendicular to the reflective surface, large incidence angles causes higher end losses which have the effect of reducing the geometric conversion coefficient and hence the optical efficiency also decreases. Figure 4.1 represents the optical efficiency in function of time for both East-West and North-South alignment. In the case of N-S alignment, the receiver has a higher optical efficiency especially in the early morning and late afternoon due to low end loss effect, and this differs from the case of E-W alignment as the receiver is facing the sun during mid-day and therefore lower end loss and higher optical efficiency.

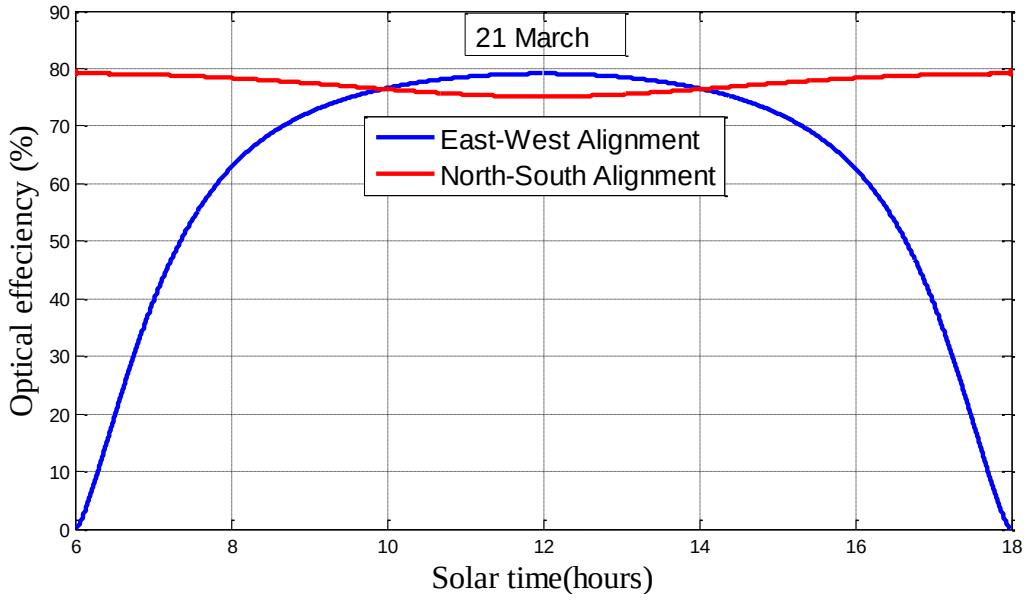

Figure 4.1. The optical efficiency of the receiver

4.2.2 **Daily variation of and loss for both East-West and North-South alignment**

Single-axis tracking PTC have end loss due to the cosine effect, the non-illuminated length (E) of the receiver depends on the focal length (f) and the incidence angle. Large incidence angles θ (greater than zero) imply greater losses at the end of the collector. The reflected radiation on the ends of the mirror misses the receiver tube.

Figure 4.2 represents end losses (M) for the North-South alignment in the function of Hour angle, we can observe that end loss is high in Winter Solstice 25.51% followed by Summer Solstice 10.90 % and low in Spring and Autumn equinoxes 3.44 %, these values are obtained at mid-day. We can also notice that the end loss ratio is higher at noon, in the mornings and

evenings the sun is due East or West and the PTC is pointed towards the sun, this will allow the collector to receive full Sun and hence low end loss.

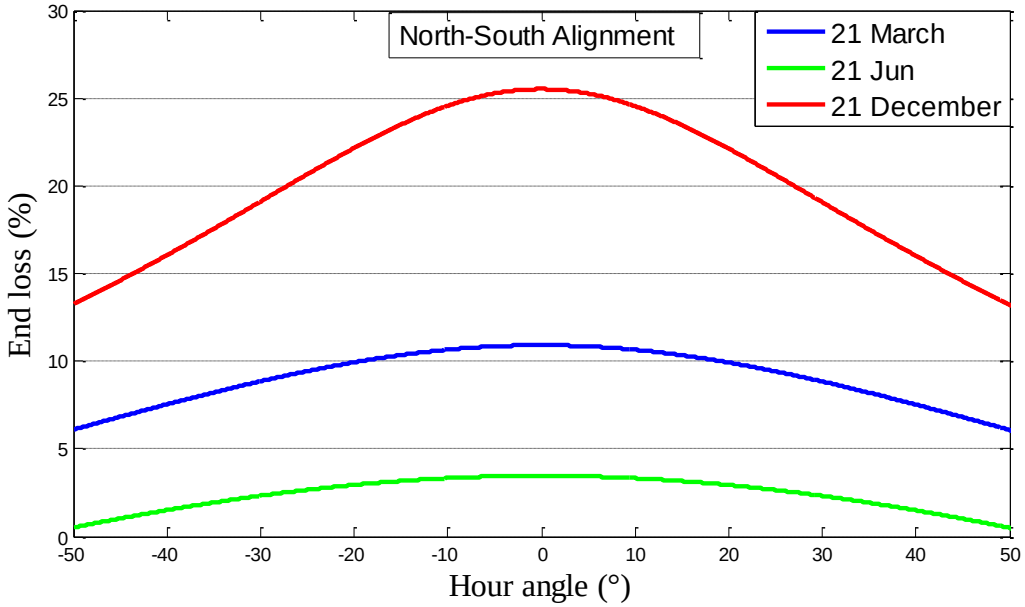

Figure 4.2: Daily variations of end losses in the case of North-South alignment

Figure 4.3 represents the daily variation of end loss in the function of azimuth angle, we can see that for East-West alignment end loss ratio is higher in Spring and Autumn equinoxes 20.37% followed by Summer Solstice 12% and minimum end loss in Winter Solstice 4% for the azimuth of -60° and +60°. We can also notice that the end loss ratio is higher at the beginning and end of the day and null at noon, this is because the East-West oriented collectors are pointed to the zenith position of the Sun at noon.

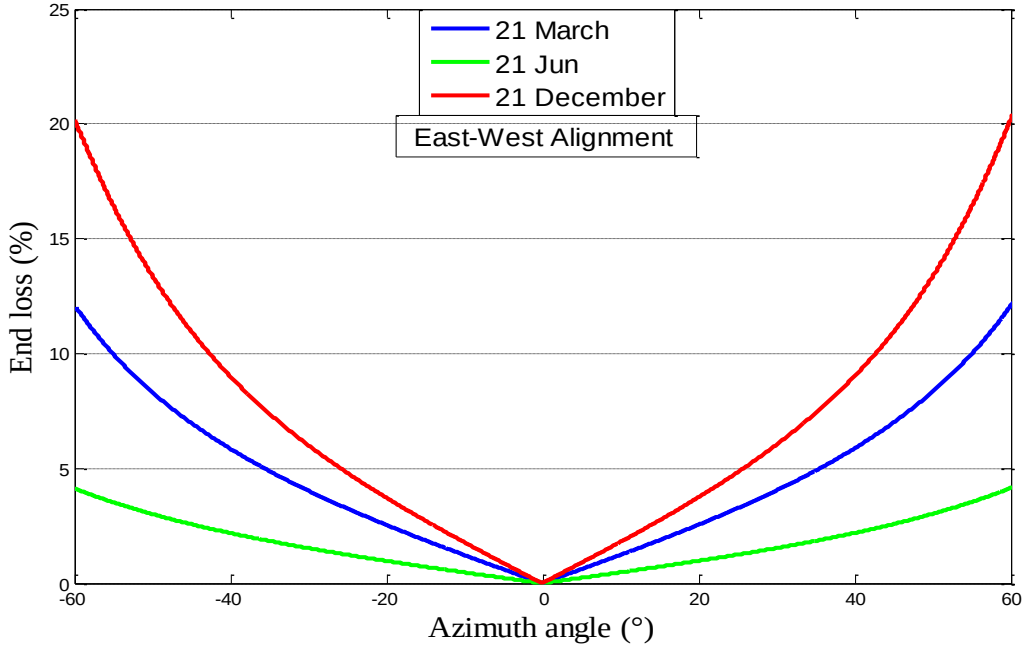

Figure 4.3: Daily variations of end losses in the case of North-South alignment

4.2.3 Effect of end loss on the optical efficiency

Single-axis tracking PTC has end losses, to minimize these losses we can use a relatively long PTC. In a parabolic trough power plant, the PCTs are mounted in series but the end loss still exist and affect the performance of the plant. Figure 4.4 illustrates the effect of end loss on the optical efficiency of the parabolic trough collector in the function of end loss in the case of North-South alignment and for both equinoxes. We can see that the optical efficiency has a linear variation starting from its highest value when end losses are null to its lowest value when and end losses are high. We notice that end loss has a great effect on the optical efficiency, where only 10% end loss results in around 11% drop in the optical efficiency, this can be explained by the fact that when the collector is not facing the Sun (nonzero incidence angle) end losses occur at the ends of the heat collection element HCEs, a part of the absorber tube length is not illuminated by reflected solar radiation from the mirrors. The equation representation of the curve can be expressed as follows:

$$\eta_0 = -1.20M + 79 \tag{3.60}$$

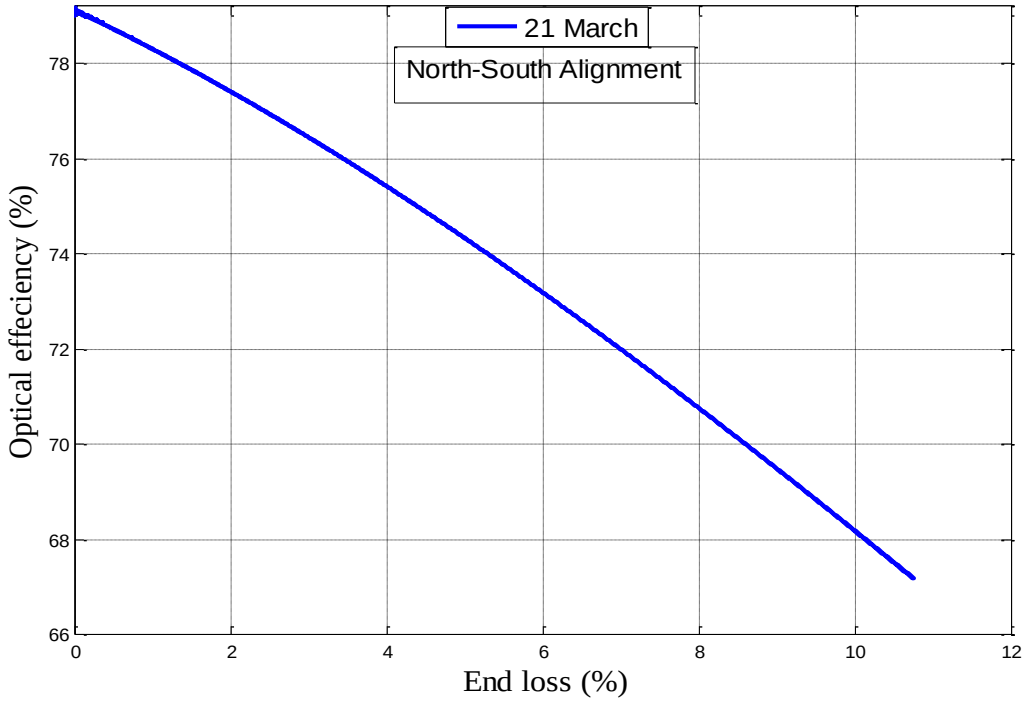

Figure 4.4. The influence of the end loss on optical efficiency

4.2.4 Effects of varying the absorptance of absorber on the optical efficiency

The optical efficiency depends on the absorptance of the material because it is used to calculate the effective absorptance-transmittance product. To study the influence of the

absorptance of the materials on the optical efficiency, three materials where chosen (see table 4.2).

Table 4-2: Absorptance of some Selective Surfaces.

Surface	**Absorptance (α_p)**	**Emissivity (ε)**
Black crome on Ni-plated steel [125]	0.95	0.09
Ebanol C on Cu; commercial Cu-blackening treatment giving coating largely CuO [126]	0.90	0.16
"Nickel black" on galvanized steel [126]	0.81	0.17

The Heat collection element (HCE) consists of a steel absorber tube coated with selective coating; the surface coating can be made from different materials. As seen in figure 4.5, the optical efficiency of the receiver depends on the absorptance of the selective surface, and the optimum optical efficiency is achieved when absorbance fraction of the selective coating is high and solar emissivity is low, which is because materials with high absorptance and low emissivity can absorb more solar radiation and hence high optical efficiency is achieved.

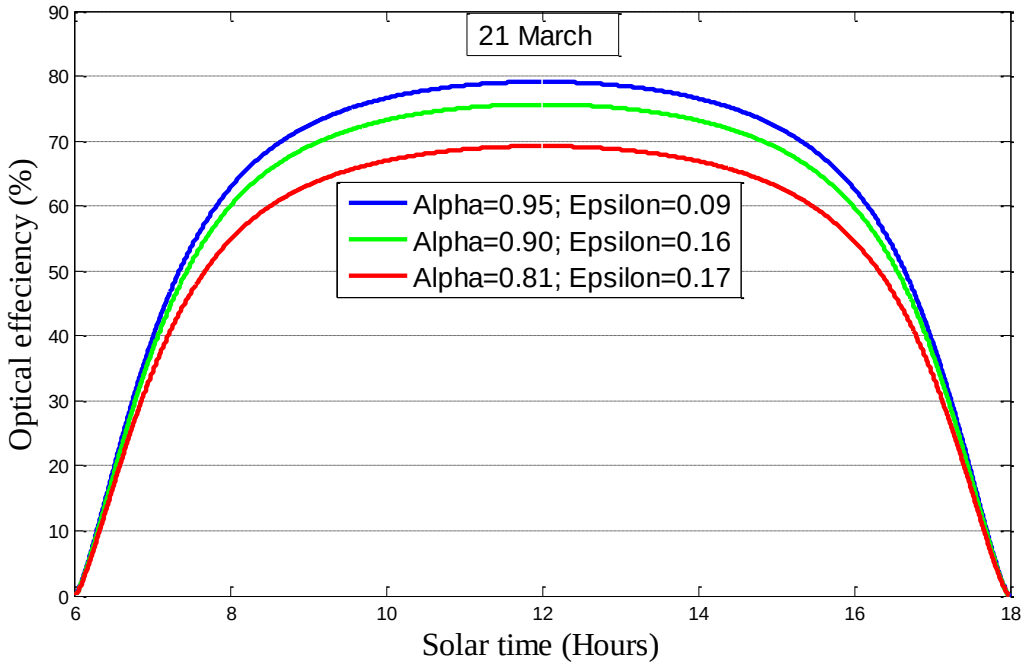

Figure 4.5. Optical efficiency for different selective surfaces.

4.2.5 The annual optical efficiency of both trough East-West and North-South alignment

Figure 4.6 represents the yearly optical efficiency of the parabolic trough collector. Overall, the North-South alignment has higher optical efficiency than East-West alignment. In case of North-South alignment solar radiation has a significant effect on the optical efficiency, a great number of solar ray's results in high optical efficiency of the PTC system which is obvious in summer, and a small number of solar rays results in low optical as can be observed in winter. The East-West alignment has higher optical efficiency in winter because unlike north-south alignment, incidence angles on the collector are smaller in winter compared to summer. The differences in the optical efficiency are due to the different incident angles and the corresponding end loss.

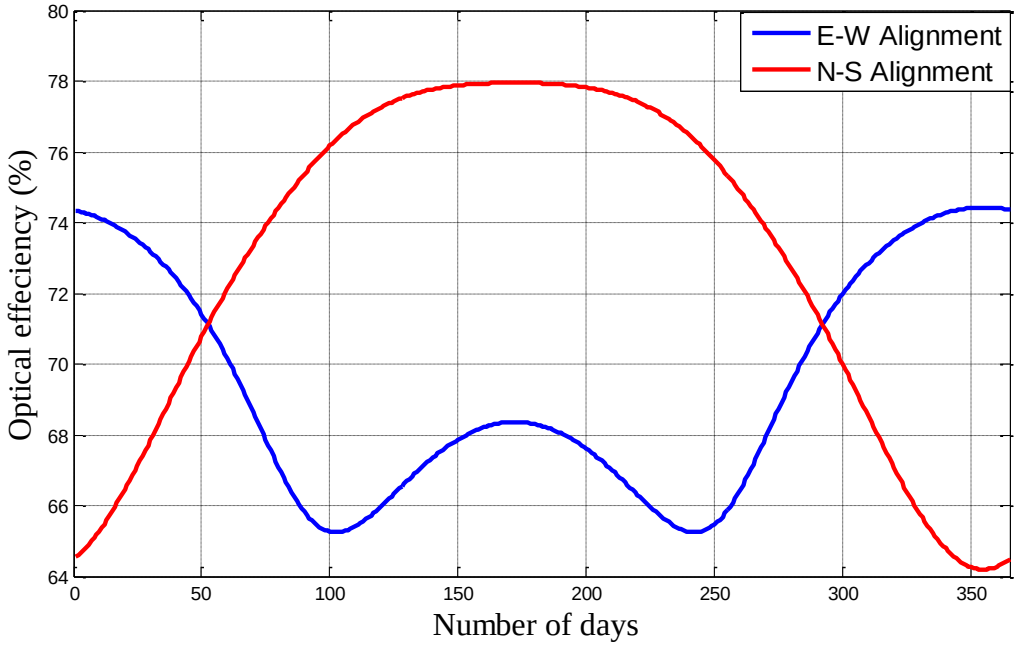

Figure 4.6. The efficiency is dependent on the time of year.

4.2.6 The results and discussions from the thermal modelling

4.2.6.1 Results obtained in the case steady state

The simulation was performed with ambient temperature and beam radiation kept constant, the ambient temperature is 25°C and the beam radiation was calculated at mid-day using R-Sun model (refer to section 6).

Table 4-3. Characteristics of different components of the system.

The latitude of the location	36°8	Condenser length	0.2 m
The longitude of the location	3°12’	Internal diameter of the heat Pipe	0.066 m
The altitude	345 m	Absorptance of the selective coating	0.95
Maximal temperature retrieved from	18 °C	External diameter of the heat pipe	0.07 m
Maximal temperature retrieved from	8°C	Emissivity of the heat pipe absorber	0.06
Wind speed	3 m/s	Thickness of the heat pipe wall	10 mm
External diameter of the glass cover	0.115 m	Thickness of the wick structure	5 mm
Internal diameter of the glass cover	0.109 m	Heat pipe wall thermal Conductivity (Copper)	380 W/m. K
Intercept factor	0.96	Tube collector’s thermal insulation	5 cm
Angle of incidence modifier	1	Wick porosity	0.6
Aperture width of the collector	5.67 m	Air conductivity	0.026 W/m. K
Reflectance of the reflector	0.93	Gas constant	8.31 J/mol. K
Transmittance of the glass cover	0.90	Conductivity of the tube collector’s absorber (Steel)	47 W/m. K
Emissivity of the glass cover	0.935	Therminol VP1 mass flow rate	0.03 kg/s.m^2
Evaporator length	15 m	Conductivity of the thermal insulation (Polyurethane)	0.028 W/m. K
		The envelope absorptance (α_g)	0.023

4.2.7 Validation of the model

Due to the lack of the experimental results provided by the literature on the topic, the obtained results were compared with experimental results of Ismail et al. [106] [127] despite the differences between our cases of study. To have a reasonable comparison, the beam radiation, the collector’s characteristic and the heat pipe’s working fluid (Water) of the experimental setup were used in the validation program.

To assess the accuracy of our theoretical model Root Mean Square Error (RMSE) was calculated using the following formulas:

$$RMSE = \frac{\sqrt{\sum_{t=1}^{N}(\eta_t - \eta_{ex})^2}}{N} \quad (4.1)$$

Where is η_t are the theoretical values at time t and η_{ex} are the experimental values at time t and N is the number values. Figure 4.7 represents the hourly predicted efficiency compared with the experimental data provided by the literature. The obtained results were compared with the experimental data provided by the literature, having RMSE=0.0166. The difference between the current model and the experimental data is explained by the fact that in the current model, the tracking system is assumed to be perfect while a manual adjustment of the PTC was adopted in the experiment, furthermore the intercept factor is function of end losses and geometrical imperfections so it can influence the heat flux intercepted by the absorber.

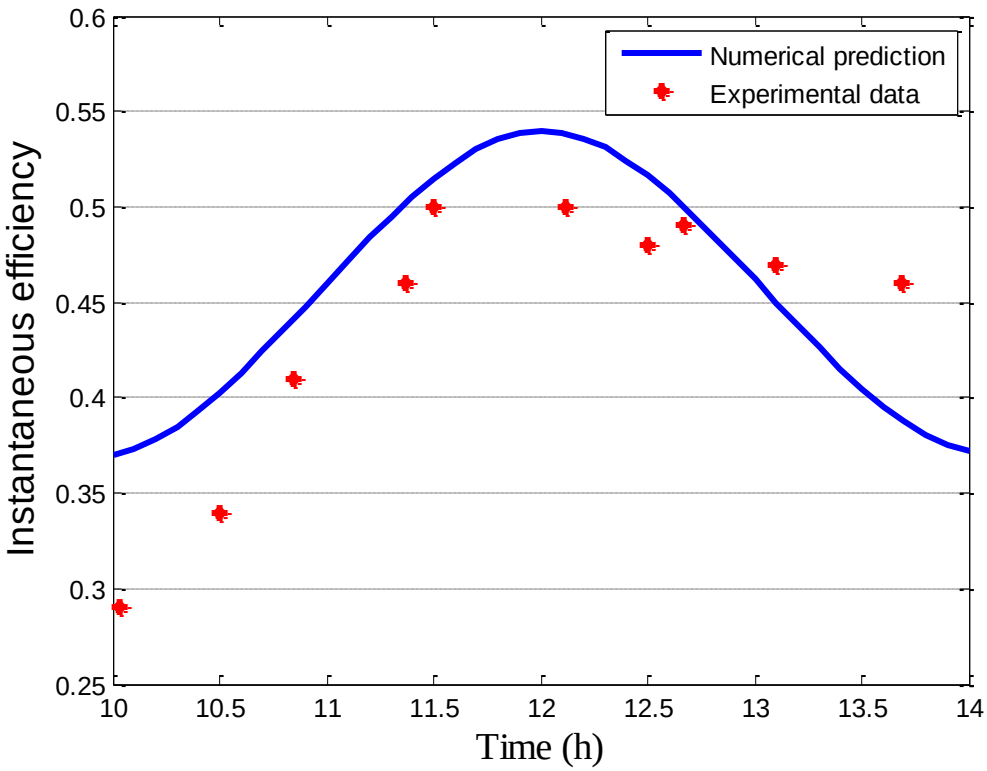

Figure 4.7. Comparison between Instantaneous efficiency of the current model and the experimental data

The heat loss plays an important role in the collector's performance; minimizing heat losses occurring at the PTC receiver can boost the efficiency of the collector. Heat pipes have several advantages compared to other receiver tubes in terms of high heat conduction and efficient heat transfer. Heat pipes also have the ability to dissipate and transfer large amount of energy without significant heat loss. Figure 4.8 represents the evolution of heat losses of the current system and the heat loss measured in the parabolic-trough collector named UrssaTrough with PTR-70 receivers. The UrssaTrough was manufactured by the Spanish company URSSA Energy Corporation, it is installed in the HTF-PTC test facility at the Plataforma Solar de Almería (Spain). PTR70 receiver tubes were manufactured by the German company Schott[128] .

Firstly, maximum heat loss measured in the UrssaTrough collector with PTR-70 receivers is 294.22 W/m.

The model representing the variation of heat loss [129]:

$$Q_p = 0.342.\Delta T + 1.16310^{-8}.\Delta T^4 \quad (4.2)$$

The maximum heat loss are obtained for the current system is 157.36 W/m.

The adjustment model representing the variation of heat loss was developed using the least-squares method:

$$Q_p = 0.33.\Delta T + 3.24.10^{-9}.\Delta T^4 \quad (4.2)$$

Where ΔT presents (Tf-Ta) for both models.

Less heat losses are obtained for the current system compared to an ordinary receiver.

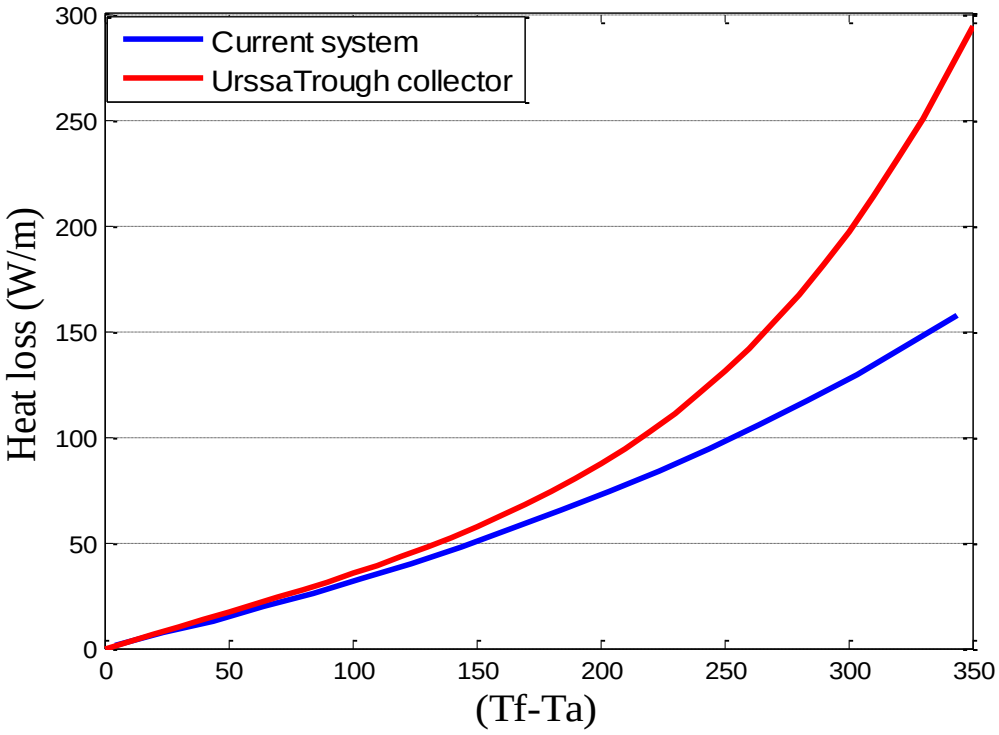

Figure 4.8. The heat losses of the system collector versus ΔT

The heat pipes operating system is based on the thermal heat transfer by the phase transition of the working fluid (latent heat), making it possible to have a particularly interesting efficiency in the transportation of heat and limitation of heat losses. Figure 4.9 shows the efficiency of the system compared with UrssaTrough collector efficiency. It is clearly observed that the overall efficiency is higher than UrssaTrough in the operating temperature range due to the low thermal resistance and the high heat removal rate of the heat pipe.

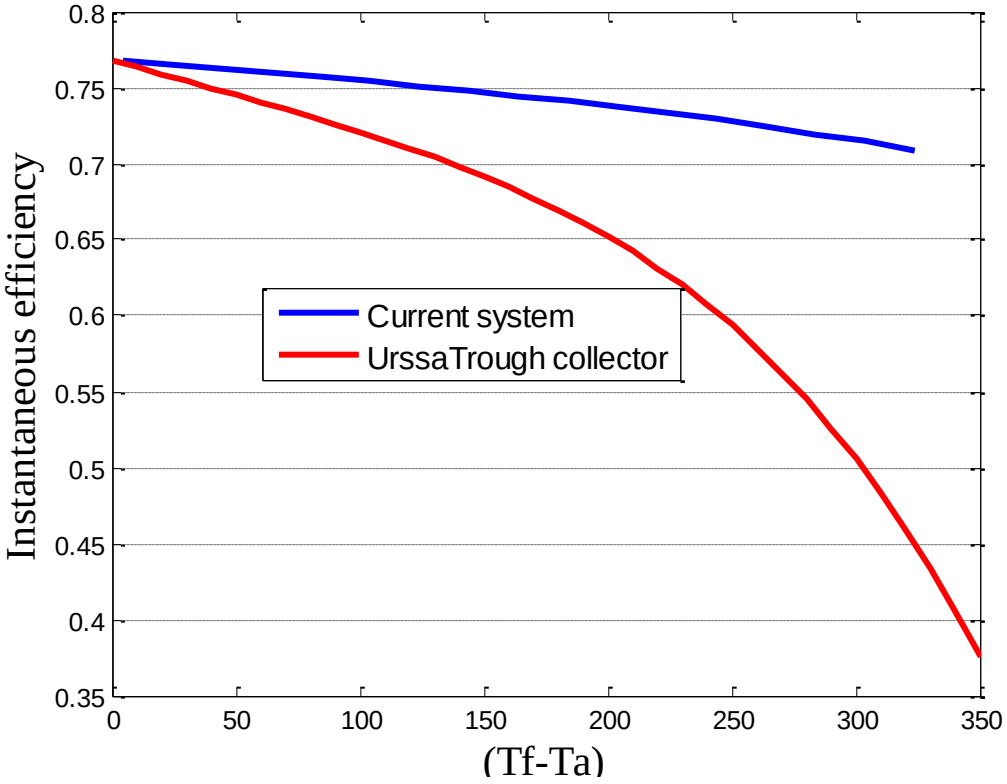

Figure 4.9. The instantaneous efficiency of the system collector as versus ΔT

Figure 4.10 depicts the evolution of the efficiency with the beam radiation, the PTC is oriented to North-South direction. We notice that the efficiency rises with the augmentation of the beam radiation. This is because when the amount of solar energy collected by the reflector increases, the solar radiation absorbed by the heat pipe becomes higher, therefore more useful heat gain reaches the collector tube. Furthermore, due to the augmentation of vapor generation from the evaporator to the condenser, only thin layer of the liquid on the pipe wall remains causing low thermal resistance. This increases the heat transfer rate of the heat pipe's working fluid and the heat transfer fluid thereby increasing the efficiency of the system.

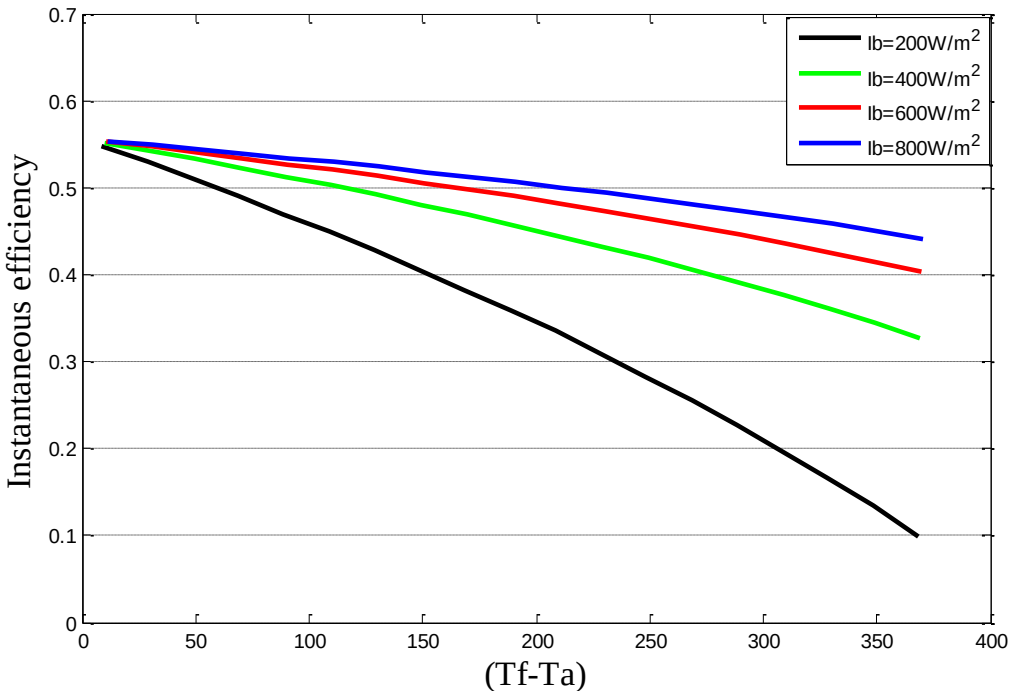

Figure 4.10. The instantaneous efficiency of the system collector versus ΔT

Inclining the pipe to an angle from the horizontal affects its performance due to the gravity effect. The evaporator has to be below the condenser to assist the capillary structure bring the condensate to return to the evaporator to continue the cycle. Figure 4.11 shows the overall efficiency of an inclined PTC compared to a horizontal configuration oriented to North-South direction. The inclined setting helps to maximize the received annual solar radiation and therefore improve the thermal performance of the system. It also depends on the incidence angle which is the angle that the solar ray makes with the line perpendicular to the reflective surface. The inclined setting has smaller incidence angles and therefore less end losses and hence the overall efficiency is increased.

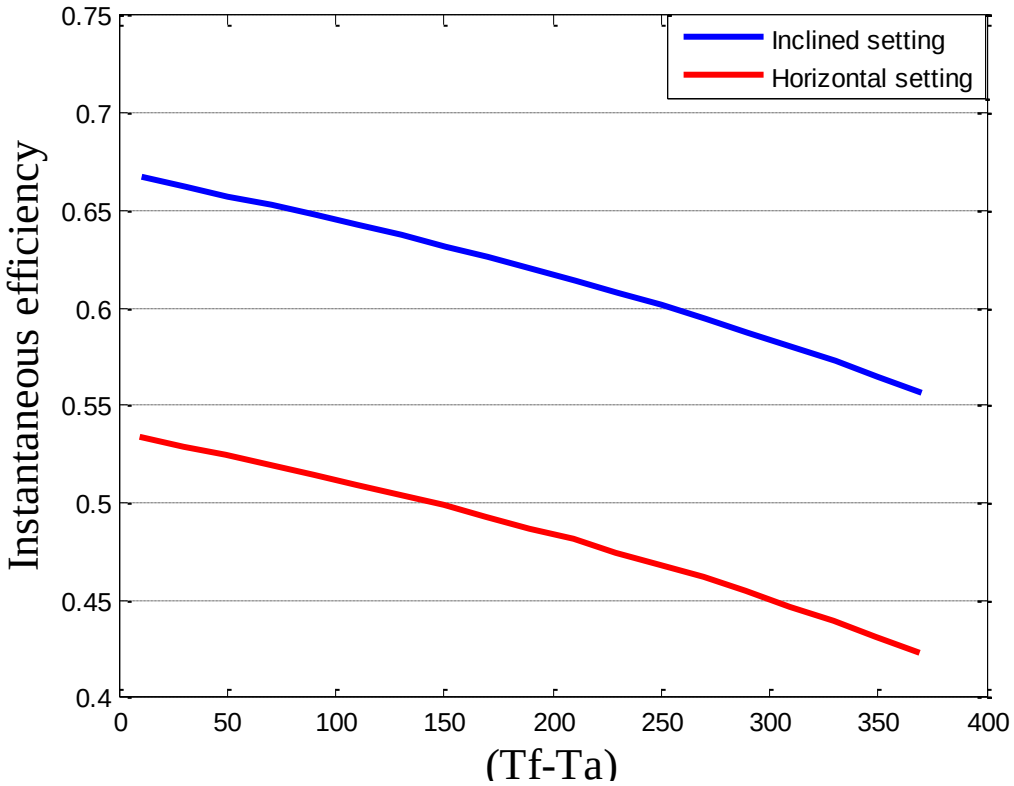

Figure 4.11. Comparison between the horizontal and inclined setting

4.2.8 **Results obtained in the case of transient state**

Table 4-4: Parameter used to perform the calculation in transient state [130][131]

Parameters	**Values**
Absorptivity of the glass cover normal incidence angle	$\alpha_{p0} = 0.023$
Heat pipe specific heat	Cp_{hp}=381.1 J/kg K
Heat pipe density	ρ_{hp} = 8954 kg/m^3
Glass envelop specific heat	Cp_g=1090 J/kg K
Glass envelop density	ρ_g 2230 kg/m^3
Mass flow rate	m=0.3. A_c

The ambient temperature, beam radiation and the optical efficiency vary with time.

Before presenting the results, two input variables namely the ambient temperature and the beam radiation are analysed.

4.2.8.1 **Scenario 1: Cold start up**

The initial temperature of the glass envelope, heat pipe wall, condenser wall, and heat transfer fluid HTF; $T_g(x, 0)$, $T_{evw}(x, 0)$, $T_{cnw}(x, 0)$, and $T_f(x, 0)$ are considered equal to the ambient temperature. The following are the initial conditions:

$T_g(x, t=0)=T_a$ $T_{cnw}(x, t=0)=T_a$ $T_{evw}(x, t=0)= T_a$ $T_f(x, t=0) = T_a$

Figure 4.12. shows the variation of the outlet temperatures of the fluid, evaporator, condenser and glass cover. The ambient temperature in function of time [121] (see equation 3.15) and the beam radiation (I_b) which is calculated using R-Sun model[28], are represented in the same figure. We notice that the evaporator's temperature is the highest followed by the temperature of the condenser and then the heat transfer fluid and the glass cover has the lowest temperature.

The increase in the solar heat flux causes an increase of the glass envelope's temperature; the increase in the glass envelope temperature produces a large external heat loss**.** The transient state behavior of the evaporator wall's and the condenser wall temperature are considered, this implies that transient temperature behavior of the heat pipe mainly depends on the wall and wick heat conduction. Although the working fluid has small thermal resistance, it does affect the heat pipe operation in another important way by maintaining a wetted evaporator surface so as to continue the heat transfer process. The figure shows that the gradient of temperature increases with heat input and shows larger temperature differences in case of the evaporator, condenser and heat transfer fluid. When the evaporator is heated, the working fluid is evaporated as it absorbs an amount of heat equivalent to its latent heat of vaporization. In the condenser section, the working fluid vapor is condensed by the heat transfer fluid circulating in the tube absorber. The variation of heat transfer fluid temperature along the absorber tube causes a rise in the condenser's temperature because of the heat transferred from evaporator to condenser by evaporation and condensation at the liquid vapor interface. The enthalpy of the heat transfer fluid (HTF) changes with time due to the fluid particles changing positions and the useful heat input to fluid terms. The latent heat transported from the evaporator and to the condenser causes the temperature of the heat transfer fluid to increase. We notice that even after the Sun sent (Absence of solar radiation), the system continues to work due to the thermal inertia of the system especially the HTF.

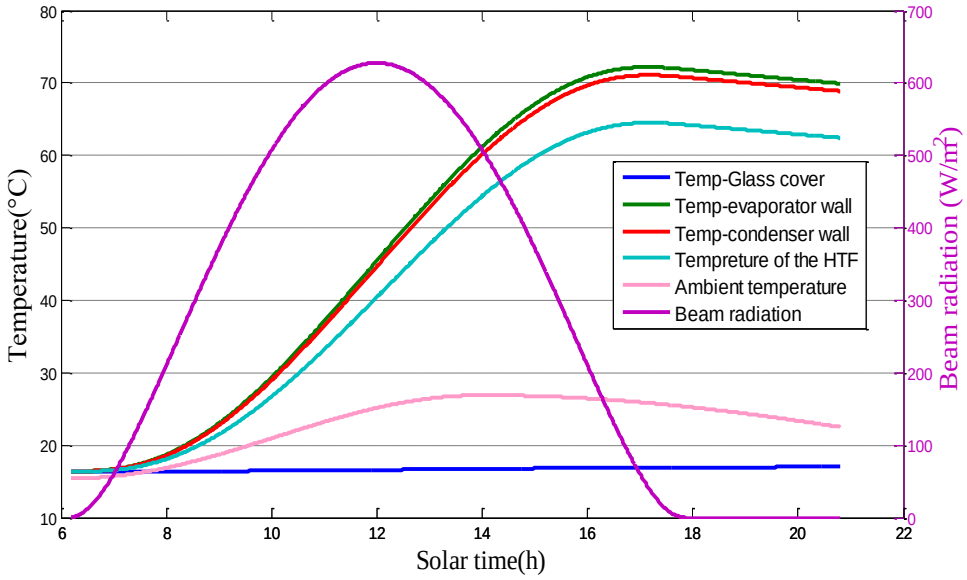

Figure 4.12. Variation of the temperatures and beam radiation in the case of cold start-up

Figure 2.13. represents the variation of the HTF temperature during a day (We have chosen summer solstice "June 21" to represent summer and winter solstice "December 21" to represent winter, both equinoxes were represented in one graph because the declination angle equals zero in both equinoxes "March 21and September 21"). The HTF temperature is high summer solstice followed by both equinoxes and then the winter solstice this is due to the high solar intensity during summer days compared to other seasons.

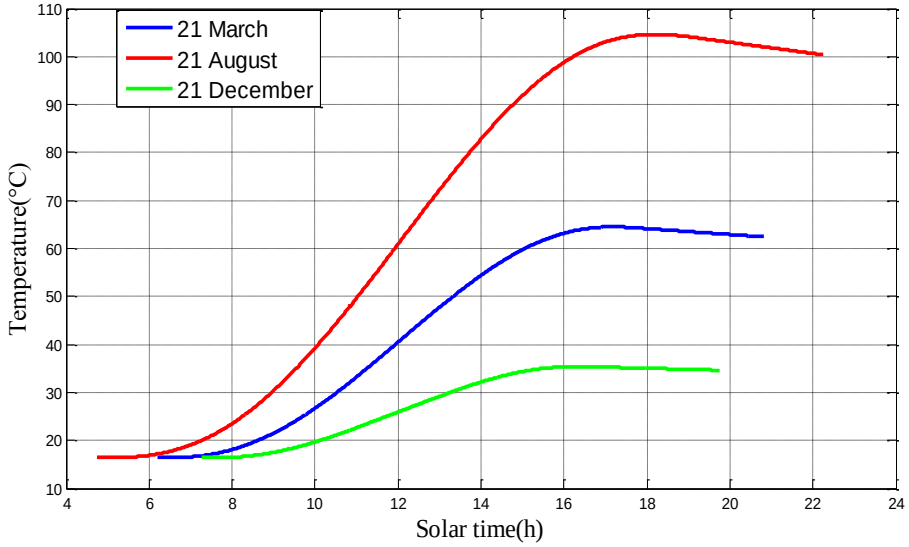

Figure 4.13. The variation of the HTF temperature during a day

Figure 4.14. depicts the variation in the HTF's outlet temperatures with mass flow rate. It is shown that the HTF temperature varies as a function of the mass flow rate, with the temperature increasing as the latter decreases.

The mass flow rate of the fluid is an important parameter causing the variation of the outlet temperature, we have seen from the figure that water outlet temperature reaches a value of 68 ° C for a flow rate of 0.01 kg / s.m^2.

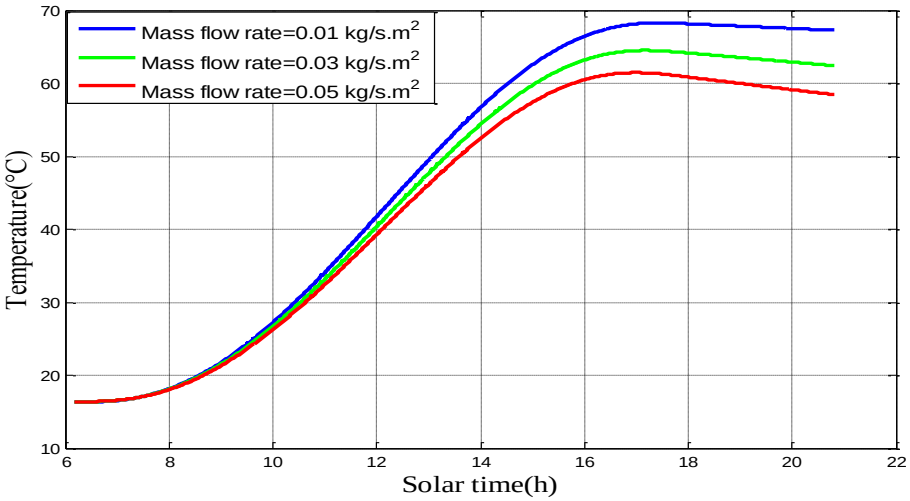

Figure 4.14. Variation in the HTF's outlet temperatures with mass flow rate

4.2.8.2 **Scenario 2: System under operation (Hot start up)**

The initial temperature of the glass envelope, heat pipe wall, condenser wall, and heat transfer fluid HTF; T_g (x, 0), T_{evw}(x, 0), T_{cnw}(x, 0), and T_f (x, 0) are considered equal to the operating temperature. The following are the initial conditions:

T_g (x, t=0) =19.25 °C; T_{con}(x, t=0) = 177.4 °C ; T_{ev} (x, t=0) = 178.91 °C;

$T_f(x, t = 0)$= 172.59 °.

Figure 4.15. represents the variation of the temperatures in case hot start-up. After the sun disappears there is no thermal gains due to the absence of lightning because of the absence of solar radiation but the system continues to work due to high thermal inertia of the system. To reach higher temperature we need a series of collectors.

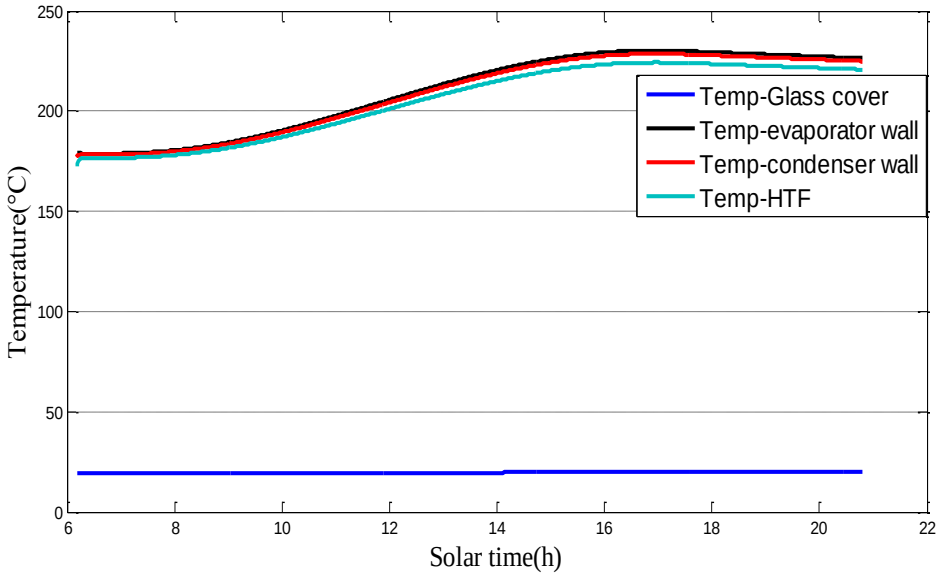

Figure 4.15. Variation of the temperatures and beam radiation in the case of hot start-up

4.3 Conclusion

The ray-tracing method was used to calculate the optical efficiency of the parabolic trough collector, the method is based on tracing the solar ray until it reaches the cylindrical absorber. The average solar transmittance of the upper part of the receiver (the part facing the sky) was calculated for different incident angles using a numerical integration technique. The transmittance of the lower part of the receiver was also calculated for different longitudinal angles taking into account the end losses. The effective absorptance -transmittance product was calculated for different incidence angles and the optical efficiency of the receiver was calculated for three representative days and the whole year. The proposed model is very efficient as it allows to calculate the optical efficiency with lower computing cost, and shorter runtime. The model also demonstrated its capability to accurately study the effect of different geometrical and optical parameters on optical efficiency. The model takes into consideration multiple reflections of solar rays between the glass cover and the absorber cylinder before their absorption. The model takes also into account the incident angle variation, end effects, and both trough alignments. Even though the lower part of the receiver has a higher transmittance because it receives concentrated solar rays with small incidence angle, the transmittance of upper semi-cylindrical part of the receiver was calculated because it receives solar rays coming directly from the Sun. By calculating the effective absorptance transmittance product absorptance $(\tau\alpha)_{eff}$ for different incident angles, better accuracy in the optical efficiency will be achieved. The results showed that the optical efficiency depends on the absorptance of the material and the trough alignment. The results also showed that end losses have a great effect on the optical efficiency.

The coupling of a PTC with a heat pipe allows to achieve higher temperatures than those achieved with an ordinary receiver and therefore the efficiency of the system. This configuration offers the possibility to the parabolic trough collectors to be mounted in parallel and arranged horizontally or inclined. In this study, a theoretical model was developed to study the performance of a heat pipe receiver integrated into a parabolic trough collector. A network of thermal resistances was created to facilitate the study of the thermal behavior of the system. The present model allows conducting comprehensive heat transfer investigation of the system. The equations describing the steady state behavior of the system were established. The developed model allows the variation of the thermo-physical properties of Thermex and Therminol VP-1 synthetic oil with temperature. The influence of some important parameters on the performance of the system was studied. The results

showed that the inclined setting improves the efficiency of the system. The system performs at high efficiency thanks to the high thermal performance of the heat pipe. The model was validated using experimental results obtained from the literature. The proposed system, the coupling of the heat pipe with PTC leads to 33 % increase of the efficiency of the system and a significant reduction in the heat losses by 46.55%. The inclined arrangement setting increased the efficiency of the system by 13 %. These values were obtained at the maximum ΔT.

Finally, the model was validated by comparing the numerical results with experimental data obtained from the literature. The results showed a good agreement with experimental data.

Transient analysis of a heat pipe absorber integrated to a parabolic trough collector were performed, energy balances were applied in each component of the system. The ambient temperature, beam radiation and the optical efficiency vary with time. The system of partial differential equations describing the unsteady-state behavior of the system was established and solved using the Runge-Kutta method on MATLAB.

GENERAL CONCLUSION

The solar energy potential of Algeria is considered as very enormous, the measure being related to the surface of the country and the number hours of Sunshine (more than 3000 hours/year). Characteristics which arouse a great national and international interest for the installation of concentrated solar systems called CSP. Among the solutions, the vacuum tube solar collectors with linear concentrators, offer good prospects**.**

The coupling of a parabolic trough concentrator with a heat pipe can improve the performance of PTC because it allows:

1- To reach higher temperatures than those encountered with an ordinary tube concentrator.

2- To reduce the complexity of the system.

3- Increase the power delivered by the turbine.

This thesis aims to determine in steady and transient state the theoretical performances of a heat pipe integrated to a parabolic trough solar collector.

We started the thesis by giving a detailed overview of the geometric aspects of solar radiation including coordinate systems and the measurement of solar radiation. We provided also a review on concentrating collectors; the review focused on the parabolic trough technology including parabolic trough collector geometry, the performance of parabolic trough collector, the different components of parabolic trough collector and a literature review on the technology.

A detailed review of the heat pipe was provided, starting from a brief history of the technology. The review included also the types of the heat pipe (Heat-Pipe, thermosiphon), the type of heat transfer fluid, and the limits of heat pipe…. etc.

All the equations used for the modelling of the optical performances of the PTC receiver have been presented. The goal of the optical analysis was to determine the incident flux on the glass cover and then the absorber accordingly.

The thermal study of the heat pipe integrated into a parabolic trough collector was presented in detail. We studied the thermal exchanges Absorber-Ambient, Absorber-Working fluid and then heat transfer through the heat pipe. We have estimated the efficiency of the solar concentrator in steady and transient state.

The validation of the model with literature and the results obtained from the optical and thermal modeling in addition to the parametric study were presented.

The optical model developed calculates the transmittance and the effective transmittance-absorptance product $(\tau\alpha)_{eff}$ for different incidence angles, this leads to a higher precision in the optical efficiency. The methodology proposed in this paper calculates $(\tau\alpha)_{eff}$ value for all incident angles and hence improves the method.

The steady state model of allows analyzing heat transfer processes in the heat pipe integrated to a parabolic trough solar collector, and estimate the efficiency of the system.

The model results were validated through experimental data provided by the literature.

The transient model was developed to investigate transient thermal behavior of coupled to a parabolic trough solar collector focusing on the influence of inlet temperature heat transfer fluid on the performance of the system. The results shows that the use of heat pipe as a receive for parabolic trough collector results in increasing the efficiency.

Perspectives:

For the continuation of this work, it would be advisable to:

- Take into account the optical errors, such as shading, cleanliness of the mirror.
- Validate the model with our own experimental results
- It is highly recommended that the economic feasibility of the heat pipe integrated to parabolic trough collector, the system should be evaluated for different applications.

5. APPENDIX

5.1 Estimation of the incidence angle

The incidence angle at a parabolic trough changes continuously throughout the day, table 6.1 summarizes the different tracking modes with corresponding incident angles.

Table 5-1: Incident angles for each tracking mode[32]

Tracking mode	Cosθ
Full tracking	Cosθ=1
E-W polar	Cosθ= Cos δ
E-W horizontal	Cosθ=$\sqrt{(cos\delta\ sin\varphi\ cos\omega - cos\delta\ cos\omega)^2}$
N-S horizontal	Cosθ=$\sqrt{1-cos^2}\delta sin^2\varphi$

5.1.1 The incident solar angle calculation in case of inclined North-South alignment:

The unit vector of the solar ray is given by:

$$\vec{s}\begin{cases} cos(h)\,cos(a) \\ cos(h)\,sin(a) \\ sin(h) \end{cases} \quad (5.1)$$

The unit vector perpendicular to the optical axis is given by:

In the morning: $\overrightarrow{n_2}\begin{cases} 0 \\ cos\,ş \\ -sin\,ş \end{cases}$ (5.2)

In the afternoon: $\overrightarrow{n_2}\begin{cases} 0 \\ cos\,ş \\ sin\,ş \end{cases}$ (5.3)

The tracking can be considered as perfect if the vector $\overrightarrow{n_2}$ and the unit vector of the solar ray are perpendicular which means that $\vec{s}\,.\overrightarrow{n_2}$= 0.

In the morning:

$$\vec{s}\,.\overrightarrow{n_2} = cos(h)\,sin(a)\,cos(ş) - sin(h)\,sin(ş) = 0 \quad (5.4)$$

In the afternoon:

$$\vec{s}\,.\overrightarrow{n_2} = cos(h)\,sin(a)\,cos(ş) + sin(h)\,sin(ş) = 0 \quad (5.5)$$

The tracking angle (s) which equal to the zenith angle is given by:

$$s = arctan\left((-1)^n \frac{sin\,a}{tan\,h}\right) \quad (5.6)$$

n= 1 before mid-day and n=2 after mid-day.

The unit vector of the optical axis $\vec{n}$ is given by:

In the morning:

$$\overrightarrow{n_1}\begin{cases} \sin(\beta) \\ +sin(ş)\cos(\beta) \\ cos(ş)\cos(\beta) \end{cases} \tag{5.7}$$

And

In after noon:

$$\overrightarrow{n_1}\begin{cases} \sin(\beta) \\ -sin(ş)\cos(\beta) \\ cos(ş)\cos(\beta) \end{cases} \tag{5.8}$$

The angle between the sunray and the optical axis given by:

In the morning:

$$\cos(\theta) = \overrightarrow{n_1}.\vec{s} = cos(h)\,cos(a)\sin(\beta) + \cos(h)\sin(a)\sin(ş)\cos(\beta) + \\ +\sin(h)\cos(ş)\cos(\beta) \tag{5.9}$$

In the afternoon:

$$\cos(\theta) = \overrightarrow{n_1}.\vec{s} = cos(h)\,cos(a)\sin(\beta) - \cos(h)\sin(a)\sin(ş)\cos(\beta) + \\ +\sin(h)\cos(ş)\cos(\beta) \tag{5.10}$$

1. Optical analysis in of a plate absorber

Figure 5.1 represents the optical path of the solar ray until it reaches the plate absorber.

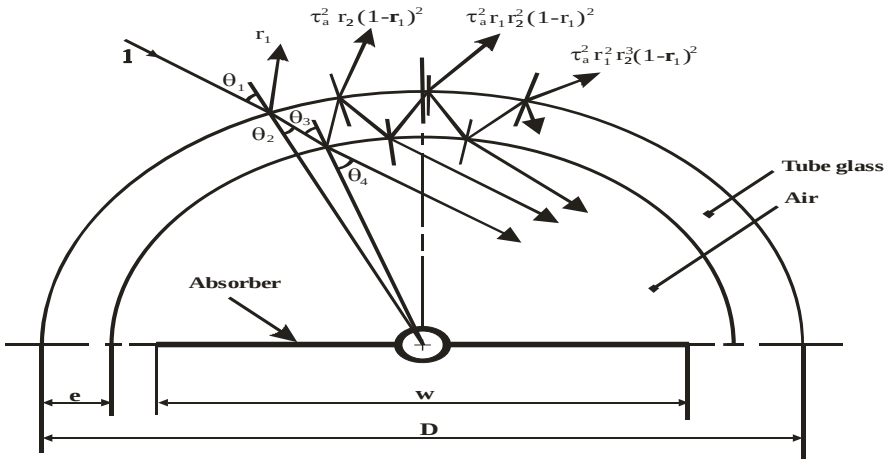

Figure 5.1. Collector cross-section and ray tracing application.

The cosine of the angle of incidence of the absorber θ_a is given by:

$$\cos(\theta_a) = \vec{n}_a.\vec{s} = -\cos(h)\sin(a+\gamma_s)\sin(\beta') + [\sin(\beta)\cos(h)\cos(a+h) + \cos(\beta)\sin(h)]\cos(\beta') \quad (5.11)$$

Figure 5.2. represents a detailed tube section with both absorber tilt angle (β') and the integration angle (ψ).

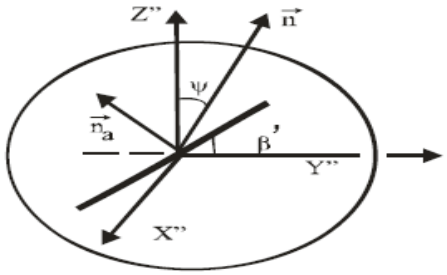

Figure 5.2. Detailed tube section

Taking into account the symmetries and with θ_1 the solution of this system, the integration limits are given by:

$$\begin{cases} \Phi_1 = \xi \\ \Phi_2 = \xi - \theta \end{cases} \quad (5.12)$$

$$\begin{cases} \dfrac{\sin(\theta)}{\sin(\theta_{2)}} = 1 - \dfrac{2e}{D} \\ \dfrac{\sin(\theta_4)}{w} = \dfrac{\cos\left[\theta - \xi - \theta_4 + \left(\arcsin\left(\frac{n1}{n2}\sin\theta_4\right)\right) - \arccos\left(\frac{n1}{n2}\sin\theta\right)\right]}{D - 2e} \end{cases} \quad (5.13)$$

Figure 5.3 presents the integration limits of the radiation received by the plate absorber, depending on the relative position of the Sun.

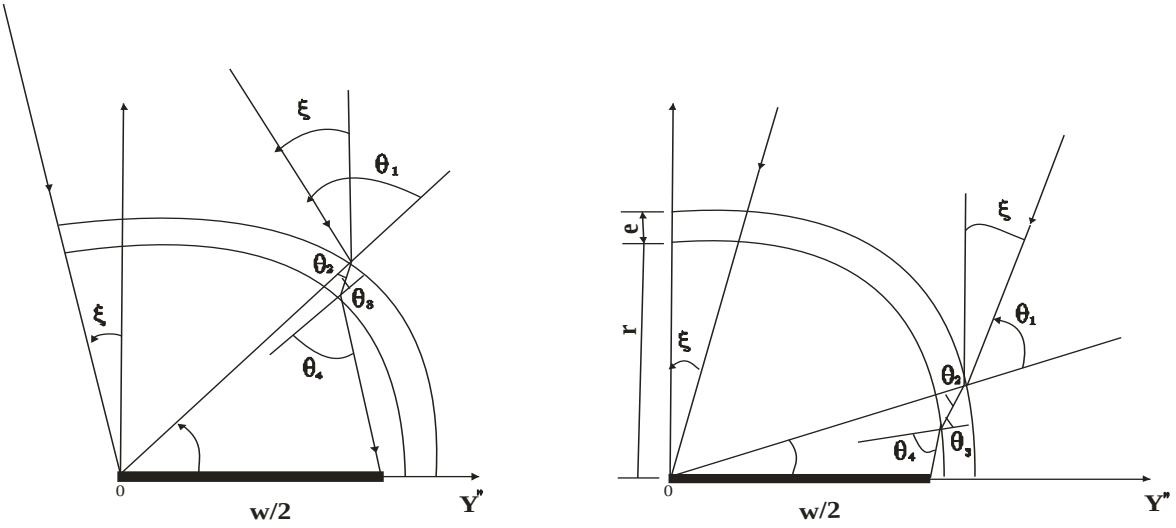

Figure 5.3. The limits of the radiation transmitted by the tube and received by the absorber.

Figure 5.4. represents the longitudinal plane of the parabolic trough collector with the absorber plate.

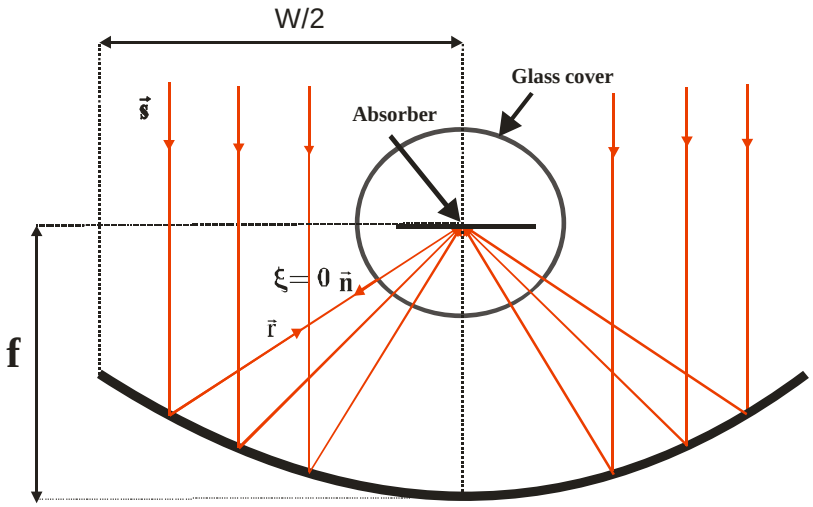

Figure 5.4: The planes of the tube receiver incidence angle

5.2 Thermo-physical properties of the working fluids

5.2.1 Thermo-physical properties of Thermex vapour [132].

Temperature	Latent heat KJ/kg	Vapor viscosity cP*10	Vapor specific Heat Kg/kg°C	Liquid thermal conductivity (W/m °C)
100	354.0	0.67	1.34	0.03
150	338.0	0.78	1.51	0.22
200	321.0	0.89	1.67	0.94
250	301.0	1.00	1.81	3.60
300	278.0	1.12	1.95	8.74
350	251.0	1.23	2.03	19.37
400	219.0	1.34	2.11	41.89
450	185.0	1.45	2.19	81.00

The adjustment models representing the variation thermo-physical properties of Thermex vapor are given by:

$$C_{pv}(T) = 1340\, e^{(-3.0322\,10^{-6}\,T^2+3.0419\,10^{-3}T-0.2704)} \quad (5.14)$$

$$\mu(T) = 6.7.10^{-6}\, e^{(-2.3720.10-6\,T2+3.4936.10-3Tfv-0.3223)} \quad (5.15)$$

$$h_{fg}(T) = -0.6690T^2-110.8333T+3.707310^5 \quad (5.16)$$

5.2.2 **Thermo-physical properties of the heat transfer fluids**

Table 5-2: Thermo-physical properties of TherminolVP-1 vs temperature.

Temperature °C	**Density Kg/m^3**	**Thermal conductivity W/. m. K**	**Heat capacity Kj/Kg.K**	**Dynamic viscosity mPa.s**
12	1071	0.137	1.523	5.48
20	1064	0.136	1.546	4.29
30	1056	0.135	1.575	3.28
40	1048	0.134	1.604	2.60
50	1040	0.133	1.633	2.12
60	1032	0.132	1.662	1.761
70	1042	0.131	1.690	1.492
80	1007	0.130	1.719	1.284
90	1015	0.129	1.747	1.119
100	999	0.128	1.775	0.985
110	991	0.126	1.803	0.875
120	982	0.125	1.831	0.784
130	974	0.124	1.585	0.707
140	965	0.123	1.886	0.642
150	957	0.121	1.913	0.585
160	648	0.120	1.940	0.537
170	940	0.118	1.968	0.494
180	931	0.117	1.995	0.457
190	922	0.115	2.021	0. 424
200	913	0.114	2.048	0.395
210	904	0.112	2.075	0.368
220	895	0.111	2.101	0.345
230	886	0.109	2.128	0.324
240	877	0.107	2.154	0.305
250	867	0.106	2.181	0.288
260	857	0.104	2.207	0.272
270	848	0.102	2.234	0.258
280	838	0.100	2.260	0.244
290	828	0.098	2.287	0.232
300	817	0.096	2.314	0.221
310	806	0.095	2.341	0.211
320	796	0.093	2.369	0.202
330	784	0.091	2.397	0.193
340	773	0.089	2.425	0.185
350	761	0.086	2.454	0.117
360	749	0.084	2.485	0.170
370	736	0.082	2.517	0.164
380	723	0.080	2.551	0.158
390	709	0.078	2.588	0.152
400	694	0.076	2.628	0.146
410	679	0.073	2.674	0.141
420	662	0.071	2.729	0.137
425	654	0.070	2.760	0.134

The models representing the variations of the thermo-physical properties of synthetic oil (TherminolVP-1) with the working temperature are given by[116][133]:

$Cp(T) = 0.002496.T + 5.95.10^{-6} T^2 + 1.509$ [kJ/kg/K] 5.17)

$k(T) = -8.19477.10^{-5}. T - 1.22 T^2 + 0.1377$ [W/m. K] (5.18)

$\mu(T) = 0.001.\left(10^{0.8703} . T^{(0.2877+\log(T^{-0.3638}))}\right)$ [Pa. s] (5.19)

$\rho(T) = -0.90797.T + 78.116 . 10^{-5} . T^2 - 2.367. 10^{-6} T^2 +$

1083.25 [kg/m^3] (5.20)

Table 5-3. Thermophysical Properties of Saturated Water and Steam

Temperature °C	**Liquid**	**Steam**			
	Thermal conductivity W/. m. K $\lambda.10^3$	**Dynamic viscosity N-s/m^2 $\eta.10^7$**	**Thermal conductivity W/. m. K $\lambda.10^3$**	**Heat capacity Kj/Kg. K Cp**	**Latent heat of vaporization Kj/Kg hfg**
100	680	121	24.8	2.034	2257.0
110	383	124	25.8	2.075	2230.2
120	385	128	26.7	2.124	2202.6
130	687	132	27.8	2.180	2174.2
140	687	135	28.8	2.245	2144.7
150	686	139	30.0	2.320	2144.3
160	684	142	31.3	2.406	2082.6
170	681	146	32.6	2.504	2049.5
180	676	149	34.1	2.615	2015.0
190	671	153	35.7	2.741	1978.8
200	664	156	37.5	2.883	1940.7
210	357	160	39.4	3.043	1900.7
220	648	163	41.5	3.223	1858.5
230	639	167	43.9	3.426	1813.8
240	629	171	46.5	3.656	1766.5
250	617	174	49.5	3.918	1716.2
260	604	178	52.8	4.221	1662.5
270	589	182	56.6	4.574	1605.2
280	573	187	60.9	4.996	1543.6
290	557	193	66.0	5.51	1477.1
300	540	198	71.9	6.15	1404.9
310	522	205	79.1	6.69	1326.0
320	503	214	87.8	8.05	1238.6
330	482	225	98.9	9.59	1140.6
340	460	238	113	11.92	1027.9
350	435	256	130	15.95	893.4

The models representing the variations of the thermo-physical properties of Liquid water travelling from the condenser to the evaporator is given by[134].

$k_{water} = 1.68.10^{-3}.T - 5.96341.10^{-6}.T^2 + 1.68$ [W/m. K]. (5.21)

The models representing the variations of the thermo-physical properties of water vapor in the evaporator is given by:

$$\mu(T) = 1.3072.10^{-12}.T^3 - 7.4814.10^{-10}.T^2 + 1.7066.10^7.T + 0.8922.10^{-6} \quad (5.22)$$

$$h_{fg} = -0.0636.T^3 + 26.8788.T^2 - 6829.7412.T + 2.7457.10^6 \quad (5.23)$$

$$k_v = 1,2994.10^{-8}.T^3 - 6.6735.10^{-6}.T^2 + 1.2381.10^{-3}.T - 4.7757.10^{-2} \quad (5.24)$$

$$Cave = 0.2197.10^{-4}.T^4 - 172.4010^{-4}.T^3 + 4.9564.T^2 - 602.1734.T + 2.805.10^4 \quad (5.25)$$

5.3 Properties of glass and metal components of the system[151,152]:

a- Properties of the heat pipe wall made of copper

Heat pipe specific heat Cp_{hp}=381.1 J/kg K

Heat pipe density (ρ_{hp}) = 8954 kg/m^3

b- Properties of the Glass cover

Glass envelop specific heat (Cp_g) 1090 J/kg K

Glass envelop density (ρ_{ab}) 2230 kg/m^3

c- Properties of stainless steel absorber pipe

Absorber pipe specific heat Cp_{ab} =500 J/kg K

Absorber pipe density ρ_p =8020 kg/m^3

5.4 Ambient temperature

The ambient temperatures models which will be presented here have been developed based on measurement data using metrological equipment at Bouzareah (latitude 36°8', longitude 3°12' and altitude 345m). The data have been recorded during five years (2003-2007) with a step time equal to 30 minutes[135].

A cousin function for the time between 6a.m and 6 p.m it is given by:

$$T_a(t) = a(\cos(p_1) + p_2 \quad 5.26)$$

The coefficients, $p_1$and $p_2$and were calculated using the non-linear least-squares method.

The results of the first function are listed in the table.

Table 5-4: The values of the coefficients p1, p2 and a for each month as a function of cosines function.

Month	A	p_1	p_2
January	1.7042	0.421	-3.166
February	1.2978	0.399	-2.701
March	1.79	0.381	-2.662
April	1.4357	0.383	-2.471
May	1.1451	0.379	-2.470
Jun	2.0457	0.375	-2.475
July	1.9139	0.382	-2.678
August	1.9523	0.379	-2.497
September	1.587	0.393	-2.487
October	1.3298	0.450	-2.692
November	1.2387	0.423	-2.639
December	1.0377	0.434	-2.805

The second part is adjusted by the exponential function for the time between 6 p.m and 6 a.m:

$$T(t) = C(1 - exp\left(-\left(\frac{t_0 - t(i)}{b}\right)\right) \tag{5.27}$$

Applying the Method of non-linear least squares, Hakem et al [135] determined the average monthly values of the coefficient *b*. The values of these coefficients are listed in table 5.4.

Table 5-5. The values of coefficient b for each month.

Month	b	Month	b
January	6.7224	July	1.0001
February	1.8245	August	3.2958
March	5.0933	September	4.073
April	5.4234	October	5.9553
May	3.8759	November	5.0012
June	4.4594	December	3.8215

In figure 5.5, represents the experimental data (red colour) and the predicted ambient temperature using the developed model in the present study. The model was divided into two parts and modelled using the function (5.26) and function (5.27).

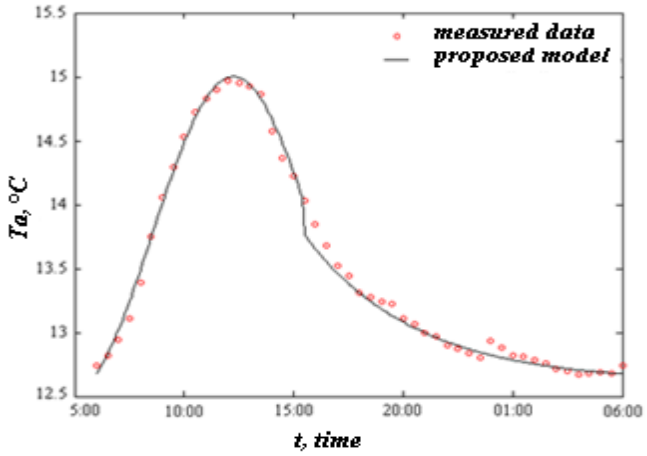

Figure 5.5. Modelling of ambient temperature

The curves in figure 5.5 can be adjusted by the Weibull law, but after a modification using the following equation.

$$T(t) = T_m + \left(\frac{t}{P_3}\right)^{P_5} \exp\left(-\frac{t}{P_3}\right)^{P_4} c \qquad (5.28)$$

Table 5-6: Modelling of ambient temperature.

Month	C	P3	P4	P5	$\bar{T}_{min}$
January	1.91	3.38	1.25	3.03	11.06
February	5.12	9.01	3.67	1.27	9.76
March	8.97	6.19	1.73	1.90	13.02
April	7.07	7.90	1.96	1.13	12.44
May	4.92	9.15	2.61	0.94	14.04
June	7.34	10.86	2.67	0.91	18.76
July	6.45	10.69	5.59	0.74	25.08
August	8.22	9.36	2.71	0.96	25.32
September	7.59	8.29	2.30	1.19	18.56
October	4.50	2.90	1.15	2.36	16.33
November	5.59	4.41	1.44	2.13	12.67
December	5.51	6.36	1.95	1.80	12.99

5.5 Second order Runge Kutta method

The $\overline{f(x,y)}$ is estimated at half a step, (x_i+Δx/2) and $\hat{y}$ (x_i+Δx/2) (estimated value of y at

((x_i+Δx/2), as follows :

$\overline{f(x,y)}$ = f(x_i+ Δx/2, $\hat{y}$ (x_i+Δx/2))

Avec :

$\hat{y}$ (x_i+ Δx/2) = y (x_i), f (x_i+ y_i)* Δx/2

The resolution is done step by step according to the following algorithm:

By posing $T = [T_g \;\; T_{evw} \;\; T_{cw} \;\; T_{tc} \;\; T_f]$

The system becomes:

$$\frac{dT}{dt} = f(t,T)$$

Put the calculation program for a time t and a temperature distribution T defined in a function

End the program with the calculation of the function f (vector).

For i = 2 to n:

$$fi = feval(\text{fonction}, t(i), T(i))$$

$$fi12) = feval(\text{fonction}, t(i) + \Delta t/2), T(i) + fi * \Delta t/2);$$

$$T(i+1) = T(i) + fi12 * \Delta t;$$

end

5.6 Types of capillary network

The operating equation and the calculation of the pressure drops bring out two important parameters attached to the capillary network:

The permeability K connected to the pressure loss of the liquid circulation in the network.

The effective pore radius r_{cap} of the capillary connected to the pumping capacity of the network.

Moreover, the calculation of K and r_{cap} can reveal two other quantities characteristic of the porous medium:

- The porosity ε is the ratio of the volume of the saturated liquid to the total volume of the network.

- A characteristic dimension of the porous medium (grain diameter for sintered material, wire diameter for fabrics, etc.).

Wick type	Capillary pumping	Thermal conductivity	Permeability	Comments
 A. Wrapped Screen	High	High	Low–average	Single or multiple wraps of wire screen mesh
 B. Sintered Metal	High	Average	Low–average	Packed spherical particles, felt metal fibers or powder
 C. Axial Grooves	Low	High	Average–high	Rectangular, circular, triangular, or trapezoidal grooves
 D. Open Annulus	Low	Low	High	Wire screen mesh spaced from wall
 E. Open Artery	Low	High	High	Wire screen mesh formed into artery and wall lining
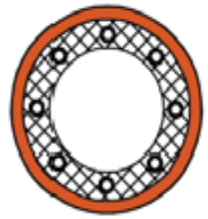 F. Integral Artery	High	High	Average–high	Homogeneous material with built–in arteries

Figure 5.6: Typical homogeneous wick designs (Faghri 2014)

5.7 Thermal analysis of the heat pipe

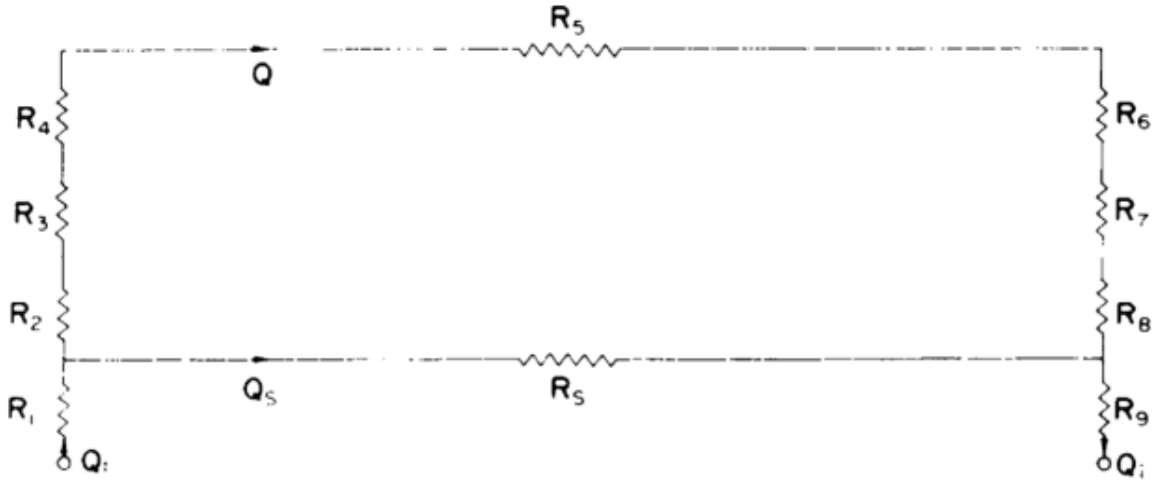

Figure 5.7: Electro thermal analogue for a heat pipe

The resistances can be summarized as follows [136][132]:

R_1 and R_9 are the normal heat transfer resistances for heating a solid surface.

R_2 and R_8 represent the thermal resistance of the heat pipe wall.

R_3 and R_7 take account of the thermal resistance of the wick structure and include any temperature difference between the wall and the liquid together with conduction through the saturated wick.

R_7 is made is up principally from the saturated wick.

R_4 and R_6 are the thermal resistances corresponding to the vapor-liquid surfaces.

R_5 is due to the temperature drop ΔT_5 along the vapor column.

Estimates of the order of magnitude for each of these resistances indicate that R_4, R_5 and R_6 can be neglected:

$$Q = \frac{T_e - T_c}{R_1 + R_2 + R_3 + R_7 + R_8 + R_9} \tag{5.29}$$

Table 5-7. Thermal analogue for a heat pipe

N°	Defining relation	Resistances
1	$Q_i = h_e A_e \Delta T_1$	$R_1 = \frac{1}{A_e h_e}$
2	Plane geometry: $Q_e = \frac{A_e k_p \Delta T_2}{e}$ Cylindrical geometry: $Q_e = \frac{A_e k_p \Delta T_2}{r_2 \log(\frac{r_2}{r_2})}$	$R_2 = \frac{e}{A_e k_p}$ $R_2 = \frac{\log(\frac{r_2}{r_1})}{2\pi L_e k_p}$
3	Plane geometry: $Q_e = \frac{k_w A_e \Delta T_3}{D_w}$ Cylindrical geometry: $Q_e = \frac{A_e k_w \Delta T_3}{\log(\frac{r_2}{r_1})}$	$R_3 = \frac{e_w}{k_w A_e}$ $R_3 = \frac{\log(\frac{r_2}{r_1})}{2\pi L_e k_w}$
4	$Q_e = \frac{h_{fg}^2 A_e P_v \Delta T_4}{RT^2\sqrt{2\pi RT_s}}$	$R_4 = \frac{RT^2\sqrt{2\pi RT}}{h_{fg}^2 P_v A_e}$
5	$\Delta T_5 = \frac{RT^2 \Delta P_v}{h_{fg} P_v}$	$R_5 = \frac{RT^2 \Delta P_v}{Q h_{fg} P_v}$
6	$Q_c = \frac{h_{fg}^2 A_c P_v \Delta T_6}{RT^2\sqrt{2\pi RT}}$	$R_4 = \frac{RT^2\sqrt{2\pi RT}}{h_{fg}^2 P_v A_c}$
7	Plane geometry: $Q_e = \frac{k_w A_c \Delta T_7}{D_w}$ Cylindrical geometry: $Q_e = \frac{A_c k_w \Delta T_3}{r_2 \log(\frac{r_2}{r_1})}$	$R_7 = \frac{e_w}{k_w A_c}$ $R_7 = \frac{\log(\frac{r_2}{r_1})}{2\pi L_c k_w}$
8	Plane geometry: $Q_e = \frac{A_c k_p \Delta T_8}{e}$ Cylindrical geometry: $Q_e = \frac{A_c k_p \Delta T_8}{r_2 \log(\frac{r_2}{r_2})}$	$R_8 = \frac{e}{A_c k_p}$ $R_8 = \frac{\log(\frac{r_2}{r_1})}{2\pi L_c k_p}$
9	$Q = h_c A_c \Delta T_9$	$R_9 = \frac{1}{A_c h_c}$

Estimates of the order of magnitude for each of these resistances indicate that several simplifications can be made, that is, the axial resistance of both the heat pipe wall and the liquid-wick combination may be treated as open circuits and neglected, the liquid-vapor interface resistance and the axial vapor resistance can typically be assumed to be negligible, leaving only the pipe wall radial resistances and the liquid-wick resistances at both the evaporator and condenser.

Table 5-8: Effective Thermal Conductivity for Liquid-Saturated Wick Structures[122]

Wick structures	k_{eff}
Wick and liquid in series	$\frac{k_l k_w}{\varepsilon k_w + k_l(1+\varepsilon)}$
Wick liquid in parallel	$\varepsilon k_l + k_w(1-\varepsilon)$
Wrapped screen	$\frac{k_l[(k_l+k_w)-(1-\varepsilon)(k_l-k_w)]}{[(k_l+k_w)+(1-\varepsilon)(k_l-k_w)]}$
Packed spheres	$\frac{k_l[(2k_l+k_w)-2(1-\varepsilon)(k_l-k_w)]}{(2k_l+k_w)+(1-\varepsilon)(k_l-k_w)}$
Rectangular grooves	$\frac{(w_f k_l k_w \delta)-w k_l(0.185 w_f k_w-\delta k_l)}{(w+w_f)+(0.185 w_f k_l-\delta k_f)}$

5.8 Limits of the capillary heat pipe

The operation of heat pipes and thermosiphons is based on the coexistence of the vapor and liquid phases of a heat transfer fluid under conditions close to saturation. Thus, a first obvious operating condition is the temperature range of the fluid, which is between the triple point and the critical point. Besides, the strong evolution of thermophysical properties of the fluid with the temperature leads to the occurrence of phenomena blocking the transferred flow at a maximum value. We will present these operating limits by order of appearance when the operating temperature rises.

The operating limits in order of appearance when the operating temperature increases are as follows:

The first two limits (viscous and sonic) appear for temperatures at the beginning of the operating range and are related to the vapor phase. Then comes the two main limitations: the entrainment limit related to the liquid-vapor interaction for the thermosiphons and the capillary limit related to the pumping capacities of the capillary structures of the heat pipes. Finally, the boiling limit appears for high temperatures and high flux densities at the evaporator.

5.8.1 Capillary limit

The capillary limit is an essential element in the design of capillary-type heat pipes commonly used in space or microcomputer applications. Nevertheless, it is necessary to pay attention to the calculation of pressure drops by considering the permeability of the capillary structure containing the liquid and the shear conditions at the liquid-vapor interface.

Exceeding the capillary limit leads to rapid drying of the evaporator and a very rapid increase in the overall evaporation resistance. The resultant heating often blocks rewetting of the wall. In such a situation, it is imperative to reduce the flow rate significantly to allow the heat pipe to be re-primed.

The operating cycle of a capillary pumped heat pipe includes an essential phase which is the return of the liquid from the condensation zone to the evaporation zone under the effect of capillary pumping. These forces must compensate for the loss of dynamic loads generated by fluid flow and static pressure drops from volume forces. Since capillary forces have a maximum value that is a function of the mean pore radius of the structure and dynamic pressure losses are an increasing function of the mass flow rate of the fluid, there is a limit to the transfer possibilities of heat pipes, known as the capillary limit. This limit is not valid for thermosiphons.

The calculation of the capillary limit is therefore based on the equilibrium between the maximum capillary motive pressure Δp_{cap} that can be supplied and the liquid and vapor pressure drop along with the flow[84]:

$$\Delta p_{cap} = \int_{X_{min}}^{X_{max}} \left(\frac{dp_v}{dX} - \frac{dp_l}{dX} \right) dX \tag{5.30}$$

Where:

p_v Is the vapor pressure

p_v Is the liquid pressure

The capillary motive pressure is maximum when the main bending radii of the interface are minimal:

$$\Delta p_{cap,max} = \sigma \left(\frac{1}{r_{rap,1}} + \frac{1}{r_{cap,2}} \right) \cos(\theta_w) \tag{5.31}$$

Where:

σ Is the surface tension

θ_w Is the wetting angle

For a heat pipe with circular porous media in a laminar flow condition for the vapor phase, the maximum allowed heat flux Q_{max} is given by:

$$Q_{max} = \frac{\frac{i\sigma\cos(\theta_w)}{r_e} \pm \rho_l g L_t \sin(\alpha)}{\frac{\mu_l L_{eff}}{\rho_l A_w K h_{fg}} + \frac{8\mu_v L_{eff}}{\pi \rho_v r_v^4 h_{fg}}} \tag{5.32}$$

$$L_{eff} = \frac{1}{\dot{Q}_{max}} \int_0^{l_t} \dot{Q}(z) dz \tag{5.33}$$

Or, for an injected uniform flow:

$$L_{eff} = \frac{1}{2}(L_e + L_c) + L_a \quad (5.34)$$

Where:

$\dot{Q}\ (z)$ Represents the distribution of the extracted flux along the condenser

L_{eff} Is the effective length of the evaporator

h_{fg} Is the latent heat of vaporization

μ_l , μ_v Are the dynamic viscosity of vapor liquid and vapor respectively

e, c and a refer respectively to the length of the evaporator, condenser and adiabatic zone

i = 1 for a heat pipe with longitudinal grooves

i = 2 for other types of structures

K (m^2) permeability of the porous medium.

The work of Hoa[137] has shown the validity of this approach which allows an evaluation of the capillary limit with maximum errors of the order of 20 to 30 %.

5.8.2 **Entrainment limit**

This limit corresponds to the influence of the interaction between the countercurrent flows of the liquid and vapor phases. As the relative speeds increase, the shear at the interface liquid-steam tends to limit the mass flow rates and therefore the transferable power. In thermosiphons, you can even achieve liquid droplet entrainment in the steam. The evaluation of the entrainment limit has been the subject of numerous studies in the literature, without leading to any reliable approaches for the majority of cases. However, an assessment of this limit can be given by two different formulations depending on the structuring of the interface. For capillary pumped heat pipes, this interface is by definition strongly influenced by the tensile forces of the surface. Approaches are then based on the number of Weber (We) which compares inertial pressure to capillary pressure:

$$W_e = \frac{Inertial\ force}{Capillary\ force} = \frac{\rho_v \overline{U}_v^2}{\sigma / l_{ref}} \quad (5.35)$$

Where:

l_{ref} (m) Is the characteristic dimension of the capillary structure (e.g.: half-width of a groove or radius of the pore of a porous medium).

$\bar{U}_v$ Is the average vapor velocity.

We will retain the driven power, the expression provided by Prenger and Kemme [138]:

$$\dot{Q}_{ent} = \sqrt{\frac{2\pi}{K_\alpha}} \sqrt{\frac{\sigma \rho_v}{l_{ref}}} \frac{l_{eff}}{l^*_{ref}} A_v h_{fg} \tag{5.36}$$

With: $l^*_{ref} = 6.7\ 10^{-4} m$

K_α = 1.234 for laminar flow of the vapour phase.

Beyond that, the authors consider that capillary forces are no longer preponderant and the expression for a smooth tube thermosiphon should be used. We use the expression recommended by Faghri [87]:

$$\dot{Q}_{ent} = K_e L_v A_v [g\sigma - \rho_v)]^{1/4} [\rho_l^{-\frac{1}{4}}]^{-2} \tag{5.37}$$

With:

$$K_e = \left(\frac{g(\rho_l - \rho_v}{\sigma}\right)^{0.14} th^2(BO^{\frac{1}{4}}) \tag{5.38}$$

And

$$BO = D_{int} \left[\frac{g(\rho_l - \rho_v)}{\sigma}\right]^{1/2} \tag{5.39}$$

Where:

BO is the boiling number

5.8.3 **Viscous limit**

For common fluids having an adiabatic temperature a few Kelvin higher than the temperature of the triple point, the viscous limit is not the phenomenon to be taken into account for dimensioning the heat pipe. However, it is necessary to be attentive to this limit for heat pipes for liquid metals such as lithium, whose saturation curve derivative is very low. Exceeding the viscous limit leads to an increase in the operating temperature of the heat pipe.

The Clausius-Clapeyron relationship for a perfect gas relates pressure variations p_v to temperature variations T_v:

$$dp_v = \frac{\rho_v L_v}{T_v}\, dT_v \tag{5.40}$$

Thus, for a given adiabatic temperature close to the triple point, and a steam temperature equal to the triple point at the end of the condenser, there is then a given pressure difference between these two points. The viscous limit is calculated by considering an isothermal incompressible laminar flow of Poiseuille type. By adapting the work of Busse [139] to the uniformity of the reference temperatures in the middle of the adiabatic zone, the viscous limit is expressed by:

$$\dot{Q}_{Vis} = \frac{\pi r_V^4 L_{V,a}}{16\mu_{V,PT}\, l_{eff}^i}\left(1 - \left(\frac{P_{PT}}{P_{V,a}}\right)^2 \rho_{v,a} P_{V,a}\right) \tag{5.41}$$

With r_v (m) radius of the steam passage section.

$$l_{eff}^i = \frac{1}{\dot{Q}_{vis}} \int_{l'}^{l_t} \dot{Q}\,(\mathrm{Z})\,\mathrm{dz} \tag{5.42}$$

And

$$l' = l_c + \frac{l_a}{2} \tag{5.43}$$

"PT" refers to the triple point and "a" to the adiabatic zone.

$\dot{Q}$ (Z) represents the distribution of the extracted stream through the condenser. If the flow is homogeneous, we simply have:

$$l_{eff}^i = \frac{l_c + l_a}{2} \tag{5.44}$$

Otherwise, an iterative procedure is required to solve the problem.

5.8.4 **Sonic limit**

The sonic limit is a critical limit for the fluids with a very low saturation pressure such as liquid metals at low temperatures. This limit leads to a limitation of the transferable flow and imposes a temperature setting of liquid metal heat pipe, to avoid destructive overheating of the evaporator zone.

The evaporator zone of a heat pipe or thermosiphon corresponds to a flow zone with a material injection which can be assimilated to a Laval nozzle (constant mass flow rate with section reduction). This similarity is expressed by the differentiation of the mass flow rate $\dot{m}_v$ expression in a section S_v:

$$\frac{d\dot{m}_v}{\dot{m}_v} = \frac{d\rho_v}{\rho_v} + \frac{dU_v}{U_v} + \frac{dA_v}{A_v} \tag{5.45}$$

In both cases, for a given thermodynamic flow condition (isothermal, adiabatic or saturated steam), this leads to an increase in the steam velocity U_v. Due to the coexistence of the liquid and in the case of steam, we have retained the expression of the sonic limit for a flow in a saturated state. This approach provides a boundary between the isothermal approach [139] and the isentropic approach [140][87].

$$\dot{Q}_{son} = \frac{\pi}{4\sqrt{A_s}} D_v^2 L_{v,a} \sqrt{\gamma r_g T_{v,a}} \tag{5.46}$$

$$A_s = \frac{\overline{U}_{v,1}^2}{\overline{U}_{v,1}^2} \tag{5.47}$$

With γ ratio of thermal mass capacities at constant pressure and volume, r_g is the mass constant of the vapor considered to be a perfect gas.

Busse [139] provides a value of $A_s = 1.11$ for a 2D flow with a cosine profile.

5.8.5 **Boiling limit**

The boiling point is characterized by the appearance of bubbles within the liquid in the evaporator. The first stage of boiling is commonly referred to as nucleate boiling and corresponds to the formation of bubbles of very small diameter that can form and re-condense within the liquid, in this case boiling favors the heat transfer. However, in a capillary-pumped heat pipe, the explosion of these bubbles at the liquid-vapour interface can lead to the capillary motor rupture. It is therefore customary to consider this boiling limit as a strict limit for heat pipes, although there may have been cases where boiling in heat pipes of the type "two-phase heat diffusers"... was beneficial [141]. On the other hand, for thermosiphons, boiling on the walls of the evaporator is part of the process integral part of the transfer process. However, when bubbles are growing very fast, coalescence between different bubbles can lead to the ejection of a large amount of liquid to the condenser. This phenomenon implies unstable functioning with strong temperature oscillations. The boiling limit is calculated from the superheat necessary to maintain a vapor bubble of radius R_b. The overpressure in the vapor bubble, which must balance the capillary pressure, is calculated from the Clapeyron relationship:

$$\Delta T_{eb} = T_{v,bulle} - T_l = \frac{\sigma T_{sat}}{\rho_v h_{fg}} \left(\frac{2}{R_b} \right) \tag{5.48}$$

Within a capillary structure, the pressure in the liquid being related to the radius of the meniscus, the superheat at the wall T_p can be expressed with the temperature of the vapor phase T_{sat} by:

$$\Delta T_{eb} = T_p - T_{sat} = \frac{\sigma T_{sat}}{\rho_v h_{fg}} \left(\frac{2}{R_b} - \left(\frac{1}{r_{cap,1}} + \frac{1}{r_{cap,1}} \right) \right) \quad (5.49)$$

The flow is then expressed as:

$$\dot{Q}_{eb} = G_{ev} \Delta T_{eb} \quad (5.50)$$

With G_{ev} (W. K^{-1}) conductance to the evaporator.

Or, for a circular heat pipe with outside diameter D_{ext} and diameter under the capillary structure D_{int}:

$$\dot{Q}_{eb} = \frac{2\pi k_{eff}}{ln\left(\frac{d_{ext}}{d_{int}}\right)} \frac{\sigma\, T_{sat}}{\rho_v L_v} \left(\frac{2}{R_b} - \frac{i}{r_{cap}} \right) \quad (5.51)$$

With k_{eff}(W.m^{-1}.K^{-1}) effective thermal conductivity of the porous structure.

5.9 Choice of the working fluid

The choice of the working fluid is the first step in determining the type of the heat pipe at a given application. This is determined by the operating temperature range of the heat pipe and then by the desired level of performance. The environmental impact, the flammability and the toxicity of the fluid are also important criteria, which can lead to the removal of fluid from their good thermal performance.

Example: this may be the case for ammonia or methanol (toxicity), CFC-type of fluids or mercury (environmental impact).

The performance of various fluids can be compared using the merit number M_c. The merit number of a fluid is a number built from several thermophysical properties, chosen and combined according to the type of heat pipe, so that the higher its value at a given temperature, the better the fluid performance for a functioning heat pipe at this temperature. For a capillary heat pipe, the merit number M_c (in W/m^2) is defined by:

$$M_c = \frac{\rho_l\, \sigma\, L_v}{\mu_l} \quad (5.52)$$

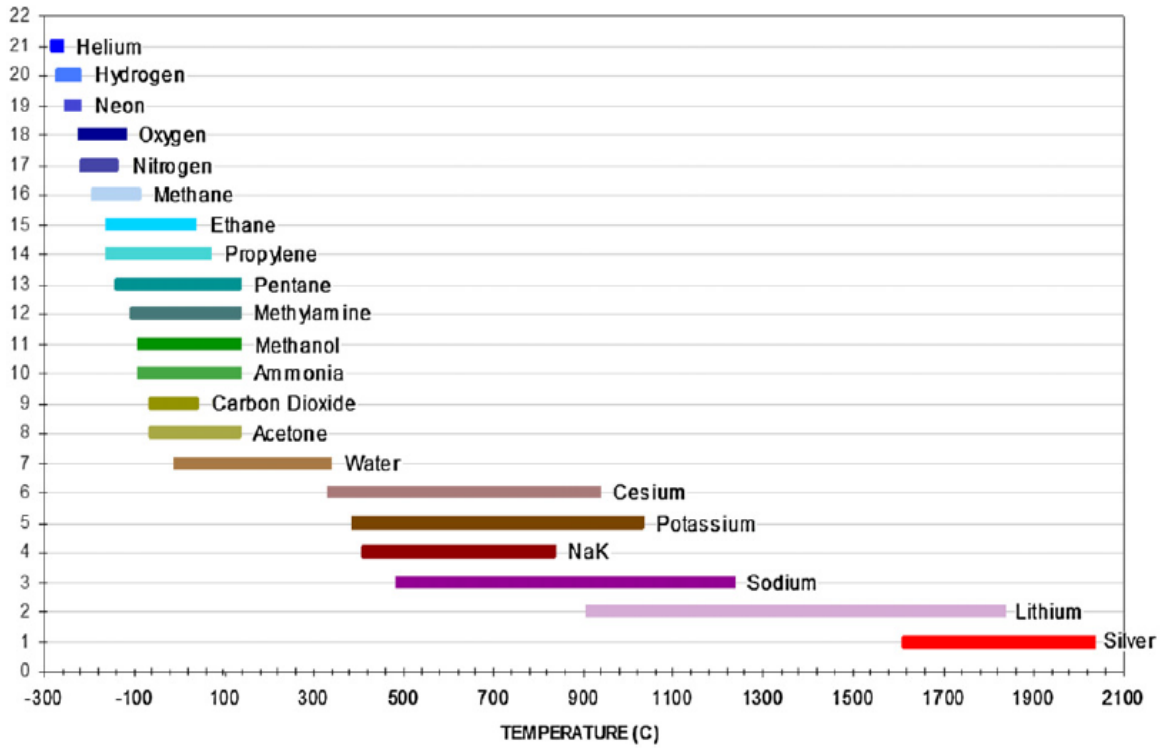

Figure 5.8. Operating temperature range of common working fluids (Rafferty, n.d.).

5.10 Choice of the envelope tube

The nature of the envelope material of a heat pipe is first of all conditioned by the nature of the internal fluid that we have previously chosen. Indeed, no chemical reaction, however weak it may be, cannot be tolerated between the fluid and its casing because the gases emissions from this reaction, even in very small quantities, would probably lead to the blocking of the heat pipe's functioning.

Once selected, the compatible material(s) with the heat pipe fluid, it must be checked that it is also corrosion-resistant from the environment outside the heat pipe and plan, if necessary, a corrosion-resistant coating of the pipe.

Finally, it is essential to ensure that the material, in the chosen thickness, resists the internal pressure, which can be high, taking particular care to avoid overheating which, when the steam remains saturated in the heat pipe, can lead to significant accidental overpressure (this requires examination of the fluid saturation pressure curve and the critical pressure).

Table 5-9. Heat pipe's working fluid and their compatible materials.

Working fluid	**Compatible Materials**
Ammonia	Aluminium, stainless steels
Synthetic refrigerants (HCFC, HFC)	Aluminium, copper, steels
Acetone	Copper, steel
Methanol, ethanol	Copper, steel
Water	Copper, mild steels
Toluene	Steels, stainless steels
Gilotherm DO	Steels, stainless steels
Naphthalene	Steels, stainless steels
Mercury	Low carbon steels, stainless steels up to 500 ^{o}C
Potassium	Stainless steel AISI 316, nickel
Sodium	Stainless steel AISI 316, nickel, tungsten, molybdenum
Lithium	Tungsten, molybdenum, molybdenum-rhenium alloy

REFERENCES

[1] I. E. A. OECD, “Energy and air pollution: world energy outlook special report 2016,” 2016.

[2] A. Ummadisingu and M. S. Soni, “Concentrating solar power–technology, potential and policy in India,” *Renew. Sustain. energy Rev.*, vol. 15, no. 9, pp. 5169–5175, 2011.

[3] A.-R. Nadia, N. A. M. Isa, and M. K. M. Desa, “Advances in solar photovoltaic tracking systems: A review,” *Renew. Sustain. energy Rev.*, vol. 82, pp. 2548–2569, 2018.

[4] M. T. Islam, N. Huda, A. B. Abdullah, and R. Saidur, “A comprehensive review of state-of-the-art concentrating solar power (CSP) technologies: Current status and research trends,” *Renew. Sustain. Energy Rev.*, vol. 91, pp. 987–1018, 2018.

[5] A. B. Awan, M. N. Khan, M. Zubair, and E. Bellos, “Commercial parabolic trough CSP plants: Research trends and technological advancements,” *Sol. Energy*, vol. 211, pp. 1422–1458, 2020.

[6] V. K. Jebasingh and G. M. J. Herbert, “A review of solar parabolic trough collector,” *Renew. Sustain. Energy Rev.*, vol. 54, pp. 1085–1091, 2016.

[7] D. Zhan, H. Zhang, Y. Liu, S. Li, and J. Zhuang, “Investigation on medium temperature heat pipe receiver used in parabolic trough solar collector,” *ISES Sol. World Congr. 2007, ISES 2007*, vol. 3, no. 5, pp. 1823–1827, 2007, doi: 10.1007/978-3-540-75997-3_372.

[8] A. El Fadar, A. Mimet, and M. Pérez-García, “Study of an adsorption refrigeration system powered by parabolic trough collector and coupled with a heat pipe,” *Renew. Energy*, vol. 34, no. 10, pp. 2271–2279, 2009, doi: 10.1016/j.renene.2009.03.009.

[9] M. R. Yaiche, A. Bouhanik, S. M. A. Bekkouche, A. Malek, and T. Benouaz, “Revised solar maps of Algeria based on sunshine duration,” *Energy Convers. Manag.*, vol. 82, pp. 114–123, 2014.

[10] J. A. Duffie and W. A. Beckman, *Solar engineering of thermal processes*. John Wiley & Sons, 2013.

[11] M. Capderou, “Atlas Solaire de l’Algérie, modèles théoriques et expérimentaux,” *Vol. 1, T1, Off. des Publ. Univ. Algérie*, 1987.

[12] N. Zhao, X. Zeng, and S. Han, “Solar radiation estimation using sunshine hour and air pollution index in China,” *Energy Convers. Manag.*, vol. 76, pp. 846–851, 2013.

[13] W. L. Diabaté L, Remund J, “Linke turbidity factors for several sites in Africa,” *Sol Energy*, vol. 75:111–9, 2003.

[14] I. A. Djafer D, “Estimation of atmospheric turbidity over Ghardaïa city,” *Atmos Res*, vol. 128:76–84, 2013.

[15] Y. Marif, H. Benmoussa, H. Bouguettaia, M. M. Belhadj, and M. Zerrouki, “Numerical simulation of solar parabolic trough collector performance in the Algeria Saharan region,” *Energy Convers. Manag.*, vol. 85, no. October 2017, pp. 521–529, 2014, doi: 10.1016/j.enconman.2014.06.002.

[16] M. Günther, “Advanced CSP teaching materials, chapter 2: Solar radiation, enerMENA.” DLR, 2012.

[17] H. G. Wagemann, “Eschrich,“,” *Grundlagen der photovoltaischen Energiewandlung, Stuttgart, Teubner*, 1994.

[18] C. G. Abbot, *Annals of the Astrophysical Observatory of the Smithsonian Institution:(vol. 2) By Charles Greely Abbot and FE Fowle*. US Government Printing Office, 1908.

[19] F. S. Johnson, "The solar constant," *J. Atmos. Sci.*, vol. 11, no. 6, pp. 431–439, 1954.

[20] M. P. Thekaekara, "Solar radiation measurement: Techniques and instrumentation," *Sol. Energy*, vol. 18, no. 4, pp. 309–325, 1976, doi: 10.1016/0038-092X(76)90058-X.

[21] R. C. Frohlich, "Contemporary measures of the solar constant: The solar output and its variations." Colorado Associated University Press, Boulder, CO, 1977.

[22] J. R. Hickey *et al.*, "Extraterrestrial solar irradiance variability two and one-half years of measurements from Nimbus 7," *Sol. Energy*, vol. 29, no. 2, pp. 125–127, 1982.

[23] R. C. Willson, S. Gulkis, M. Janssen, H. S. Hudson, and Ga. Chapman, "Observations of solar irradiance variability," *Science (80-.).*, vol. 211, no. 4483, pp. 700–702, 1981.

[24] C. H. Duncan, R. C. Willson, J. M. Kendall, R. G. Harrison, and J. R. Hickey, "Latest rocket measurements of the solar constant," *Sol. Energy*, vol. 28, no. 5, pp. 385–387, 1982.

[25] S. Younes and T. Muneer, "Improvements in solar radiation models based on cloud data," *Build. Serv. Eng. Res. Technol.*, vol. 27, no. 1, pp. 41–54, 2006.

[26] C. P. de B. et Ch, "Vauge,''Le gisement solaire," *Eval. la Ressour. énergétique'', Tech. Doc. Lavoisier Paris*, 1982.

[27] M. Capderou, "Modeles théoriques et expérimentaux, Atlas solaire de l'Algérie." Office des Publications Universitaires, Algérie, 1987.

[28] J. Hofierka and M. Suri, "The solar radiation model for Open source GIS: implementation and applications," in *Proceedings of the Open source GIS-GRASS users conference*, 2002, vol. 2002, pp. 51–70.

[29] M. Gunther, "Solar Radiation - Advanced CSP Teaching Materials," *Adv. CSP Teach. Mater.*, pp. 16–21, 2011, [Online]. Available: http://www.scientificamerican.com/article/solar-radiation/#.

[30] T. Mancini *et al.*, "Dish-stirling systems: An overview of development and status," *J. Sol. Energy Eng. Trans. ASME*, vol. 125, no. 2, pp. 135–151, 2003, doi: 10.1115/1.1562634.

[31] C. K. Ho, "Overview of Concentrating Solar Power Research at Sandia Outline Sandia CSP Research Integration of FOCUS and CSP Doing work with Sandia," 2017.

[32] S. A. Kalogirou, "Solar thermal collectors and applications," *Prog. energy Combust. Sci.*, vol. 30, no. 3, pp. 231–295, 2004.

[33] A. Fernández-García, E. Zarza, … L. V.-R. and, and 2010, "Parabolic-trough solar collectors and their applications," *Renew. Sustain. Energy Rev. 14 1695–1721.*, Accessed: Dec. 16, 2019. [Online]. Available: https://www.sciencedirect.com/science/article/pii/S1364032110000675.

[34] H. Price *et al.*, "Advances in parabolic trough solar power technology," *J. Sol. Energy Eng. Trans. ASME*, vol. 124, no. 2, pp. 109–125, 2002, doi: 10.1115/1.1467922.

[35] A. Rabl, *Active solar collectors and their applications*. Oxford University Press on Demand, 1985.

[36] K. Frank, "Solar heating and cooling: active and passive design," 1982.

[37] M. Günther, M. Joemann, and S. Csambor, “Parabolic trough technology,” *Adv. CSP Teach. Mater.*, 2011.

[38] P. Daniel, Y. Joshi, and A. K. Das, “Numerical investigation of parabolic trough receiver performance with outer vacuum shell,” *Sol. Energy*, vol. 85, no. 9, pp. 1910–1914, 2011.

[39] Y. Krishna, M. Faizal, R. Saidur, K. C. Ng, and N. Aslfattahi, “State-of-the-art heat transfer fluids for parabolic trough collector,” *Int. J. Heat Mass Transf.*, vol. 152, 2020, doi: 10.1016/j.ijheatmasstransfer.2020.119541.

[40] P. Sansoni *et al.*, “Optical collection efficiency and orientation of a solar trough medium-power plant installed in Italy,” *Renew. Energy*, vol. 36, no. 9, pp. 2341–2347, 2011, doi: 10.1016/j.renene.2011.02.004.

[41] J. T. Pytilinski, “Solar energy installations for pumping irrigation water,” *Sol. Energy*, vol. 21, no. 4, pp. 255–262, 1978.

[42] J. Ericsson, “The sun motor and the sun’s temperature.” Nature Publishing Group, 1884.

[43] R. A. Maier W, “Vorrichtung zur unmittelbaren Verwendung der Sonnenwa¨rme zur Dampferzeugung,” Patent Nr. 231294.

[44] F. Shuman and C. V. Boys, “Sun-boiler.” Google Patents, Sep. 25, 1917.

[45] L. C. Spencer, “A comprehensive review of small solar-powered heat engines: Part I. A history of solar-powered devices up to 1950,” *Sol. Energy*, vol. 43, no. 4, pp. 191–196, 1989.

[46] C. F. Kutscher, *Design Approaches for Solar Industrial Process Heat Systems: Nontracking and Line-focus Collector Technologies*, vol. 253, no. 1356. Solar Energy Research Institute, 1982.

[47] D. Kearney and H. Price, “Advances in parabolic trough solar power technology,” *Adv. Sol. energy*, vol. 16, 2002.

[48] A. Kasaeian, G. Nouri, P. Ranjbaran, and D. Wen, “Solar collectors and photovoltaics as combined heat and power systems: a critical review,” *Energy Convers. Manag.*, vol. 156, pp. 688–705, 2018.

[49] G. Kumaresan, P. Sudhakar, R. Santosh, and R. Velraj, “Experimental and numerical studies of thermal performance enhancement in the receiver part of solar parabolic trough collectors,” *Renew. Sustain. Energy Rev.*, vol. 77, pp. 1363–1374, 2017.

[50] Y. C. S. Too and R. Benito, “Enhancing heat transfer in air tubular absorbers for concentrated solar thermal applications,” *Appl. Therm. Eng.*, vol. 50, no. 1, pp. 1076–1083, 2013.

[51] K. S. Reddy, K. R. Kumar, and C. S. Ajay, “Experimental investigation of porous disc enhanced receiver for solar parabolic trough collector,” *Renew. Energy*, vol. 77, pp. 308–319, 2015.

[52] J. Li, Z. Wang, J. Li, and D. Lei, “Vacuum reliability analysis of parabolic trough receiver,” *Sol. Energy Mater. Sol. Cells*, vol. 105, pp. 302–308, 2012, doi: 10.1016/j.solmat.2012.06.034.

[53] X. Song, G. Dong, F. Gao, X. Diao, L. Zheng, and F. Zhou, “A numerical study of parabolic trough receiver with nonuniform heat flux and helical screw-tape inserts,” *Energy*, vol. 77, pp. 771–782, 2014.

[54] Z. Huang, G. L. Yu, Z. Y. Li, and W. Q. Tao, “Numerical study on heat transfer enhancement in a receiver tube of parabolic trough solar collector with dimples, protrusions and helical fins,” *Energy Procedia*, vol. 69, pp. 1306–1316, 2015.

[55] M. Muraleedharan, H. Singh, S. Suresh, and M. Udayakumar, “Directly absorbing Therminol-Al2O3 nano heat transfer fluid for linear solar concentrating collectors,” *Sol. Energy*, vol. 137, pp. 134–142, 2016.

[56] E. Bellos, C. Tzivanidis, K. A. Antonopoulos, and G. Gkinis, “Thermal enhancement of solar parabolic trough collectors by using nanofluids and converging-diverging absorber tube,” *Renew. Energy*, vol. 94, pp. 213–222, 2016, doi: 10.1016/j.renene.2016.03.062.

[57] A. Kasaeian, S. Daviran, R. D. Azarian, and A. Rashidi, “Performance evaluation and nanofluid using capability study of a solar parabolic trough collector,” *Energy Convers. Manag.*, vol. 89, pp. 368–375, 2015.

[58] E. Ebrahimnia-Bajestan, M. C. Moghadam, H. Niazmand, W. Daungthongsuk, and S. Wongwises, “Experimental and numerical investigation of nanofluids heat transfer characteristics for application in solar heat exchangers,” *Int. J. Heat Mass Transf.*, vol. 92, pp. 1041–1052, 2016.

[59] A. B. Kasaeian, T. Sokhansefat, M. J. Abbaspour, and M. Sokhansefat, “Numerical study of heat transfer enhancement by using Al2O3/synthetic oil nanofluid in a parabolic trough collector tube,” *World Acad. Sci. Eng. Technol.*, vol. 69, pp. 1154–1159, 2012.

[60] R. Forristall, “Heat transfer analysis and modeling of a parabolic trough solar receiver implemented in engineering equation solver,” National Renewable Energy Lab., Golden, CO.(US), 2003.

[61] C. E. Kennedy, “Review of mid-to high-temperature solar selective absorber materials,” National Renewable Energy Lab., Golden, CO.(US), 2002.

[62] J. Cheng *et al.*, “Improvement of thermal stability in the solar selective absorbing Mo–Al2O3 coating,” *Sol. energy Mater. Sol. cells*, vol. 109, pp. 204–208, 2013.

[63] E. Céspedes, M. Wirz, J. A. Sánchez-García, L. Alvarez-Fraga, R. Escobar-Galindo, and C. Prieto, “Novel Mo-Si3N4 based selective coating for high temperature concentrating solar power applications,” *Sol. Energy Mater. Sol. Cells*, vol. 122, pp. 217–225, 2014, doi: 10.1016/j.solmat.2013.12.005.

[64] J. Barriga, U. Ruiz-de-Gopegui, J. Goikoetxea, B. Coto, and H. Cachafeiro, “Selective coatings for new concepts of parabolic trough collectors,” *Energy Procedia*, vol. 49, pp. 30–39, 2014.

[65] A. Kasaeian, S. Daviran, and R. D. Azarian, “Optical and thermal investigation of selective coatings for solar absorber tube,” *Int. J. Renew. Energy Res.*, vol. 6, no. 1, pp. 15–20, 2016.

[66] C. J. Winter, “C.-J., Sizmann, RL, Vant-Hull, LL: Solar Power Plants.” Springer-Verlag, Berlin, 1991.

[67] R. Tamme, D. Laing, and W.-D. Steinmann, “Advanced thermal energy storage technology for parabolic trough,” *J. Sol. Energy Eng.*, vol. 126, no. 2, pp. 794–800, 2004.

[68] D. Laing, W.-D. Steinmann, R. Tamme, and C. Richter, “Solid media thermal storage for parabolic trough power plants,” *Sol. energy*, vol. 80, no. 10, pp. 1283–1289, 2006.

[69] S. Tamme, R., Laing, D., Steinmann, W.D., Zunft, “Innovative Thermal Energy Storage Technology for Parabolic Trough Concentrating Solar Power Plants.”

[70] L. Zhang *et al.*, “An experimental investigation of the heat losses of a U-type solar heat pipe receiver of a parabolic trough collector-based natural circulation steam generation system,” *Renew. energy*, vol. 57, pp. 262–268, 2013.

[71] F. Chen, M. Li, P. Zhang, and X. Luo, “Thermal performance of a novel linear cavity absorber for parabolic trough solar concentrator,” *Energy Convers. Manag.*, vol. 90, pp. 292–299, 2015.

[72] S. M. Jeter, “Analytical determination of the optical performance of practical parabolic trough collectors from design data,” *Sol. Energy*, vol. 39, no. 1, pp. 11–21, 1987.

[73] R. Grena, “Optical simulation of a parabolic solar trough collector,” *Int. J. Sustain. Energy*, vol. 29, no. 1, pp. 19–36, 2010.

[74] W. Huang, P. Hu, and Z. Chen, “Performance simulation of a parabolic trough solar collector,” *Sol. Energy*, vol. 86, no. 2, pp. 746–755, 2012.

[75] Z. D. Cheng, Y. L. He, and F. Q. Cui, “A new modelling method and unified code with MCRT for concentrating solar collectors and its applications,” *Appl. Energy*, vol. 101, pp. 686–698, 2013.

[76] Y. Shuai, X.-L. Xia, and H.-P. Tan, “Radiation performance of dish solar concentrator/cavity receiver systems,” *Sol. Energy*, vol. 82, no. 1, pp. 13–21, 2008.

[77] Y. L. He, J. Xiao, Z. D. Cheng, and Y. B. Tao, “A MCRT and FVM coupled simulation method for energy conversion process in parabolic trough solar collector,” *Renew. Energy*, vol. 36, no. 3, pp. 976–985, Mar. 2011, doi: 10.1016/j.renene.2010.07.017.

[78] M. Fan *et al.*, “An optimized Monte Carlo ray tracing optical simulation model and its applications to line-focus concentrating solar collectors,” *Appl. Energy*, vol. 225, pp. 769–781, 2018.

[79] S. M. Jeter, “Calculation of the concentrated flux density distribution in parabolic trough collectors by a semifinite formulation,” *Sol. Energy*, vol. 37, no. 5, pp. 335–345, 1986.

[80] C.-Y. Tsai and P. D. Lin, “Optimized variable-focus-parabolic-trough reflector for solar thermal concentrator system,” *Sol. Energy*, vol. 86, no. 5, pp. 1164–1172, 2012.

[81] M. Balghouthi, A. B. H. Ali, S. E. Trabelsi, and A. Guizani, “Optical and thermal evaluations of a medium temperature parabolic trough solar collector used in a cooling installation,” *Energy Convers. Manag.*, vol. 86, pp. 1134–1146, 2014.

[82] H. Liang, S. You, and H. Zhang, “Comparison of three optical models and analysis of geometric parameters for parabolic trough solar collectors,” *Energy*, vol. 96, pp. 37–47, 2016.

[83] M. Boukhalfa, M. Merzouk, and N. K. Merzouk, “Optical analysis of an evacuated parabolic trough receiver with a plate absorber,” 2018, doi: 10.1109/IRSEC.2018.8702915.

[84] J. Bonjour *et al.*, “Systèmes diphasiques de contrôle thermique Thermosiphons et caloducs,” *Tech. l’Ingénieur*, vol. 33, no. 0, pp. 1–24, 2010.

[85] A. Faghri, “Heat Pipes: Review, Opportunities and Challenges,” *Front. Heat Pipes*, vol. 5, no. 1, 2014, doi: 10.5098/fhp.5.1.

[86] A. Faghri, “Review and advances in heat pipe science and technology,” *J. Heat Transfer*, vol. 134, no. 12, pp. 1–18, 2012, doi: 10.1115/1.4007407.

[87] A. Faghri, *Heat pipe science and technology*. Global Digital Press, 1995.

[88] T. J. Stephen Obrey, Joel SteOenheim, Troy McBride, Markus Hehlen, Robert Reid, "High Temperature Heat Pipe Receiver for Parabolic Trough Collectorse," in *Program Summit*, 2016, p. LA-UR-16-22615.

[89] L. L. Vasiliev, L. P. Grakovich, and D. K. Khrustalev, "Optimization of flat-plate solar energy heat pipe collector parameters," *J. heat Recover. Syst.*, vol. 4, no. 3, pp. 157–164, 1984.

[90] K. A. R. Ismail and M. M. Abogderah, "Performance of a heat pipe solar collector," *J. Sol. Energy Eng. Trans. ASME*, vol. 120, no. 1, pp. 51–59, 1998, doi: 10.1115/1.2888047.

[91] S. Rittidech and S. Wannapakne, "Experimental study of the performance of a solar collector by closed-end oscillating heat pipe (CEOHP)," *Appl. Therm. Eng.*, vol. 27, no. 11–12, pp. 1978–1985, 2007.

[92] T. Muneer, M. Asif, Z. Cizmecioglu, and H. K. Ozturk, "Prospects for solar water heating within Turkish textile industry," *Renew. Sustain. Energy Rev.*, vol. 12, no. 3, pp. 807–823, 2008.

[93] M. Shafahi, V. Bianco, K. Vafai, and O. Manca, "Thermal performance of flat-shaped heat pipes using nanofluids," *Int. J. Heat Mass Transf.*, vol. 53, no. 7–8, pp. 1438–1445, 2010, doi: 10.1016/j.ijheatmasstransfer.2009.12.007.

[94] N. Zhu and K. Vafai, "Analytical modeling of the startup characteristics of asymmetrical flat-plate and disk-shaped heat pipes," *Int. J. Heat Mass Transf.*, vol. 41, no. 17, pp. 2619–2637, 1998, doi: 10.1016/S0017-9310(97)00325-6.

[95] G. Huminic, A. Huminic, I. Morjan, and F. Dumitrache, "Experimental study of the thermal performance of thermosyphon heat pipe using iron oxide nanoparticles," *Int. J. Heat Mass Transf.*, vol. 54, no. 1–3, pp. 656–661, 2011.

[96] M. Arab and A. Abbas, "Model-based design and analysis of heat pipe working fluid for optimal performance in a concentric evacuated tube solar water heater," *Sol. Energy*, vol. 94, pp. 162–176, 2013.

[97] Z. Yulan, Z. Hong, and Z. Dongdong, "Study on thermal efficiency of CPC heat pipe evacuated tubular collectors," *Acta Energiae Solaris Sin.*, vol. 28, no. 9, p. 1022, 2007.

[98] X. Xuesong and Z. Yuezhao, "Thermal performance of CPC heat pipe heat pipe evacuated tubular collectors," *J. Nanjing Univ. Technol.*, vol. 26, no. 6, pp. 53–56, 2004.

[99] R. Yunfeng, Y. Jianlin, and Z. Hua, "Experimental research on a compound parabolic concentrator heat pipe type solar collector," *JOURNAL-XIAN JIAOTONG Univ.*, vol. 41, no. 3, p. 291, 2007.

[100] Y. Wang, Y. Zhu, H. Chen, X. Zhang, L. Yang, and C. Liao, "Performance analysis of a novel sun-tracking CPC heat pipe evacuated tubular collector," *Appl. Therm. Eng.*, vol. 87, pp. 381–388, 2015.

[101] D. Zhan, H. Zhang, Y. Liu, S. Li, and J. Zhuang, "Investigation on medium temperature heat pipe receiver used in parabolic trough solar collector," in *Proceedings of ISES World Congress 2007 (Vol. I–Vol. V)*, 2008, pp. 1823–1827.

[102] W. Zhang, J. Wang, R. Tian, Q. Xue, and X. Ba, "Analysis of heat transfer characteristics for parabolic trough solar collector system with heat-pipe evacuated tube," *Trans. Chinese Soc. Agric. Eng.*, vol. 34, no. 3, pp. 202–209, 2018.

[103] A. El Fadar, A. Mimet, and M. Pérez-García, “Study of an adsorption refrigeration system powered by parabolic trough collector and coupled with a heat pipe,” *Renew. Energy*, vol. 34, no. 10, pp. 2271–2279, 2009.

[104] L. Zhang *et al.*, “An experimental investigation of a natural circulation heat pipe system applied to a parabolic trough solar collector steam generation system,” *Sol. Energy*, vol. 86, no. 3, pp. 911–919, 2012.

[105] H. J. Mosleh, S. J. Mamouri, M. B. Shafii, and A. H. Sima, “A new desalination system using a combination of heat pipe, evacuated tube and parabolic trough collector,” *Energy Convers. Manag.*, vol. 99, pp. 141–150, 2015.

[106] K. A. R. Ismail, M. A. Zanardia, and F. A. M. Lino, “Modeling and validation of a parabolic solar collector with a heat pipe absorber,” *Adv. Energy Res.*, vol. 4, no. 4, p. 299, 2016.

[107] V. P. Kalbande, P. V Walke, S. Untawale, and M. Mohan, “Performance evaluation of novel heat pipe-assisted thermal storage system with parabolic trough solar collector using nanofluid,” *Energy Technol.*, 2022.

[108] H. Fathabadi, “Novel low-cost parabolic trough solar collector with tpct heat pipe and solar tracker: Performance and comparing with commercial flat-plate and evacuated tube solar collectors,” *Sol. Energy*, vol. 195, pp. 210–222, 2020.

[109] W. Zhang, L. Duan, J. Wang, X. Ba, Z. Zhang, and R. Tian, “Influences of tracking and installation errors on the optical performance of a parabolic trough collector with heat pipe evacuated tube,” *Sustain. Energy Technol. Assessments*, vol. 50, p. 101721, 2022.

[110] A. Meskine, “Contribution à l’étude thermo-optique du capteur évacué à structure cylindrique.” 1982.

[111] M. Merzouk, “Contribution à la Détermination des Performances Théoriques et Expérimentales des Capteurs Solaires à Tubes Sous-vide en Régime Transitoire,” *Thèse Docteur d’état en Phys. énergétique, Univ. aboubaker belkaid Tlemcen*, 2004.

[112] M. Merzouk, P. R. Bala, M. Feidt, and B. Benyoucef, “Derivation of a tube solar collector transmittance for beam and diffuse radiation,” *Int. J. Therm. Sci.*, vol. 42, no. 3, pp. 317–322, 2003.

[113] F. Lippke, “Simulation of the part-load behavior of a 30 MWe SEGS plant,” Sandia National Labs., Albuquerque, NM (United States), 1995.

[114] R. Lazzarin, “Sistemi Solari Attivi: Manuale Di Calcolo (Solar Passive Systems: A Calculation Handbook),” *F. Muzzio C.(Padova 1981)*, 1981.

[115] P. D. Dunn and D. A. Reay, “Heat pipes,” 1982.

[116] J. E. Kopp, “Two-tank indirect thermal storage designs for solar parabolic trough power plants,” 2009.

[117] J. P. Holman, “1989, Heat Transfer, McGraw-Hill, New York.”

[118] Cengel .YA, *Heat transfer and mass transfer: a practical approach, 3 rd ed. McGraw Hill Book Company*. 2006.

[119] S. A. Kalogirou, “A detailed thermal model of a parabolic trough collector receiver,” *Energy*, vol. 48, no. 1, pp. 298–306, 2012, doi: 10.1016/j.energy.2012.06.023.

[120] O. García-Valladares and N. Velázquez, “Numerical simulation of parabolic trough solar collector: Improvement using counter flow concentric circular heat exchangers,” *Int. J. Heat Mass Transf.*, vol. 52, no. 3–4, pp. 597–609, 2009.

[121] A. Belghit, M. Belahmidi, A. Bennis, B. C. Boutaleb, and S. Benet, “Numerical study of a solar dryer in forced convection,” *Rev. Générale Therm.*, vol. 11, no. 36, pp. 837–850, 1997.

[122] G. P. Peterson, “An introduction to heat pipes. Modeling, testing, and applications,” *Wiley Ser. Therm. Manag. Microelectron. Electron. Syst. New York, Chichester Wiley,| c1994*, 1994.

[123] S. Whitaker, “Forced convection heat transfer correlations for flow in pipes, past flat plates, single cylinders, single spheres, and for flow in packed beds and tube bundles,” *AIChE J.*, vol. 18, no. 2, pp. 361–371, 1972, doi: 10.1002/aic.690180219.

[124] A. P. Colburn, “A method of correlating forced convection heat-transfer data and a comparison with fluid friction,” *Int. J. Heat Mass Transf.*, vol. 7, no. 12, pp. 1359–1384, 1964, doi: 10.1016/0017-9310(64)90125-5.

[125] H. Y. B. Mar, R. E. Peterson, and P. B. Zimmer, “Low cost coatings for flat plate solar collectors,” *Thin Solid Films*, vol. 39, pp. 95–103, 1976.

[126] H. Tabor, *Further studies on selective black coatings*. 1961.

[127] Z. M. Araujo, “Analise Numerica E Experimental De Conjunto Concentrador Com Tubo De Calor,” 1989.

[128] “SCHOTT,” *PTR®70 Receivers Datasheet; 2013.* .

[129] L. Valenzuela, R. López-Martín, and E. Zarza, “Optical and thermal performance of large-size parabolic-trough solar collectors from outdoor experiments: A test method and a case study,” *Energy*, vol. 70, pp. 456–464, 2014, doi: 10.1016/j.energy.2014.04.016.

[130] M. Ouagued, A. Khellaf, and L. Loukarfi, “Estimation of the temperature, heat gain and heat loss by solar parabolic trough collector under Algerian climate using different thermal oils,” *Energy Convers. Manag.*, vol. 75, pp. 191–201, 2013.

[131] W. M. Rohsenow and J. R. Hartnett, *Handbook of heat transfer*, vol. 36, no. 06. 1999.

[132] P. D. Dunn and D. Reay, *Heat pipes*. Elsevier, 2012.

[133] S. E. Ghasemi and A. A. Ranjbar, “Thermal performance analysis of solar parabolic trough collector using nanofluid as working fluid: a CFD modelling study,” *J. Mol. Liq.*, vol. 222, pp. 159–166, 2016.

[134] “<www.celsius-process.com>;2020.” .

[135] S. A. Hakem, M. Merzouk, N. Kasbadji-Merzouk, and K. Kaci, “Long-term influence of external parameters on the storage of a solar water heater with thermosyphon.”

[136] W. M. Rohsenow, “A method of correlating heat transfer data for surface boiling of liquids,” Cambridge, Mass.: MIT Division of Industrial Cooporation,[1951], 1951.

[137] C. Hoa, “Thermique des caloducs à rainures axiales: Etudes et réalisations pour des applications spatiales.” Poitiers, 2004.

[138] F. C. Prenger Jr and J. E. Kemme, “Performance limits of gravity-assist heat pipes with

simple wick structures," in *Advances in Heat Pipe Technology*, Elsevier, 1982, pp. 137–146.

[139] C. A. Busse, "Theory of the ultimate heat transfer limit of cylindrical heat pipes," *Int. J. Heat Mass Transf.*, vol. 16, no. 1, pp. 169–186, 1973, doi: 10.1016/0017-9310(73)90260-3.

[140] J. E. Deverall, J. E. Kemme, and L. W. Florschuetz, "Sonic limitations and startup problems of heat pipes," 1972.

[141] S. Lips, F. Lefèvre, and J. Bonjour, "Nucleate boiling in a flat grooved heat pipe," *Int. J. Therm. Sci.*, vol. 48, no. 7, pp. 1273–1278, 2009.